

REPORT DOCUMENTATION PAGE					Form Approved OMB No. 0704-0188	
<p>The public reporting burden for this collection of information is estimated to average 1 hour per response, including the time for reviewing instructions, searching existing data sources, gathering and maintaining the data needed, and completing and reviewing the collection of information. Send comments regarding this burden estimate or any other aspect of this collection of information, including suggestions for reducing the burden, to Department of Defense, Washington Headquarters Services, Directorate for Information Operations and Reports (0704-0188), 1215 Jefferson Davis Highway, Suite 1204, Arlington, VA 22202-4302. Respondents should be aware that notwithstanding any other provision of law, no person shall be subject to any penalty for failing to comply with a collection of information if it does not display a currently valid OMB control number.</p> <p>PLEASE DO NOT RETURN YOUR FORM TO THE ABOVE ADDRESS.</p>						
1. REPORT DATE (DD-MM-YYYY) 31-12-2018		2. REPORT TYPE Final Report		3. DATES COVERED (From - To) From 01-08-2015 To 30-09-2018		
4. TITLE AND SUBTITLE Computational Design of Carbon Nanocomposite Conductors				5a. CONTRACT NUMBER		
				5b. GRANT NUMBER N00014-15-1-2693		
				5c. PROGRAM ELEMENT NUMBER		
6. AUTHOR(S) Fahrenthold, Eric P.				5d. PROJECT NUMBER		
				5e. TASK NUMBER		
				5f. WORK UNIT NUMBER		
7. PERFORMING ORGANIZATION NAME(S) AND ADDRESS(ES) Department of Mechanical Engineering, University of Texas, Austin, TX 78712				8. PERFORMING ORGANIZATION REPORT NUMBER		
9. SPONSORING/MONITORING AGENCY NAME(S) AND ADDRESS(ES) Office of Naval Research				10. SPONSOR/MONITOR'S ACRONYM(S)		
				11. SPONSOR/MONITOR'S REPORT NUMBER(S)		
12. DISTRIBUTION/AVAILABILITY STATEMENT						
13. SUPPLEMENTARY NOTES						
14. ABSTRACT Computational materials design offers important opportunities for the development of improved naval platforms. New multiphysics simulation methods can strongly complement experimental research in the Power and Energy focus area. This grant developed and validated a new multiscale modeling approach to nanocomposite conductor design, including a novel nonholonomic Hamiltonian method for ab initio molecular dynamics.						
15. SUBJECT TERMS						
16. SECURITY CLASSIFICATION OF:			17. LIMITATION OF ABSTRACT	18. NUMBER OF PAGES	19a. NAME OF RESPONSIBLE PERSON	
a. REPORT	b. ABSTRACT	c. THIS PAGE			Eric P. Fahrenthold	
					19b. TELEPHONE NUMBER (Include area code) (512) 471-3064	

FINAL REPORT

for

ONR Grant Number N00014-15-1-2693

Computational Design of Carbon Nanocomposite Conductors

submitted by

Eric P. Fahrenthold
Professor, Department of Mechanical Engineering
University of Texas, 204 East Dean Keeton Street, Mail Code C2200
Austin, TX 78712-1591
Email: epfahren@mail.utexas.edu
Tel: (512) 471-3064, Fax: (512) 471-8727

December 31, 2018

ABSTRACT

Computational materials design offers important opportunities for the development of improved naval platforms. The development of new multiphysics simulation methods can strongly complement experimental research in the Power and Energy focus area. This grant investigated the development of reliable, high strength, high ampacity conductors. The research has developed and validated a new multiscale modeling approach to nanocomposite conductor design, including a novel nonholonomic Hamiltonian method for ab initio molecular dynamics. The research is aimed at assisting the experimental development of carbon nanocomposites which offer light weight, low cost, high reliability, and high current density.

The research is detailed the five chapters which follow:

Chapter 1: Ab Initio Study of Iodine Doped Carbon Nanotube Conductors

Chapter 2: Quantum Conductance of Copper-Carbon Nanotube Composites

Chapter 3: Nonholonomic Formulation of Ab Initio Molecular Dynamics

Chapter 4: Molecular Doping of Carbon Nanotube Wiring, Part I: Conductors

Chapter 5: Molecular Doping of Carbon Nanotube Wiring, Part II: Junctions

Additional papers are in preparation on work completed under the grant, and a code implementing the new ab initio molecular dynamics method developed under the project will be distributed as open source.

AB INITIO STUDY OF IODINE DOPED CARBON NANOTUBE CONDUCTORS

Yangchuan Li

Department of Mechanical Engineering
University of Texas
Austin, TX, USA

Eric Fahrenthold

Department of Mechanical Engineering
University of Texas
Austin, TX, USA

ABSTRACT

The widespread use of copper in power and data cabling for aircraft, ships, and ground vehicles imposes significant mass penalties and limits cable ampacity. Experimental research has suggested that iodine doped carbon nanotubes (CNT) can serve as energy efficient replacements for copper in mass sensitive cabling applications. The high computational costs of ab initio modeling have limited complimentary modeling research on the development of high specific conductance materials. In recent research the authors have applied two modeling assumptions, single zeta basis sets and approximate geometric models of the CNT junction structures, to allow an order of magnitude increase in the atom count used to model iodine doped CNT conductors. This permits the ab initio study of dopant concentration and dopant distribution effects, and the development of a fully quantum based nanowire model which may be compared directly with the results of macroscale experiments. The accuracy of the modeling assumptions is supported by comparisons of ballistic conductance calculations with known quantum solutions and by comparison of the nanowire performance predictions with published experimental data. The validated formulation offers important insights on dopant distribution effects and conduction mechanisms not amenable to direct experimental measurement.

1 INTRODUCTION

The widespread use of copper in power and data cabling for aircraft, ships, and ground vehicles imposes significant mass penalties and can limit system electrical performance. Carbon nanotube (CNT) [1,2] based electrical conductors have attracted considerable attention, as potential replacements for pure copper, since they may offer improved specific conductivity [3] and higher ampacity [4,5]. CNT based conductors have been studied both experimentally and computationally, as a promising new cable technology. Their relatively low electrical conductivity [6], as compared to copper, has encouraged the consideration of doped nanotubes as mass efficient replacements in weight sensitive applications. Tables 1 and 2 compare published data on the electrical conductivity and the mass specific electrical conductivity of doped CNT with the corresponding properties of copper.

Over the course of the last two decades, considerable experimental research has investigated the conduction performance of single wall carbon nanotubes (SWCNT) [7],

multi-wall carbon nanotubes (MWCNT) [8], doped CNT [3,9-12], CNT composites [13,14], CNT junctions [15], and CNT networks [16]. Complimentary computational research on these topics has also been performed, although the ab initio computational literature has modeled rather simple systems [11], due in large part to high computational cost. Given the substantial basic knowledge base, recent experimental and computational research has increasingly focused on the most promising material candidates to replace copper in weight sensitive engineering applications [17,18]. An example application is the development of high specific conductivity power and data cabling for civilian and military aircraft.

Table 1. Electrical conductivities

Material	Conductivity σ (S/cm)
Cu	5.80×10^5 [4]
Undoped CNT fiber	$(1.82 - 2.90) \times 10^4$ [17,18]
Iodine doped CNT fiber	$(5.00 - 6.67) \times 10^4$ [3,17]
Acid doped CNT fiber	$(2.42 - 3.89) \times 10^4$ [5]

Table 2. Mass specific electrical conductivities

Material	Specific conductivity σ/ρ (S · cm ² /g)
Cu	6.47×10^4 [4]
Iodine doped CNT fiber	$(0.65 - 1.96) \times 10^5$ [3]

The most widely used approach to ballistic conductance modeling employs density functional theory and non-equilibrium Green's function methods to study the electrical transport properties of nanoscale conductors [19-21]. Since a macroscopic CNT cable is necessarily composed of many nanoscale CNT conductors and junctions, modeling work on the ballistic conductance of both CNT conductors and CNT junctions is of major interest.

Previous work on CNT conductors has included studies of: (1) defects (e.g. vacancies [22]), (2) chemical doping (e.g. F [23], I₂, ICl, IBr [11], MoO₃ [24], AuCl₃ [25]), (3) multiwall CNT systems (e.g. a double wall CNT in which each tube has different electrical properties [26] or a double wall CNT with variations in the inter-wall spacing [8]), and (4) the performance of nanocomposite wires (e.g. copper-CNT conductors [27] and sulfur chains positioned inside CNT [28]). Some research has

investigated such parameters acting in combination. For example, Lopez-Bezanilla [29] investigated chemically doped double wall CNT, examining the effects of both inter-wall spacing and outer wall modification [by monovalent phenyl ($-C_6H_5$) and divalent dichlorocarbene ($>CCl_2$) dopants] on conductor performance. Note that doping can also have negative effects on conductivity. The last cited research suggested that monovalent dopants have a stronger negative (for metallic CNT) effects on conductance than do divalent dopants. They noted that large inter-wall spacing can prevent the negative effects of outer tube doping from affecting the inner tube.

In the case of CNT junctions, modeling research has focused on: (1) structural effects (e.g. variations in junction overlap [30,31] or tube intersection angles [32,33]), and (2) chemical doping effects (including transition metals [34], gold nanoparticles [35], or O_2 and N_2 [36]) on junction performance. The computational results indicate that the junction conductance ‘oscillates’ with the extent of tube overlap, which may explained by ‘quantum interference’ effects [30,31]. With respect to tube intersection angles, the highest conductance has been reported to occur when the junction structure is ‘commensurate’ [33]. In the case of transition metal doping, it appears that the best junction conductance results from chromium doping [34].

In the case of CNT network modeling, most modeling work has employed percolation theory, which accounts for both conductor and junction performance. For example, references [16,37,38] combine the macroscale conductance properties of the conductor with the ballistic conductance properties of the junctions to predict the overall performance of CNT composites. In this paper, overall CNT network performance is estimated by developing a transmission line model, parametrized by the ballistic conductance properties of both the CNT conductors and the CNT junctions. Hence in all cases, the results presented in this paper are based on electronic structure calculations.

The succeeding sections of this paper are organized as follows. Section 2 describes the computational methods employed. Section 3 presents modeling results on polyiodide doped CNT conductors and junctions. The effects of iodine doping on both metallic [CNT(M)] and semiconducting [CNT(S)] carbon nanotubes are included in the analysis. As compared to previous work [11,39] on iodine dopants, this section considers atom counts as high as 616, an approximate order of magnitude increase over the last cited works. The combination of high atom counts, complex junction structures, and complex dopant distributions resulted in very high computational costs. Hence this section also describes certain modeling approximations introduced in order to perform ballistic conductance analyses at models sizes sufficient to allow for the study of nanotube interaction, dopant concentration, and dopant distribution effects. The study of these effects is a critical part of any attempt to compare ab initio performance predictions with macroscale experimental results.

Section 4 formulates a transmission line model, used to estimate nanowire performance, applying conductor and junction analysis data presented in the preceding section. The transmission line is represented as series combination [16] of

CNT conductors and CNT junctions (alternative methods might be used [40]), in order to estimate nanowire performance. Using room temperature copper conductor properties as a reference, the expected performance of various CNT based conductors are compared, on a specific conductivity basis.

Section 5 discusses conclusions suggested by the computational results presented in the paper.

2 COMPUTATIONAL METHODS

The computational package used in this paper is the open source code SIESTA [41], which is based on density functional theory (DFT) and employs atomic orbitals as a basis set. The electrical transport properties are computed using a non-equilibrium Green’s function (NEGF) method [42], implemented in the TranSIESTA module [43] of the SIESTA package. The electrical conductance (G) is calculated using the Landauer formula [44].

$$G = 2 \frac{e^2}{h} \int -\frac{\partial f(E)}{\partial E} T(E) dE, T(E) = Tr[t^\dagger(E)t(E)] \quad (1)$$

where e is the electron charge, h is Planck’s constant, $f(E)$ is the Fermi-Dirac distribution function, E is the wave energy, $T(E)$ is the transmission function, \dagger denotes the conjugate transpose, and $t(E)$ is a matrix of transmission coefficients for waves propagating along the conductor. The calculations presented in this paper are made for zero temperature conditions, in which case [45]

$$-\frac{\partial f(E)}{\partial E} = \delta(E - E_f) \quad (2)$$

with E_f the Fermi energy and δ a Dirac delta function, so that

$$G = G_0 T(E_f), \quad G_0 = 2 \frac{e^2}{h} = 7.75 \times 10^{-5} \text{ S} \quad (3)$$

where G_0 is the standard quantum conductance unit. For an ideal metallic carbon nanotube, $T(E_f) = 2$ and $G = 2G_0$ [7].

All calculations were performed using the generalized gradient approximation (GGA) for the exchange-correlation functional parameterized by Perdew-Burke-Ernzerhof [46]. A single-zeta basis set was employed for all atoms, to reduce computational cost. The accuracy of the single-zeta basis calculations was evaluated by comparing the computed ballistic conductance results for single and dual parallel metallic nanotubes to the ‘exact’ conductance solutions for those systems. The integration k-points in the Brillouin zone were chosen using a Monkhorst-Pack mesh [47]. The model parameters used in the calculations are discussed in the sections which follow.

The junction conductance calculations presented in this paper were performed on atom sets obtained by removing atoms from ‘relaxed’ models of dual, parallel, doped and undoped nanotubes. This approximation was adopted in part due to

difficulties encountered in obtaining converged equilibrium solutions for junction structures using the default SIESTA force convergence criterion (0.04 eV/Å). Note that published work has employed force convergence criteria that vary by two orders of magnitude (0.001 eV/Å [48] to 0.1 eV/Å [36]).

The accuracy of the approximate junction models was evaluated by comparing the predictions of a nanowire performance model (which incorporates the approximate junction models) with published experimental data on iodine doped CNT fibers, as detailed in Section 4. Such indirect validation of the approximate junction models is necessitated by the absence of nanoscale experimental data measuring directly junction ballistic conduction as a function of junction geometry, nanotube type, doping concentration, and dopant distribution. The consistency of the nanowire modeling results with published macroscale experimental data suggests that the conductance calculations presented in this paper are in general representative of the modeled physical systems. The conclusions presented in Section 5, which discuss junction geometry, doping mass fraction, doping distribution, and other characteristics of the system not amenable to direct experimental measurement are intended to assist experimental research on the development of new high specific conductivity cabling.

3 POLYIODIDE DOPED CNT

In general, the performance of iodine doped CNT systems may be affected by iodine atom interactions. An example is the presence of iodine in polyiodide form, as described in experimental papers on both CNT [3,49] and graphene [50], which suggest that I_3^- and I_5^- polyiodide chains may be formed during the doping process. An iodine chain structure located inside CNT's was also observed in experiments performed by Fan et al. [51].

Transmission electron microscope images of iodine doped CNT [3] suggest that the iodine distribution in doped CNT cables consists of: (1) interstitial dopant atoms concentrated near CNT 'contacts' and (2) randomly distributed dopant atoms scattered across CNT surfaces. To better understand the effects of polyiodide doping, the analysis which follows considers CNT's doped with polyiodide (note that the present model is formulated at the electronic structure level, no molecular structure is imposed). The interaction of both metallic and semiconducting CNT's with polyiodides is investigated.

The following iodine doped system configurations were modeled, for both metallic and semiconducting CNT (in some configurations, dopant weighting was also varied):

- CNT conductors with 'aligned' doping
- CNT conductors with 'random' doping
- CNT conductors with 'interstitial' doping
- CNT junctions with 'interstitial' doping

The modeled CNT are metallic with chirality (5,5) [CNT(5,5)] and semiconducting with chirality (8,0) [CNT(8,0)], which have diameters 7.1 Å and 6.4 Å respectively. Note that the smallest energetically stable CNT has diameter of 4 Å [52]. The calculations employed k-points chosen using a Monkhorst-Pack

mesh [47]. It is important to note that previous work has employed k-grid dimensions which varied widely. Published conductance calculations have employed k-point dimensions that range from $1 \times 1 \times 4$ [29,34] to $1 \times 1 \times 50$ [53,54]. Since the models presented here are computationally quite expensive, a relatively coarse k-grid was selected. For the relaxation calculations, the k-grid has dimensions $1 \times 1 \times 4$ [34]. For the conductance calculations, the k-grid has dimensions $1 \times 1 \times 9$. The fineness of the real space mesh was controlled by setting the energy cutoff to 200 Ry [55,56,57].

3.1 Polyiodide Doped CNT Conductors

The polyiodide doped conductor models investigated single nanotube and dual nanotube configurations. In the single nanotube configurations, both 'aligned' and 'random' doping patterns were modeled. In the dual nanotube configuration, only 'interstitial' doping patterns were modeled. These three doping geometries are illustrated in the figures which follow.

Figure 1 shows the doped single metallic nanotube configurations considered. The first and second models assume 'aligned' dopant atoms, with 0.7 iodine atoms per CNT unit cell (0.7/u.c.) and 1.0 iodine atoms per CNT unit cell (1.0/u.c.) respectively. The third model depicts the random doping pattern. In the case of the randomly doped CNT, the electrodes were not doped.

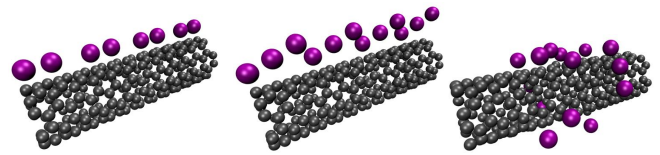


Fig. 1. CNT(5,5) models: aligned 0.7/u.c. (left), aligned 1.0/u.c. (center), and random 2.3/u.c. (right) doping

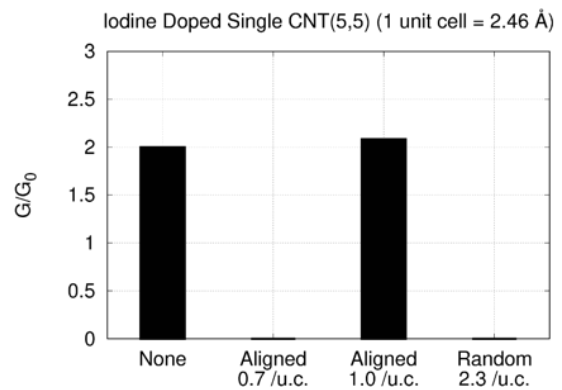


Fig. 2. Conductance of the metallic CNT models

Figure 2 shows the computed conductance for the modeled metallic CNT's. The calculation made here for an undoped metallic CNT (shown by the bar labeled 'None') correctly returns the 'exact' solution of 2.0 quantum conductance units.

Note that reference [11], which employs a double zeta basis set, returns a conductance twenty-five percent lower, perhaps due to electrode effects. The present work employs an electrode whose structure matches that of the modeled device, in order to represent a segment of a much longer (as long as the material's mean free path) conductor. The remaining three bars in Figure 2 show conductance results for the doped metallic nanotubes. They indicate that the conductance of the doped tube is affected by both the dopant concentration and the dopant distribution. At the lowest dopant concentration, the iodine converts the metallic tube into a semiconducting tube, as reported in previous experimental and computational work [39]. At the highest doping concentration, the distribution of the modeled dopant is random and the semiconducting conversion is maintained. At the intermediate doping concentration, the dopant distribution is 'aligned' and the metallic conductance of the system is restored. This restoration may be due to the formation of polyiodide structures, and two consequent effects: (1) the creation of p-doped conduction 'pathways' (axially asymmetric doping) in the nanotubes, and (2) conduction in the polyiodide chains, via a Grothuss mechanism [58,59,60]. Given the highly ordered structure of the conduction paths in metallic CNT's [61], conductance sensitivity to dopant distribution is certainly plausible.

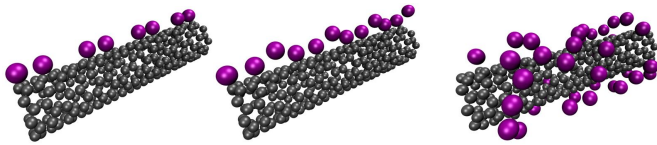


Fig. 3. CNT(8,0) models: aligned 1.0/u.c. (left), aligned 1.5/u.c. (middle), and random 4.9/u.c. (right) doping

Figure 3 shows the doped single semiconducting nanotube configurations considered. The first and second models assume 'aligned' dopant atoms, with 1.0 iodine atoms per CNT unit cell and 1.5 iodine atoms per CNT unit cell respectively. The third model depicts the random doping pattern. In the case of the semiconducting CNT's, the electrodes were doped.

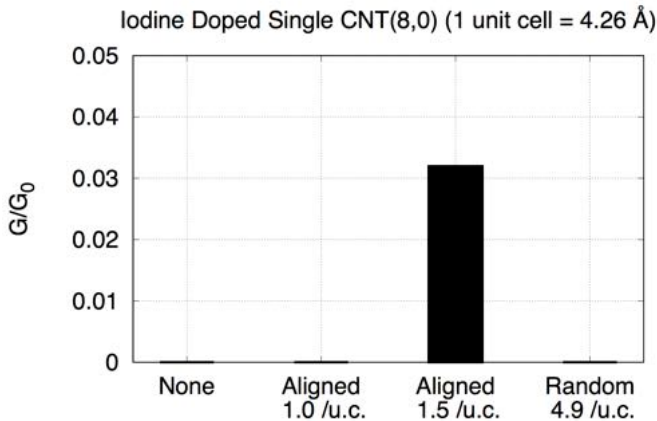


Fig. 4. Conductance of the semiconducting CNT models

Figure 4 shows the computed conductance for the modeled semiconducting CNT's. The calculation made here for an undoped semiconducting CNT (shown by the bar labeled 'None') returns (as expected) negligible conductance. Note that reference [11], which employs a double zeta basis set, returns a conductance fully seventy percent of that computed (in that work) for a metallic tube, in a copper electrode configuration. The remaining three bars in Figure 4 show conductance results for the doped semiconducting nanotubes. As in the metallic case, they indicate that the conductance of the doped tube is affected by both the dopant concentration and the dopant distribution. At the lowest dopant concentration, application of the iodine does not improve conductance. At the highest doping concentration, the distribution of the modeled dopant is random and the conductance is again negligible. At the intermediate doping concentration, the dopant distribution is 'aligned' and a small but nonzero conductance is computed. The modeling results might again be explained by the formation of polyiodide structures, and: (1) the creation of p-doped conduction 'pathways' (axially asymmetric doping) in the nanotubes, and (2) conduction in the polyiodide chains.

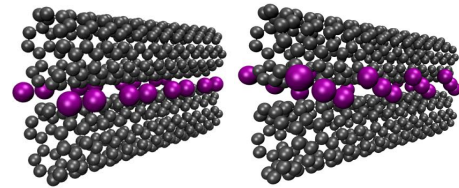


Fig. 5. Doped metallic CNT(5,5): 1.3/u.c. (left) and 2.0/u.c. (right)

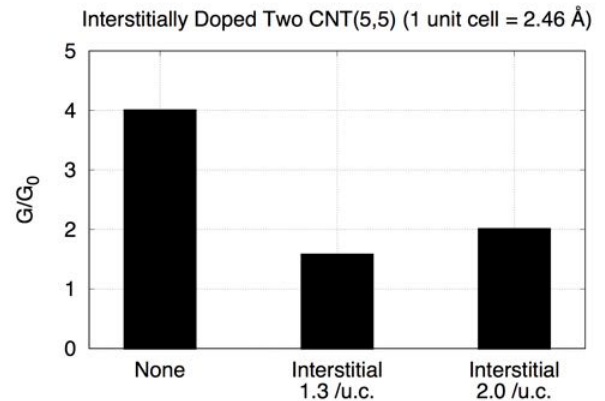


Fig. 6. Conductance of the interstitially doped dual CNT(5,5) models

Although the preceding calculations on isolated nanotubes are of great interest, experimental studies of iodine doped CNT conductors emphasize that macroscale cables are composed of nanotube bundles, and that such bundles will give rise to more complex doping patterns. The simplest doping pattern associated with interacting tubes (a pattern depicted in reference [3]) is the

‘interstitial’ doping configuration shown in Figure 5. The latter figure depicts dual parallel metallic nanotubes, interstitially doped at two different iodine concentrations. Figure 6 shows the computed conductance results for the modeled dual metallic CNT’s. The calculation for the undoped system (shown by the bar labeled ‘None’) correctly returns the ‘exact’ solution of 4.0 quantum conductance units. The remaining two bars in Figure 6 show computed conductance results for the doped dual tubes. As in the single metallic nanotube case, low levels of iodine doping significantly reduce metallic system conductance. Note that for multi-nanotube bundles, alignment of the dopant atoms along the interstitial crevice might be encouraged by some manufacturing processes (e.g. extrusion). Consistent with the arguments made for the isolated tube models, the creation of p-doped conduction ‘pathways’ (axially asymmetric doping) in the nanotubes and possible conduction within the polyiodide chains may be responsible for the non-monotonic variation in conductance.

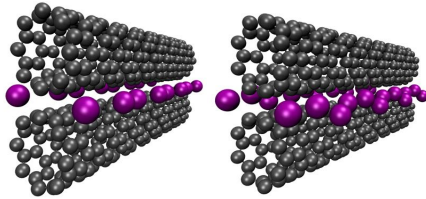


Fig. 7. Doped CNT(8,0): 2.0/u.c. (left), 3.0/u.c. (right)

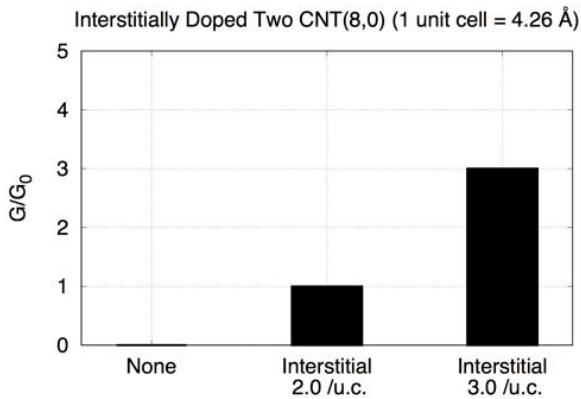


Fig. 8. Conductance of the interstitially doped dual CNT(8,0) models

Figure 7 depicts dual parallel semiconducting nanotube configurations, interstitially doped at two different iodine concentrations. Figure 8 shows the computed conductance results for the modeled dual semiconducting CNT’s. The calculation for the undoped system (shown by the bar labeled ‘None’) correctly returns a result indicating negligible conductance. The remaining two bars in Figure 8 show computed conductance results for the doped dual tubes. Interstitial iodine doping improves system conductance, and the system conductance increases with dopant concentration. As in the metallic case, the dual nanotube geometry appears to promote the formation of polyiodides and the formation of p-doped

conduction pathways. At the higher of the two modeled dopant concentrations, the computed system conductance reaches seventy-five percent of that expected for dual undoped metallic nanotubes.

3.2 Polyiodide Doped CNT Junctions

The polyiodide doped CNT junction models investigated dual nanotube configurations, at various overlaps, in interstitial doping configurations. The dopant per unit length was varied, and both metallic and semiconducting tubes were analyzed. In general, relaxation calculations for the doped CNT junctions failed to converge. The junction models were constructed by removing carbon atoms from the relaxed models of the interstitially doped CNT’s depicted in Fig. 5 and Fig. 7.

It is important to note that the junctions of interest in this paper are intended to be representative of nanotube bundles contained in macroscale cables, typically manufactured by pressure rolling [62], extrusion [63], or other mechanically intrusive processes. Given these circumstances, the junction models analyzed in this paper are perhaps far more likely to be representative of those in macroscale cables than any junction models obtained by ‘re-relaxation’ of isolated atomic configurations of the type depicted in Figure 9. The authors are not aware of any previous work which has performed ab initio relaxation or conductance calculations for interstitially doped junctions like those depicted in Figure 9.

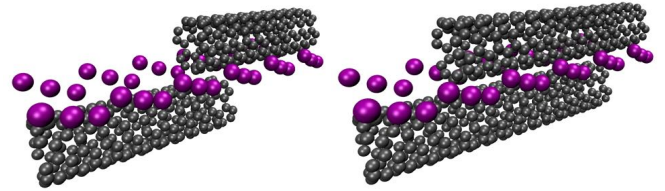


Fig. 9. Doped CNT(5,5) junction: overlaps of 2 unit cells (left) and 10 unit cells (right)

The metallic nanotube junction shown Figure 9 was analyzed at five different overlaps, ranging from 2 to 10 unit cells, without doping and at two different doping concentrations. Figure 10 shows the computed conductance results. As indicated in previous work [30,31], junction conduction does not in general vary monotonically with overlap. In the undoped configuration modeled here, the junction conductance is (at best) half that expected for an undoped metallic nanotube, emphasizing the importance of ‘contact resistance’ in determining the performance of nanotube based cabling. The reduced conductance computed (for all overlaps) at the low doping concentration mimics the previously discussed response of isolated metallic nanotubes to low dopant concentrations. Only at the highest levels of dopant concentration and overlap considered in the analysis does the junction conductance approach seventy-five percent of the conductance of a pristine nanotube: that result, indicated by the highlighted square in Fig.

10, is used in the nanowire performance calculations discussed in Section 4.

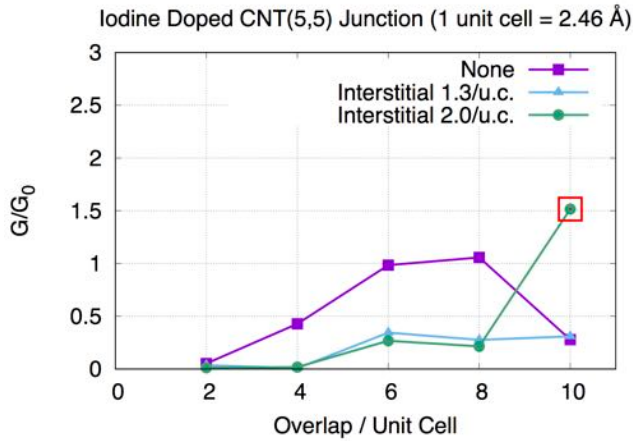


Fig. 10. Conductance of a metallic CNT(5,5) junction

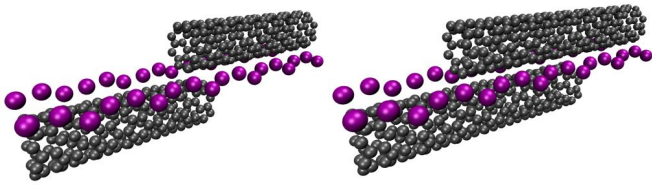


Fig. 11. Doped CNT(8,0) junction: overlaps of 0.7 unit cells (left) and 4.7 unit cells (right)

The semiconducting nanotube junction shown Figure 11 was also analyzed at five different overlaps, in this case ranging from 0.7 to 4.7 unit cells. Since the undoped semiconducting tubes analyzed previously performed as insulators, junction performance was modeled only with doping applied, at two concentrations. Figure 12 shows the computed conductance results. At the low doping concentration, the junction conductance was negligible, at all overlaps. At the high doping concentration, junction performance was very good, peaking at an overlap of 3.7 unit cells, where the doped junction performance approached that of a pristine metallic nanotube. That result, indicated by the highlighted square in Fig. 12, is used in the nanowire performance calculations discussed in Section 4.

3.2 SUMMARY

The precise effects of polyiodide doping vary significantly with nanotube type (metallic or semiconducting) and dopant distribution (aligned, random, or interstitial). The results presented in this section suggest several conclusions:

- (1) At low dopant levels, metallic nanotubes are adversely affected by iodine doping. However if the dopant is properly distributed, the performance of metallic nanotubes can be recovered (at least in part) by increasing the dopant concentration. In the case of the semiconducting nanotubes, conductance improves with iodine dopant concentration, as long as the dopant is properly distributed.

- (2) At low dopant levels, metallic nanotube junctions are adversely affected by iodine doping. However if the dopant is interstitially distributed, the performance of metallic junctions can be recovered by increasing the dopant concentration and junction overlap. In the case of the semiconducting nanotube junctions, conductance improves with iodine dopant concentration, if the dopant is interstitially distributed.
- (3) In the CNT configurations modeled here: interstitial doping is broadly beneficial, aligned doping offers some benefits, and random doping is ineffective.
- (4) Current explanations of the effects of iodine doping on CNT conductance focus broadly on iodine as p-type dopant for the CNT [11,64]. However the enhanced conductance offered by interstitial doping may more specifically be due to asymmetric p-doping of the nanotubes.
- (5) Conduction within polyiodide structures (charge transfer without mass transport [58,59,60]) may contribute to the doped system's performance. The formation of interstitial polyiodides might be encouraged by particular fabrication processes, such as pressure rolling or extrusion.

The next section of the paper applies the results of the ballistic conduction calculations just discussed, in order to estimate the measured performance of iodine doped CNT cables studied in macroscale experiments. Comparison with experiment serves to critique the assumptions made in formulating the nanoscale model, evaluating its usefulness in assisting engineering design.

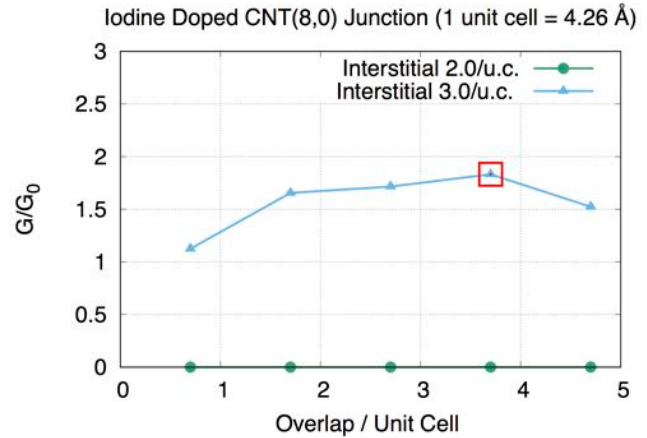


Fig. 12. Conductance of a semiconducting CNT(8,0) junction

4 TRANSMISSION LINE MODEL

In this section a nanowire is modeled as a transmission line consisting of a set of conductors, each with a length no greater than the electron mean free path for the conductor material, joined by discrete 'junction' resistors. The mass and conductivity properties of the transmission line components are taken from the ballistic conductance analysis described in the preceding section. The assumed model, shown in Fig. 13, is inspired by experimental measurements on CNT networks [16]. Estimates of

the mean free path for the nanotube based conductors are taken from the literature [65,66].

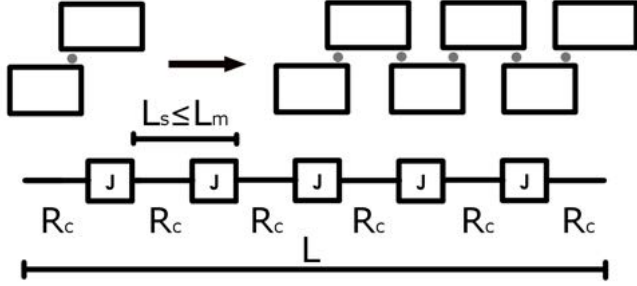


Fig. 13. Transmission line model

The mass per unit length and resistance per unit length of the transmission line are determined by the conductor resistance R_c , junction resistance R_j , conductor mass per unit length \hat{m}_c , and added mass per junction m_j^{add} , all determined from the models described in the previous section, and by the mean free path (L_m) of an electron in the conductor. Adopting the product of mass (m) per unit length and resistance (R) per unit length as performance measures for a nanowire, one may define a performance metric (M) using

$$\frac{1}{M} = \frac{\rho}{\sigma} = \frac{m}{L} \times \frac{R}{L} = \left(\hat{m}_c + \frac{m_j^{add}}{L_m} \hat{n} \right) \left(\frac{R_c + R_j}{L_m} \right) \hat{n} \quad (7)$$

where the number of junctions per mean free path is

$$\hat{n} = \frac{n}{L/L_m} \quad (8)$$

and n is the number of junctions in a transmission line of length L (composed of segments of length L_s). Note that in the case of a continuum conductor, the performance metric is the mass specific conductance, defined as the ratio of electrical conductivity (σ) to mass density (ρ).

The plots which follow employ the metric M to estimate the performance of nanowires fabricated using the material systems considered in previous sections. Specifically, they plot the relative specific conductivity M/M_{ref} versus the number of junctions per unit mean free path (\hat{n}) for each material system, where M_{ref} is a reference value for the chosen metric (the specific conductivity of pure copper). Note that for the minimum value of $\hat{n} = 1$ indicated in the plots, the number of junctions is just sufficient to permit ballistic conductance. Additional junctions add parasitic mass and resistance, reducing nanowire performance. The plots which follow assume a mean free path of either 500 nm or 1,000 nm for the CNT's [65,66]. The high performance combinations of polyiodide doped CNT conductors and junctions selected for the nanowire analysis presented in this section are shown in Table 3. The junction conductance data used in the analysis is indicated by the highlighted squares shown in Fig. 10 and Fig. 12.

The upper plot in Figure 14 shows that for the minimum junction count ($\hat{n} = 1$) and a CNT mean free path (MFP) of 500 nm, the relative specific conductance (M/M_{ref}) for the iodine doped CNT nanowires ranges from one to three: the estimated specific conductance of the CNT nanowire is as much three times that of pure copper. This range matches that described by published experimental data [3] on the performance of iodine doped CNT cables. The transmission line (nanowire) model also suggests that the number of junctions per mean free path (\hat{n}) should be limited, in order to obtain high performance. As indicated in the lower plot of Figure 14, for the range of parameters considered in this analysis, performance varies approximately linearly with mean free path.

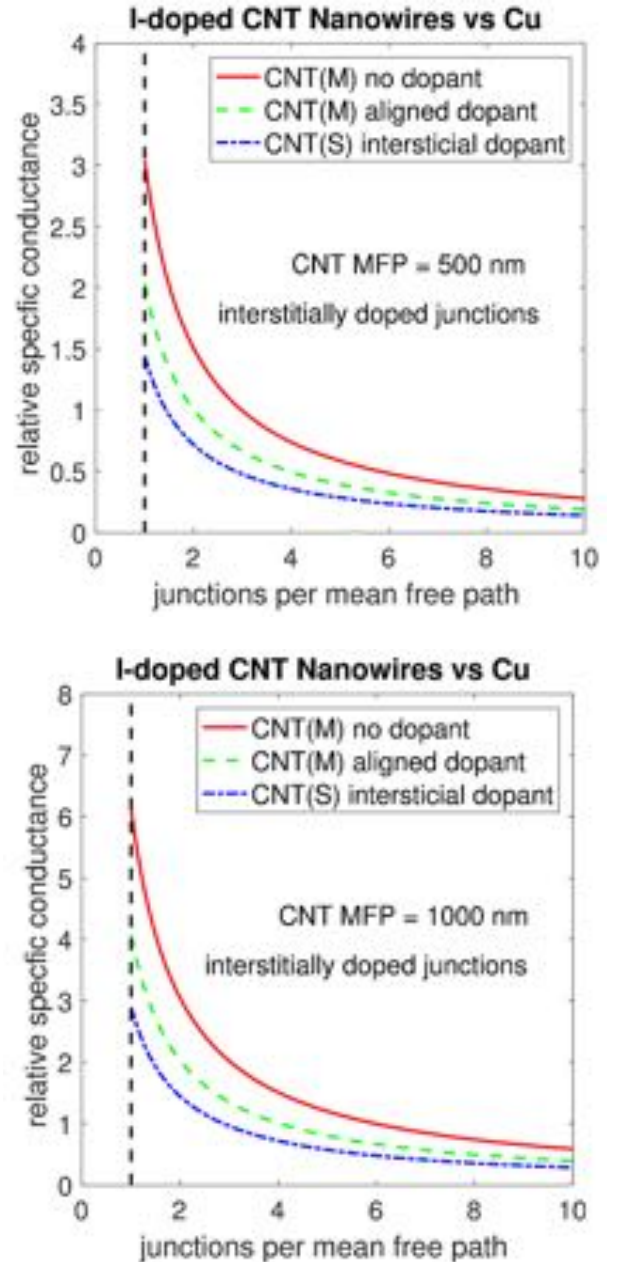
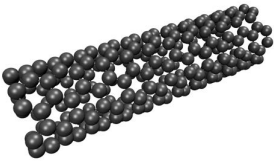
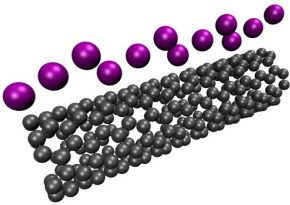
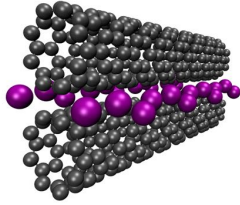
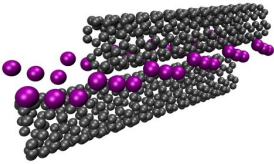
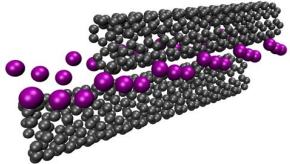
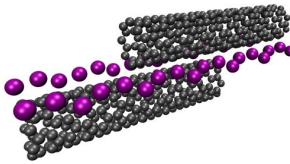


Fig. 14. Performance of the polyiodide doped CNT nanowires (MFP = 500 nm, top, and 1,000 nm, bottom)

Table 3. High performance combinations of iodine doped CNT conductors and junctions

	CNT(M)	CNT(M)	CNT(S)
Conductor	Undoped CNT	Aligned 1.0/u.c.	Interstitial 3.0/u.c.
			
	$1/R_c = 2.00G_0$	$1/R_c = 2.08G_0$	$1/R_c = 3.00G_0$
	$\hat{m}_c = 98.6 \text{ amu}/\text{\AA}$	$\hat{m}_c = 150.8 \text{ amu}/\text{\AA}$	$\hat{m}_c = 275.5 \text{ amu}/\text{\AA}$
Junction	Interstitial dopant	Interstitial dopant	Interstitial dopant
			
	$1/R_j = 1.52G_0$	$1/R_j = 1.52G_0$	$1/R_j = 1.83G_0$
	$m_j^{add} = 2538.1 \text{ amu}$	$m_j^{add} = 2538.1 \text{ amu}$	$m_j^{add} = 1395.9 \text{ amu}$

5 CONCLUSIONS

This section presents general conclusions on the polyiodide doped CNT systems analyzed in this paper, and offers suggestions for future research. The ballistic conductance and transmission line analysis results for the polyiodide doped CNT nanowires suggest a number of conclusions:

- The analysis results are consistent with published experimental data [3], which indicate that iodine doped CNT conductors can offer specific conductivity in the range of one to three times that of copper.
- The analyses presented here considered smaller diameter nanotubes (by a factor of four) and higher dopant to carbon mass ratios (by a factor of three) than those described in published experiments [3,17]. Since the model and the experiments indicate similar mass specific conductivity, mass specific performance does not appear to depend strongly on nanotube diameter.
- Estimated CNT nanowire performance varies approximately linearly with CNT mean free path; published experimental data indicates that mean free path is reduced as temperature is increased [67].
- In the case of iodine doping, realizing high specific conductivity appears to require very mass efficient use of the dopant.
- Doping distribution is highly important, and might be influenced by cable fabrication processes.
- Charge transport in within polyiodides may contribute to conductor performance.

The computational research described in this paper, and the corresponding experimental research literature, suggest many opportunities for future research. Of immediate interest are: (1) the modeling of more complex dopants, including ICl [12], KAuBr₄ [9], and others, (2) consideration of longer junction overlaps, (3) the modeling of multi-tube interactions (as computational costs permit), based on the experimentally observed complexity [68] of CNT cable architectures, (4) application of the modeling approach to graphene [50], and (5) the development of improved computational methods for both equilibrium calculations and ballistic conduction calculations, an essential enabler if computational research is to keep pace with experimental work on the increasingly complex cable nanostructures, doping systems, and fabrication processes of interest.

ACKNOWLEDGMENTS

This work was supported by the Office of Naval Research (Grant N00014-15-1-2693). Computer time support was provided by the Texas Advanced Computing Center at the University of Texas at Austin.

REFERENCES

- [1] M. F. L. De Volder, S. H. Tawfick, R. H. Baughman, and A. J. Hart, 2013, "Carbon nanotubes: present and future commercial applications.," *Science*, **339** (6119), pp. 535–539.
- [2] J. M. Wernik and S. a. Meguid, 2010, "Recent Developments in Multifunctional Nanocomposites Using Carbon Nanotubes," *Appl. Mech. Rev.*, **63** (5), p. 50801.
- [3] Y. Zhao, J. Wei, R. Vajtai, P. M. Ajayan, and E. V Barrera, 2011, "Iodine doped carbon nanotube cables exceeding specific electrical conductivity of metals.," *Sci. Rep.*, **1** (c), p. 83.
- [4] C. Subramaniam *et al.*, 2013, "One hundred fold increase in current carrying capacity in a carbon nanotube-copper composite.," *Nat. Commun.*, **4**, p. 2202.
- [5] X. Wang, N. Behabtu, C. C. Young, D. E. Tsentelovich, M. Pasquali, and J. Kono, 2014, "High-ampacity power cables of tightly-packed and aligned carbon nanotubes," *Adv. Funct. Mater.*, **24** (21), pp. 3241–3249.
- [6] S. E. Harvey, 2012, "Carbon Conductor: A Pragmatic View," *Int. Wire Cable Connect. Symp.*, p. 558.
- [7] J. Kong *et al.*, 2001, "Quantum interference and ballistic transmission in nanotube electron waveguides.," *Phys. Rev. Lett.*, **87** (10), p. 106801.
- [8] M. Soto *et al.*, 2015, "Effect of interwall interaction on the electronic structure of double-walled carbon nanotubes.," *Nanotechnology*, **26** (16), p. 165201.
- [9] J. Alvarenga *et al.*, 2010, "High conductivity carbon nanotube wires from radial densification and ionic doping," *Appl. Phys. Lett.*, **97** (18), pp. 19–22.
- [10] I. Puchades *et al.*, 2015, "Mechanism of chemical doping in electronic-type-separated single wall carbon nanotubes towards high electrical conductivity," *J. Mater. Chem. C*, **3** (39), pp. 10256–10266.
- [11] D. Janas, K. Z. Milowska, P. Bristowe, and K. Koziol, 2017, "Improving the electrical properties of carbon nanotubes with interhalogen compounds," *Nanoscale*, **44** (27), pp. 3212–3221.
- [12] D. Janas, A. P. Herman, S. Boncel, and K. K. K. Koziol, 2014, "Iodine monochloride as a powerful enhancer of electrical conductivity of carbon nanotube wires," *Carbon N. Y.*, **73** (February 2014), pp. 225–233.
- [13] L. Fan and X. Xu, 2015, "A stable iodine-doped multi-walled carbon nanotube-polypyrrole composite with improved electrical property," *Compos. Sci. Technol.*, **118**, pp. 264–268.
- [14] J. T. Wescott, P. Kung, and A. Maiti, 2007, "Conductivity of carbon nanotube polymer composites," *Appl. Phys. Lett.*, **90** (3), p. 33116.
- [15] P. L. M. S. Fuhrer, J. Nygård, L. Shih, M. Forero, Young-Gui Yoon, M. S. C. Mazzoni, Hyounghoon Choi, Jisoon Ihm, Steven G. Louie, A. Zettl, McEuen, 2000, "Crossed Nanotube Junctions," *Science*, **288** (5465), pp. 494–497.

- [16] P. N. Nirmalraj, P. E. Lyons, S. De, J. N. Coleman, and J. J. Boland, 2009, "Electrical connectivity in single-walled carbon nanotube networks," *Nano Lett.*, **9** (11), pp. 3890–3895.
- [17] N. Behabtu *et al.*, 2013, "Strong, light, multifunctional fibers of carbon nanotubes with ultrahigh conductivity," *Science*, **339** (6116), pp. 182–186.
- [18] J. N. Wang, X. G. Luo, T. Wu, and Y. Chen, 2014, "High-strength carbon nanotube fibre-like ribbon with high ductility and high electrical conductivity," *Nat. Commun.*, **5** (2005), p. 3848.
- [19] K. Stokbro, 2008, "First-principles modeling of electron transport," *J. Phys. Condens. Matter*, **20** (6), p. 64216.
- [20] Z. Qian, R. Li, S. Hou, Z. Xue, and S. Sanvito, 2007, "An efficient nonequilibrium Green's function formalism combined with density functional theory approach for calculating electron transport properties of molecular devices with quasi-one-dimensional electrodes," *J. Chem. Phys.*, **127** (19).
- [21] R. Li *et al.*, 2007, "A corrected NEGF + DFT approach for calculating electronic transport through molecular devices: Filling bound states and patching the non-equilibrium integration," *Chem. Phys.*, **336** (2–3), pp. 127–135.
- [22] B. Biel, F. J. Garcia-Vidal, A. Rubio, and F. Flores, 2008, "Ab initio study of transport properties in defected carbon nanotubes: an $O(N)$ approach," *J. Phys. Condens. Matter*, **20** (29), p. 15.
- [23] H. Park, J. Zhao, and J. P. Lu, 2006, "Effects of sidewall functionalization on conducting properties of single wall carbon nanotubes," *Nano Lett.*, **6** (5), pp. 916–919.
- [24] S. Esconjauregui *et al.*, 2015, "Efficient Transfer Doping of Carbon Nanotube Forests by MoO_3 ," *ACS Nano*, **9** (10), pp. 10422–10430.
- [25] K. K. Kim *et al.*, 2008, "Fermi level engineering of single-walled carbon nanotubes by AuCl_3 doping," *J. Am. Chem. Soc.*, **130** (38), pp. 12757–12761.
- [26] R. Moradian, S. Azadi, and H. Refii-Tabar, 2007, "When double-wall carbon nanotubes can become metallic or semiconducting," *J. Phys. Condens. Matter*, **19** (17), p. 176209.
- [27] X. J. Du, Z. Chen, J. Zhang, C. S. Yao, C. Chen, and X. L. Fan, 2012, "Structural and electronic properties of conducting Cu nanowire encapsulated in semiconducting zigzag carbon nanotubes: A first-principles study," *Phys. Status Solidi Basic Res.*, **249** (5), pp. 1033–1038.
- [28] T. Fujimori *et al.*, 2013, "Conducting linear chains of sulphur inside carbon nanotubes," *Nat. Commun.*, **4**, p. 2162.
- [29] A. Lopez-Bezanilla, 2013, "Electronic Transport Properties of Chemically Modified Double-Walled Carbon Nanotubes," *J. Phys. Chem. C*, **117**, pp. 15266–15271.
- [30] C. Buia, A. Buldum, and J. P. Lu, 2003, "Quantum Interference Effects in Electronic Transport through Nanotube Contacts," *Phys. Rev. B*, **67** (January), pp. 113409–113412.
- [31] F. Xu, A. Sadrzadeh, Z. Xu, and B. I. Yakobson, 2013, "Can carbon nanotube fibers achieve the ultimate conductivity? - Coupled-mode analysis for electron transport through the carbon nanotube contact," *J. Appl. Phys.*, **114** (6).
- [32] A. Buldum and J. P. Lu, 2001, "Contact resistance between carbon nanotubes," *Phys. Rev. B Condens. Matter*, **63** (16), p. 161403(1-4).
- [33] S. Ciraci, A. Buldum, and I. Batra, 2001, "Quantum effects in electrical and thermal transport through nanowires," *J. Phys. Condens.*, **13**, pp. 537–568.
- [34] E. Y. Li and N. Marzari, 2011, "Improving the electrical conductivity of carbon nanotube networks: A first-principles study," *ACS Nano*, **5** (12), pp. 9726–9736.
- [35] K. H. Khoo and J. R. Chelikowsky, 2009, "Electron transport across carbon nanotube junctions decorated with Au nanoparticles: Density functional calculations," *Phys. Rev. B - Condens. Matter Mater. Phys.*, **79** (20), p. 205422.
- [36] D. J. Mowbray, C. Morgan, and K. S. Thygesen, 2009, "Influence of O_2 and N_2 on the conductivity of carbon nanotube networks," *Phys. Rev. B - Condens. Matter Mater. Phys.*, **79** (19), pp. 1–6.
- [37] W. S. B. Meguid, S. A. Meguid, Z. H. Zhu, and M. J., 2011, "Modeling electrical conductivities of nanocomposites with aligned carbon nanotubes," *Nanotechnology*, **22** (48), p. 485704.
- [38] S. Gong, Z. H. Zhu, and E. I. Haddad, 2013, "Modeling electrical conductivity of nanocomposites by considering carbon nanotube deformation at nanotube junctions," *J. Appl. Phys.*, **114** (7), p. 74303.
- [39] S. Ghosh, S. Yamijala, S. Pati, and C. Rao, 2012, "The interaction of halogen molecules with SWNTs and graphene," *RSC Advances*, **2**, pp. 1181–1188.
- [40] S. Datta, 1995, *Electronic Transport in Mesoscopic Systems*, Cambridge University Press.
- [41] J. M. Soler *et al.*, 2002, "The SIESTA method for ab initio order- N materials simulation," *J. Phys. Condens. Matter*, **14** (11), p. 2745.
- [42] S. Datta, 2000, "Nanoscale device modeling: the Green's function method," *Superlattices Microstruct.*, **28** (4), pp. 253–278.
- [43] K. Stokbro, J. Taylor, M. Brandbyge, and P. Ordejón, 2003, "TranSIESTA: A Spice for Molecular Electronics," in *Annals of the New York Academy of Sciences*, **1006**, pp. 212–226.
- [44] Y. Imry and R. Landauer, 1999, "Conductance viewed as transmission," *Rev. Mod. Phys.*, **71** (2), pp. S306–S312.
- [45] Y. B. Band and Y. Avishai, 2012, *Quantum Mechanics with Applications to Nanotechnology and Information Science*, 1st ed., Elsevier.
- [46] J. P. Perdew, K. Burke, and M. Ernzerhof, 1996, "Generalized Gradient Approximation Made Simple," *Phys. Rev. Lett.*, **77** (18), pp. 3865–3868.

- [47] J. D. Pack and H. J. Monkhorst, 1976, "Special points for Brillouin-zone integrations," *Phys. Rev. B*, **13** (4), pp. 5188–5192.
- [48] D. P. Hashim *et al.*, 2012, "Covalently bonded three-dimensional carbon nanotube solids via boron induced nanojunctions," *Sci. Rep.*, **2**, p. 363.
- [49] Z. Wu *et al.*, 2014, "Semimetallic-to-metallic transition and mobility enhancement enabled by reversible iodine doping of graphene," *Nanoscale*, **6** (21), pp. 13196–202.
- [50] R.A. Hoyt, E.M. Remillard, E.D. Cubuk, C.D. Vecitis, and E. Kaxiras, 2017, "Polyiodide-Doped Graphene," *Journal of Physical Chemistry C*, Vol. 121, pp. 609–615.
- [51] X. Fan *et al.*, 2000, "Atomic Arrangement of Iodine Atoms inside Single-Walled Carbon Nanotubes," *Phys. Rev. Lett.*, **84** (20), pp. 4621–4624.
- [52] L. Ci *et al.*, 2002, "Double wall carbon nanotubes promoted by sulfur in a floating iron catalyst CVD system," *Chem. Phys. Lett.*, **359** (1–2), pp. 63–67.
- [53] S. Liu, A. Nurbawono, and C. Zhang, 2015, "Density Functional Theory for Steady-State Nonequilibrium Molecular Junctions," *Sci. Rep.*, **5**, p. 15386.
- [54] Q. Yan, J. Wu, G. Zhou, W. Duan, and B.-L. Gu, 2005, "Ab initio study of transport properties of multiwalled carbon nanotubes," *Phys. Rev. B*, **72** (15), p. 155425.
- [55] G. Foti, 2014, "Elastic and inelastic electron transport through alkane-based molecular junctions," Ph.D. Thesis, CSIC-UPV - Centro de Física de Materiales (CFM).
- [56] T. Frederiksen, 2007, "Inelastic transport theory for nanoscale systems," Ph.D. Thesis, Technical University of Denmark.
- [57] J. X. Yu, Y. Cheng, S. Sanvito, and X. R. Chen, 2012, "Bias-dependent oscillatory electron transport of monatomic sulfur chains," *Appl. Phys. Lett.*, **100** (10), p. 103110.
- [58] P. H. Svensson and L. Kloo, 2003, "Synthesis, structure, and bonding in polyiodide and metal iodide-iodine systems," *Chem. Rev.*, **103** (5), pp. 1649–84.
- [59] I. Rubinstein and E. Gileadi, 1980, "Measurements of electrical conductivity in solid bromine and iodine," *J. Electroanal. Chem.*, **108** (2), pp. 191–201.
- [60] Tatsuo Kaiho, 2014, *Iodine Chemistry and Applications*, John Wiley & Sons, Inc.
- [61] S. Fugita and A. Suzuki. *Electrical Conduction in Graphene and Nanotubes*. Wiley-VCH, Weinheim, Germany, 2013, pp. 79 and 84.
- [62] J.N. Wang¹, X.G. Luo, T. Wu, and Y. Chen, 2014, "High-strength carbon nanotube fibre-like ribbon with high ductility and high electrical conductivity," *Nature Communications*, **5**, 3848.
- [63] A.R. Bucossi, C.D. Cress, C.M. Schauerman, J.E. Rossi, I. Puchades, and B.J. Landi, 2015, "Enhanced Electrical Conductivity in Extruded Single-Wall Carbon Nanotube Wires from Modified Coagulation Parameters and Mechanical Processing," *Applied Materials and Interfaces*, **7**, pp. 27299–27305.
- [64] B. R. Sankapal, K. Setyowati, J. Chen, and H. Liu, 2007, "Electrical properties of air-stable, iodine-doped carbon-nanotube-polymer composites," *Appl. Phys. Lett.*, **91** (17), pp. 10–13.
- [65] J. Y. Park *et al.*, 2004, "Electron-phonon scattering in metallic single-walled carbon nanotubes," *Nano Lett.*, **4** (3), pp. 517–520.
- [66] D. Mann, A. Javey, J. Kong, Q. Wang, and H. Dai, 2003, "Ballistic Transport in Metallic Nanotubes with Reliable Pd Ohmic Contacts," *Nano Lett.*, **3** (11), pp. 1541–1544.
- [67] E. J. Fuller, D. Pan, B. L. Corso, O. T. Gul, and P. G. Collins, 2014, "Mean free paths in single-walled carbon nanotubes measured by Kelvin probe force microscopy," *Phys. Rev. B*, **89** (24), p. 245450.
- [68] T. Wang, X. Hu, and S. Dong, 2007, "Construction of metal nanoparticle/multiwalled carbon nanotube hybrid nanostructures providing the most accessible reaction sites," *J. Mater. Chem.*, **17** (39), pp. 4189–4195.

QUANTUM CONDUCTANCE OF COPPER-CARBON NANOTUBE COMPOSITES

Yangchuan Li

Department of Mechanical Engineering
University of Texas
Austin, TX, USA

Eric Fahrenthold

Department of Mechanical Engineering
University of Texas
Austin, TX, USA

ABSTRACT

Carbon nanotube based conductors are the focus of considerable ongoing experimental research, which has demonstrated their potential to offer increased current carrying capacity or higher specific conductance, as compared to conventional copper cabling. Complementary analytical research has been hindered by the high computational cost of large scale quantum models. The introduction of certain simplifying assumptions, supported by critical comparisons to exact solutions and the published literature, allows for quantum modeling work to assist experiment in composite conductor development. Ballistic conductance calculations may be used to identify structure-property relationships and suggest the most productive avenues for future nanocomposite conductor research.

1 INTRODUCTION

Carbon nanotubes (CNT) are the focus of considerable ongoing research aimed at the development of new engineering materials [1] and devices [2]. One application of wide practical interest is the fabrication of improved electrical conductors, offering increased current carrying capacity [3,4] or higher specific conductance [5] than conventional copper cabling. Since the conductance of CNT wiring may lag that of copper, by an order of magnitude, the most promising materials of interest appear to be composites of some kind [6], including copper-CNT (Cu-CNT) composites [4,7,8,9]. Tables 1 and 2 compare the electrical conductivity and the mass specific electrical conductivity of copper with those of CNT fibers and Cu-CNT composites [4,10,11].

Experimental research on Cu-CNT composites has demonstrated high specific electrical conductivity, good electromigration resistance, and improved current carrying capacity [4] (all compared to copper). Given this demonstrated promise, the focus of much current research is the understanding of how the composite structure influences Cu-CNT conductor properties and performance. Important nanoscale properties of Cu-CNT composites include: (1) the ballistic conductance of multiwall composite tubes, (2) the contact resistance at tube junctions, and (3) the effects of doping. These properties can be difficult to isolate and thereby measure directly. Hence computational research may assist experiment in understanding the effects of the nanoscale material structure on measured macroscale performance. This paper models ballistic conductance in double-walled tube conductors and junctions, composed of both CNT and copper. Several different configurations are considered, and chromium doping effects on the junctions are also investigated.

The objectives of the research described in this paper are to: (1) compare the conductance properties of the various Cu-CNT composites which might be formed during cable fabrication processes to the corresponding properties of copper and CNT conductors with similar nanoscale structure, and (2) compare the junction conductance (contact resistance) properties of the various Cu-CNT composites which might be formed during cable fabrication processes to the corresponding properties of copper and CNT junctions with similar nanoscale structure.

Table 1. Electrical conductivities

Material	Conductivity σ (S/cm)
Cu	5.80×10^5 [4]
CNT fiber	$(1.82 - 2.90) \times 10^4$ [10,11]
Cu-CNT composite	$(2.3 - 4.7) \times 10^5$ [4]

Table 2. Mass specific electrical conductivities

Material	Specific conductivity σ/ρ ($S \cdot cm^2/g$)
Cu	6.47×10^4 [4]
CNT fiber	4.00×10^4 [10]
Cu-CNT composite	8.15×10^4 [4]

In order to address these objectives, a rather large number of quantum scale calculations were required. These analyses involved atom counts as much as double that typical [9,12] of large scale ab initio modeling. To complete the overall numerical study at an acceptable computational cost, certain modeling approximations (discussed in the section on numerical methods) were introduced. The validity of the assumptions was critically evaluated by comparing some of the ballistic conductance calculations to known ‘exact’ solutions, and by comparing the overall composite conductor model to published experimental data. As discussed in the following sections, critical evaluation of the modeling approximations adopted here suggests that the modeling results presented in this paper are broadly representative of the physical systems of interest.

The quantum scale computational work described here is aimed at connecting nanoscale material structure to measured macroscale performance. An important goal of future computational research is to assist in the development of mechanical, thermal, and chemical processes which can be used to fabricate nanoscale structures identified (by experiment or computation) to be of particular interest.

The succeeding sections of this paper are organized as follows: section 2 discusses previous numerical modeling work in this field; section 3 describes the computational methods employed and the modeled conductor and junction geometries; section 4 provides the results of the conductance calculations; section 5 applies the conductance calculations to estimate nanowire performance; and section 6 presents overall conclusions.

2 PREVIOUS WORK

Computational work to date on Cu-CNT composite wiring has been limited; it includes studies of the interaction of copper chains with a single CNT [8,13], encapsulation of a copper tube in a single CNT [14], and embedding of a single CNT in a copper matrix [9]. Note that the last three cited papers assume quite different material structures, emphasizing that the development of any mechanical, thermal, or electrical model of a composite starts with an assumption as to what constitutes a representative volume element. Based on published (and experimentally informed) speculation [5] regarding the structure of CNT conductors, the present paper adopts the following assumption: the Cu-CNT composite structures of interest are composed of aligned (parallel), double wall tubing consisting of metallic CNT [CNT(M)], semiconducting CNT [CNT(S)], and copper [Cu] tubes, in any combination. The parallel double wall tubes interact at ‘junctions’ where adjacent outer tubes overlap and are therefore in mechanical and electrical contact. The composite structure assumed here reflects the fact that CNT conductors are typically fabricated from a mixture of single and multiwall, metallic and semiconducting nanotubes, which are approximately aligned by extrusion, pressure rolling, or other manufacturing processes. The length-to-diameter ratio limitations of current CNT fabrication methods suggest that macroscale cables may incorporate numerous junctions.

With the aforementioned representative volume element in mind, previous work on computational modeling of double wall carbon nanotubes (DWCNT) and CNT junctions is also of interest. Several previous ab initio studies have investigated the properties of DWCNT systems [15,16,17], although not all computed conductance. Conductance results for metallic DWCNT are provided in reference [12], but DWCNT composed of both CNT(M) and CNT(S) are not considered. With regard to junction performance, the properties of doped [18] and undoped [19,20,21,22] junctions have been studied for SWCNT; however, it appears that no previous work has investigated the conductance of junctions composed of overlapping DWCNT.

3 METHODOLOGY

In this paper, the electronic structure and ballistic conductance calculations were performed using the open source code SIESTA [23]. Based on density functional theory (DFT), it employs atomic orbitals as a basis set. The system was modeled as periodic, and a single-zeta basis set was employed for all atoms. Calculations were performed using the generalized gradient approximation (GGA) for the exchange-correlation functional parameterized by Perdew-Burke-Ernzerhof [24]. Although the GGA-PBE functional does not include a dispersion correction [49,41], previous work using the B3LYP functional [42] has shown that very accurate band gap calculations can be made without dispersion corrections. Dispersion corrected DFT modeling is certainly an area of interest for future research in this field. Here the integration k-points in the Brillouin zone were chosen using a Monkhorst-Pack mesh [25]. Transport

properties were computed using a non-equilibrium Green's function (NEGF) method [26], employing a k-grid with dimensions $1 \times 1 \times 100$. The fineness of the real space mesh was controlled by setting the energy cutoff to 200 Ry, and the density matrix convergence criterion was set to the default value (10^{-4}). Ballistic conductance (G) values for the multiwall tubes and junctions studied were computed using the Landauer formula [27]

$$G = 2 \frac{e^2}{h} \int -\frac{\partial f(E)}{\partial E} T(E) dE, T(E) = \text{Tr}[t^\dagger(E)t(E)] \quad (1)$$

where e is the charge on an electron, h is Planck's constant, $f(E)$ represents the Fermi-Dirac distribution function, E denotes the wave energy, and $T(E)$ is the transmission function. Note that the transmission function is computed from a matrix of transmission coefficients for electron waves, $t(E)$, where \dagger denotes the conjugate transpose. Since the calculations are made for zero temperature conditions [28],

$$-\frac{\partial f(E)}{\partial E} = \delta(E - E_f) \quad (2)$$

where E_f is the Fermi energy and δ is the Dirac delta function. Hence

$$G = G_0 T(E_f), \quad G_0 = 2 \frac{e^2}{h} = 7.75 \times 10^{-5} \text{ S} \quad (3)$$

where G_0 is one quantum conductance unit. In the case of a pristine metallic carbon nanotube, $T(E_f) = 2$ and the conductance is $G = 2G_0$ [29].

Due to the high computational cost of the present calculations, relaxation analyses of the modeled systems were not performed. Instead results suggested by the published literature were used to set atomic positions for the conduction calculations. For example, the inter-tube separation distances and dopant atom positions were taken from references [18] and [30]. Comparisons of these approximate models with exact solutions for copper conductors, exact solutions for metallic nanotubes, and published experimental data suggest that the conductance calculations presented in this paper are representative of the modeled physical systems.

The conduction calculations were applied to geometry models which represented CNT and copper-CNT systems, including both conductors and junctions. The only dopant considered is chromium. Previous computational work [18] has indicated that chromium is effective at improving CNT junction conductance.

The analysis considered thirty distinct copper, CNT, and copper-CNT models, including both metallic and semiconducting nanotubes. The ten configurations are (each configuration included three models; a conductor model, an undoped junction model, and a doped junction model):

- Double wall copper tubes, two configurations (they differ in diameter)
- Double wall copper-CNT(M) and copper-CNT(S) tubes, four configurations
- Double wall CNT(M)-CNT(S) tubes, four configurations

The metallic CNT's are chirality (5,5) (for the inner tubes) and (10,10) (for the outer tubes). The semiconducting CNT's are chirality (9,0) (for the inner tubes) and (18,0) (for the outer tubes). The tube separation distances are typical of those studied in previous computational work [51]. Note that CNT's of chirality (n,m) are often referred to as metallic if the difference of the vector indices is an integer multiple of three: $n - m = 3t$ ($t = 0, 1, 2 \dots$) [31]. However, it appears from a preponderance of the published experimental [47,45], computational [32,46,50], and review [48,54] literature that (9,0) and (18,0) in fact incorporate small band gaps. Hence this work refers to CNT(9,0) and CNT(18,0) as semiconducting. Note that the sensitivity of nanotube band gaps [43] to the electric fields used in typical band gap measurement techniques may be responsible for variations in the classification of (18,0) as metallic [45] or semiconducting [55]. More detailed consideration of this issue is however beyond the scope of the present work. The choice of (9,0) and (18,0) nanotubes for the modeling work presented in this paper was motivated by an interest in investigating the performance of 'borderline' cases with small or negligible band gaps, expecting that the inclusion of large band gap nanotubes in the present study would generate results of little interest for nanocomposite conductor applications. Nonetheless, repeating the present study for nanotubes of different chirality is certainly an object of interest for future computational research. The GGA-PBE functional used for the calculations presented in this paper represents (9,0) as semiconducting [44] and (18,0) as metallic [45]. As in the case of dispersion corrected DFT, additional modeling work which considers alternative functionals is certainly an appropriate topic for future research.

Two previous papers describe methods used to build geometry models of double wall tubes composed of CNT and copper: (1) embedding CNT into bulk Cu, thus forming a copper-CNT matrix, as shown by Ghorbani-Asl et al. [9], and (2) positioning the copper tube within a CNT, as shown by Du et al [7]. The first method avoids the problem of matching copper unit cells with CNT unit cells,

however it requires many copper atoms. This is undesirable in electronic structure calculations, where 1,000 atoms is often the model size limit. The second method reduces the atom count, however the lattice structure of the copper must be highly distorted in order to match the unit cell lengths of the copper and CNT tubes. In the present work, a special lattice composed of copper atoms is constructed, in order to overcome the disadvantages of the aforementioned methods. The structure of the special lattice is obtained by ‘rolling up’ a lattice with the structure of a graphene sheet, in which: alternating atoms in a hexagonal unit cell are either replaced by a copper atom or removed. The resulting lattice of copper atoms has an atom-to-atom separation distance of 2.46 Å, approximating the 2.56 Å separation distance of atoms on the (111) face of a copper crystal.

In all of the models, the electrodes were composed of nanotube segments identical those used to represent the conductors. The computed conductance values therefore represent the properties of a representative segment of an infinitely long transmission line. In order for the periodicity of the electrode models to match the periodicity of the physical nanotubes, both electrodes of the double wall model must contain an integer number of unit cells. In the copper-CNT(M) conductors, the unit cell length in the axial direction is 2.46 Å, while the total conductor model length is 29.5 Å (12 unit cells). The model includes one electrode on each end, each with of length 7.38 Å (3 unit cells). The conductor and junction model configurations are shown in Figures 1 and 2. In the copper-CNT(S) conductors, the unit cell length in the axial direction is 4.26 Å, while the total conductor model length is 34.1 Å (8 unit cells). The model includes two electrodes, each of length 8.53 Å (2 unit cells). The conductor and junction model configurations are shown in Figures 3 and 4. Table 3 lists the atom counts and tube diameters for all of the dual tube models considered in this work. Note from Table 3 that all the models are constructed from only two inner diameters (corresponding to those of (5,5) and (9,0) CNT) and two outer diameters (corresponding to those of (10,10) and (18,0) CNT); the special lattices for the copper tubes were in all cases generated to match those four diameters. In the case of the junction models, the tube diameters remain the same but the atom count is increased by one (single Chromium dopant atom).

Since the junctions model the interaction of identical dual tube conductors, the junctions (shown in Figures 2 and 4) are always symmetric, and take one of four forms: undoped Cu-Cu, doped Cu-Cu, undoped CNT-CNT, or doped CNT-CNT. In the undoped copper-copper junctions, the intertube separation distance (all separation distances are measured between atom centers of mass) is set to 2.1 Å, so that the atomic separation distance for nearest neighbor atoms of the two tubes matches the separation distance for near neighbor atoms of the same tube (2.46 Å). In the undoped CNT-CNT junctions, the intertube separation distance is set to 3.3 Å, which is the interlayer spacing in graphite [33]. In the doped CNT-CNT junctions, the intertube separation distance is set to 3.6 Å, which yields an average separation distance between the chromium atom and its near neighbor carbon atoms of 2.34 Å (consistent with the relaxed geometry calculations performed by Li et al. [18] for a single wall CNT). In the doped copper-copper junctions, the intertube separation distance is set to 2.4 Å, so that the incremental increase in the intertube separation distance associated with the introduction of a dopant atom is the same in the copper-copper case and the CNT-CNT case. Figure 5 shows detailed views of the doped junctions. Variations in the model geometries, dopant type, dopant distribution, voltage bias, and other parameters were not considered in the present work, which already incorporates a very extensive set of calculations. However, such parameter studies are certainly of interest for future research.

The descriptions of the dual wall models which follow employ the shorthand notation A@B, where ‘A’ denotes the inside tube type and ‘B’ denotes the outside tube type. Modeling the CNT(M)@CNT(M) and CNT(S)@CNT(S) systems is simplified by the fact that the axial direction unit cell lengths for the inner and outer tubes are the same. The nanotubes are commensurate, as defined in Fig. 1 of reference [34]. Modeling the mixed metallic and semiconducting double wall CNT systems is more complicated, since they are constructed using incommensurate CNT’s. As stated by Liu et. al [35]:

“Electronic structure calculations of incommensurate DWCNT’s ... are challenging because a finite unit cell does not exist.”

Here we model the incommensurate CNT(5,5)@CNT(18,0) and CNT(9,0)@CNT(10,10) systems by: (1) aligning five metallic unit cells with three semiconducting unit cells, then (2) uniaxially compressing (without radial deformation) the semiconducting CNT by 3.76 percent (note that previous DFT work [51] has investigated much larger uniaxial strains in low dimensional materials, without numerical difficulties). The resulting supercell contains five metallic and three semiconducting CNT’s and has a length of 12.30 Å. Table 4 shows the lengths of the unit cells (in the transport direction) and the lengths of the supercells employed to model the incommensurate DWCNT systems. Figure 6 shows one supercell each for the CNT(5,5)@CNT(18,0) and CNT(9,0)@CNT(10,10) systems. The total model (including the electrode) has a length of 49.2 Å (four supercells), with the two electrodes each composed of one supercell.

4 CONDUCTANCE CALCULATIONS

The geometric models described in the last section are used to compute scaled conductance (S) and scaled specific conductance for the double wall tubes (S_t) and the junctions (S_j). These variables are defined by:

$$S = \frac{G}{G_0} \quad (4)$$

$$S_t = \frac{G}{G_0} \frac{1}{\hat{m}_c} \quad (5)$$

$$S_j = \frac{G}{G_0} \frac{L_j}{m_j}, \quad m_j = 2\hat{m}_c L_j + m_d \quad (6)$$

where \hat{m}_c is the mass per unit length of the conductor, L_j is the junction length (tube overlap), m_j is the mass associated with the junction, and m_d is the mass of the dopant. It is the double wall tube specific conductance and the junction conductance which are of most interest in estimating nanowire performance. Hence the summary bar charts included in this section compare the results for the various material systems by plotting only the latter two variables.

Figures 7-10 show all of the double wall configurations that were analyzed, while Figures 11-14 show the corresponding conductance modeling results.

Figures 11 and 12 indicate that the conductance and the specific conductance results for the Cu-CNT(M) and Cu-CNT(S) composite systems are quite similar, and that the mass specific performance of these systems is very close to that of copper. In all these cases, the introduction of a junction incurs a large conductance penalty. When the outer tubes in contact are copper, doping further reduces junction performance. When the outer tubes in contact are CNT, junction performance recovers slightly in response to the dopant. The latter result is consistent with published computational results [18] indicating that chromium doping of CNT-CNT junctions will increase the CNT ‘coupling’.

Table 3. Tube diameters and atom counts for the models

Model type (inside@outside)	Diameters (Å)	Atom Count (DWNT/junction)
Cu@Cu	6.78@13.6	360/375
CNT(M)@Cu	6.78@13.6	480/500
Cu@CNT(M)	6.78@13.6	600/625
Cu@Cu	7.05@14.1	432/432
CNT(S)@Cu	7.05@14.1	576/576
Cu@CNT(S)	7.05@14.1	720/720
CNT(M)@CNT(M)	6.78@13.6	720/750
CNT(S)@CNT(S)	7.05@14.1	864/864
CNT(S)@CNT(M)	7.05@13.6	1232/1260
CNT(M)@CNT(S)	6.78@14.1	1264/1264

Notes: ‘DWNT’ denotes the double wall nanotube model; increase the atom count by one for the doped junction models

Table 4. Incommensurate DWCNT model dimensions

CNT chirality	Unit cell length (Å)	Supercell length (Å)
(5,5)	2.46	2.46×5=12.30
(10,10)	2.46	2.46×5=12.30
(9,0)	4.26	4.26×3=12.78 comp. to 12.30
(18,0)	4.26	4.26×3=12.78 comp. to 12.30

Note: the abbreviation “comp.” denotes compressed

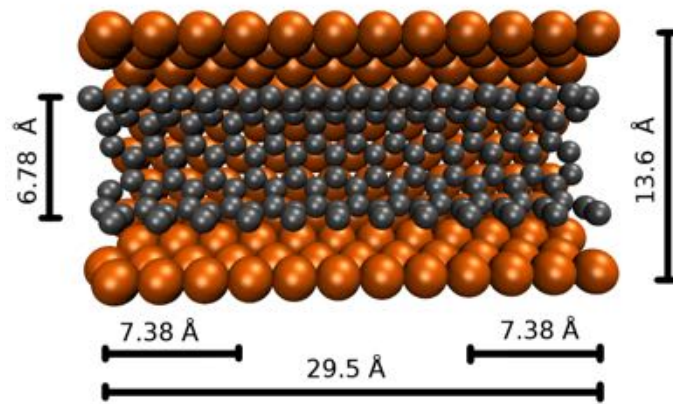


Fig. 1. Dimensions of the CNT(M)@Cu conductor

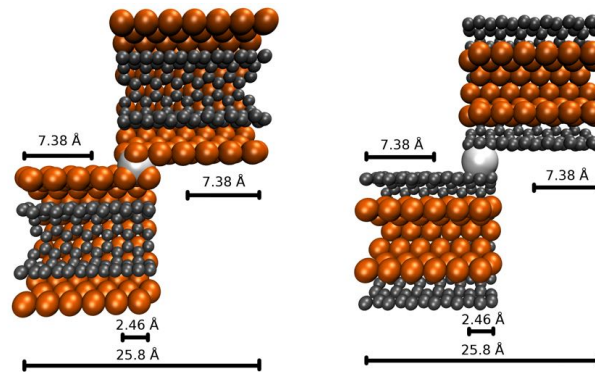


Fig. 2. Dimensions of the CNT(M)@Cu (left) and Cu@CNT(M) (right) doped junctions

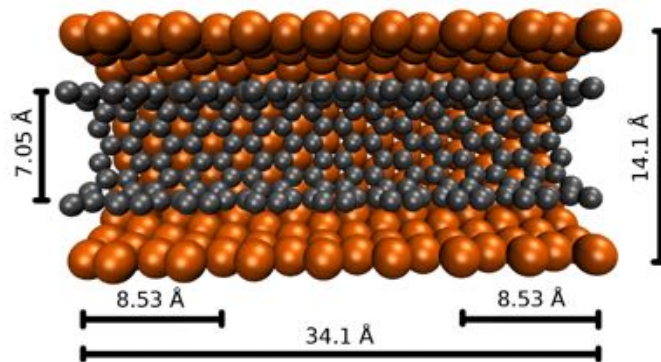


Fig. 3. Dimensions of the CNT(S)@Cu conductor

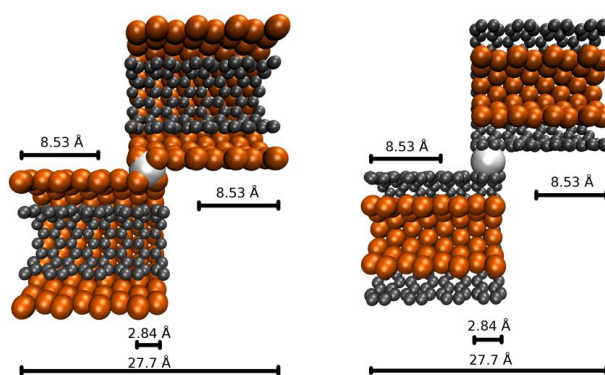


Fig. 4. Dimensions of the CNT(S)@Cu (left) and Cu@CNT(S) (right) doped junctions

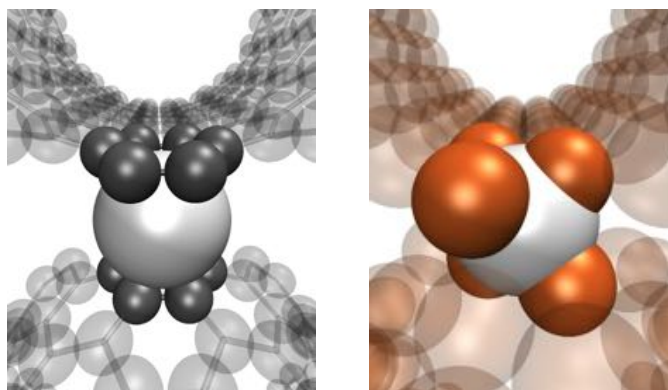


Fig. 5. Chromium doped CNT-CNT junction (left) and copper-copper junction (right)

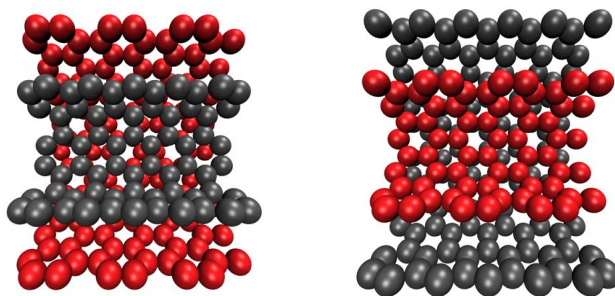


Fig. 6. One supercell for CNT(5,5)@CNT(18,0) (left) and for CNT(9,0)@CNT(10,10) (right)

Figure 13 indicates, consistent with published results [19], that the conductance of the metallic DWCNT conductor is $4G_0$. The conductance of the semiconducting DWCNT system is negligible. For the metallic DWCNT system, the introduction of a junction incurs a large conductance penalty; the junction performance shows a modest (25%) improvement in response to the doping. On a mass specific basis, performance of the metallic DWCNT system is inferior to that of the composite Cu-CNT systems.

Figure 14 indicates, as expected, that the incommensurate DWCNT conductors exhibit the conductance of a single metallic tube (the conductance is $2G_0$); hence semiconducting member of the tube pair is essentially a parasitic mass which reduces mass specific performance. Again the introduction of a junction incurs a large conductance penalty; however, if the outer tube is metallic, the junction performance shows a substantial (50%) recovery in response to the doping.

Figure 15 compares the mass specific conductance of all of the double wall conductor models, while Figure 16 compares the conductance of all of the doped junction models. Figure 17 plots the conductance for four of the undoped Cu-Cu and Cu-CNT junctions. For all of the other undoped junctions, the conductance is zero (all results are shown in Figures 11-14). Since Cu@Cu models were constructed for two different tube diameters, two Cu@Cu results are shown in Figures 15, 16, and 17 (they are differentiated by labels in which “D” denotes the outer diameter). Note that for all of the junction models investigated in the paper, only the outer tubes are in contact.

5 NANOWIRE MODEL

The conductance calculations presented in the last section are two ingredients of a nanowire model which must be constructed in order to compare the modeling results presented in this paper to performance data obtained in macroscale experiments (note that nanoscale test data is not available for validation). The third essential ingredient is published data on the electron mean free path in the materials of interest, since the ballistic conduction calculations quantify conduction performance only over such distances. There is no generally accepted approach to relating ballistic conductance properties to macroscale wiring performance. Here we consider the simplest possible nanowire model, which consists of a series combination of resistors, each representing a nanowire segment of length L , with mass m and resistance R . In terms of the conductance (reciprocal resistance) properties calculated the last section, and the mass and mean free path properties of the conductor materials, these are

$$L = L_m \quad (7)$$

$$R = \text{MAX}(R_c, R_j) \quad (8)$$

$$m = \hat{m}_c L_m + m_j^{add} \quad (9)$$

with the added mass per junction defined by

$$m_j^{add} = \hat{m}_c L_j + m_d \quad (10)$$

The mass per unit length of the conductor \hat{m}_c , the conductor resistance R_c , the junction resistance R_j , and the junction length L_j are listed in Table 5 while the chromium dopant mass (m_d) and the mean free path (L_m) data [36,37,38,53] are taken from the literature. Note that the added mass per junction includes not only the mass of the dopant but also the mass added to the nanowire due to the double wall tube overlap. The MAX function in equation (9) avoids double counting of the transmission line resistance in the nanowire model.

If we adopt the product of mass per unit length and resistance per unit length as a performance metric (M) for a nanowire, the various nanowires may be quantitatively compared using

$$\frac{1}{M} = \frac{m}{L} \times \frac{R}{L} = \left(\hat{m}_c + \frac{m_j^{add}}{L_m} \right) \left(\frac{R}{L_m} \right) \quad (11)$$

The chosen metric is, in the case of a continuum wire, simply the mass specific conductivity of the continuum

$$\frac{1}{M} = \frac{\rho}{\sigma} \quad (12)$$

where ρ is the mass density and σ is the electrical conductivity. If we define a reference specific conductivity M_{ref} as the mass specific conductivity of copper, we can use the ratio M/M_{ref} to compare the relative performance of the various material systems studied in this paper as well as their absolute performance in comparison to copper. The comparative calculations assume a mean free path of 50

nm for the copper [36] and the copper-CNT composites and 500 nm for the CNT nanowires [37,38,53]. Given the very wide range of mean free path values reported for CNT, this parameter is subject to considerable uncertainty.

Note that the specific conductivity metric (M) has the functional form

$$M = M(R_c, R_j, \hat{m}_c, m_j^{add}, L_m) \quad (13)$$

It may be critically evaluated by assuming an ideal nanowire configuration ($R_j = 0, m_j^{add} = 0$) and the two copper-copper tube models (diameters $D_1 = 13.6\text{\AA}$ and $D_2 = 14.1\text{\AA}$) analyzed in section 4. The nanowire model line indicates

$$M = M(R_c, 0, \hat{m}_c, 0, 50nm) = 0.98 M_{ref}, D = D_1 \quad (14)$$

$$M = M(R_c, 0, \hat{m}_c, 0, 50nm) = 0.94 M_{ref}, D = D_2 \quad (15)$$

which shows excellent agreement with the room temperature properties of copper. Note that this validation is nontrivial, since it requires that the ballistic conductance properties computed for the copper tube models in section 4 be consistent with published data on the room temperature mean free path of copper.

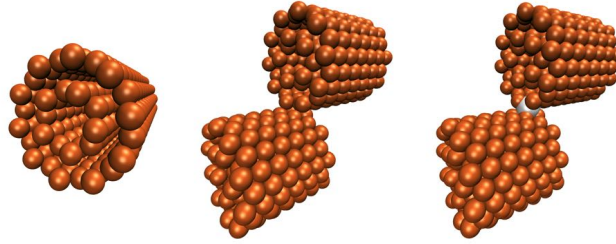


Fig. 7. Conductor, undoped junction, and doped junction for the Cu@Cu models

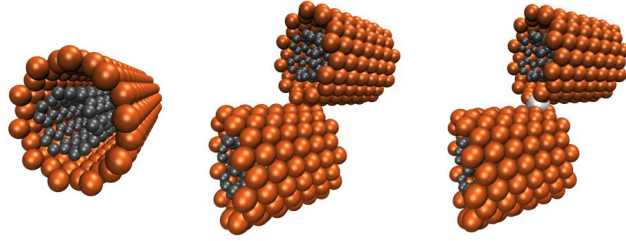


Fig. 8. Conductor, undoped junction, and doped junction for the CNT(M)@Cu models

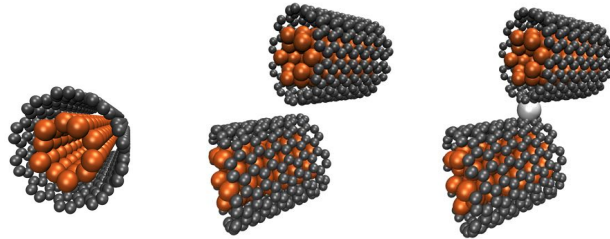


Fig. 9. Conductor, undoped junction, and doped junction for the Cu@CNT(M) models

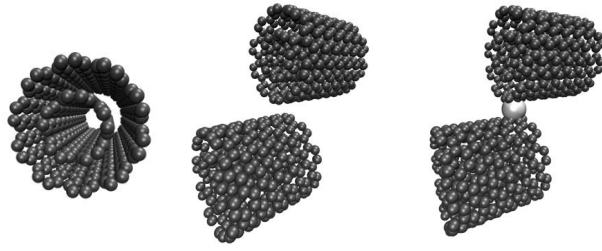


Fig. 10. Conductor, undoped junction, and doped junction for CNT(M)@CNT(M) models

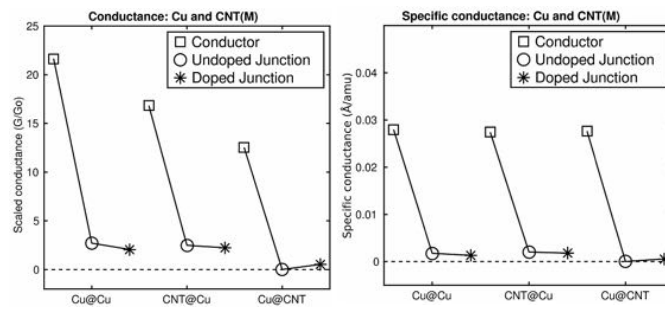


Fig. 11. Conductance and specific conductance: copper and metallic CNT models

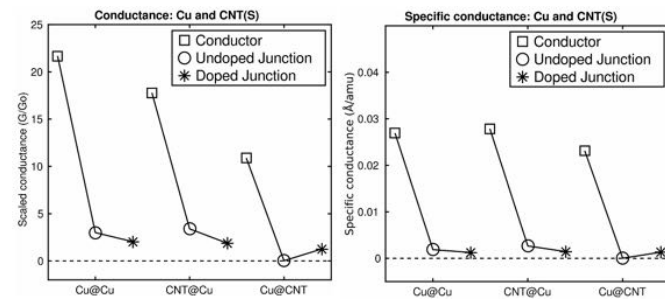


Fig. 12. Conductance and specific conductance: copper and semiconducting CNT models

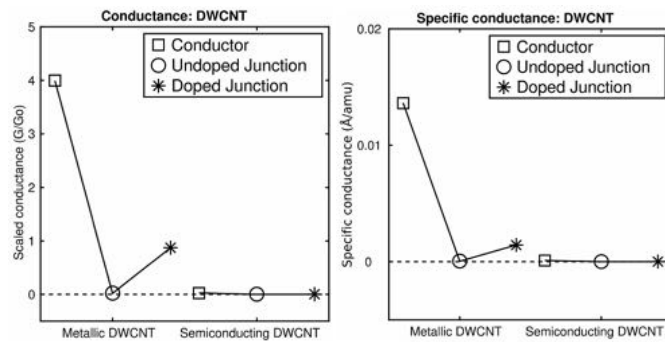


Fig. 13. Conductance and specific conductance: commensurate CNT models

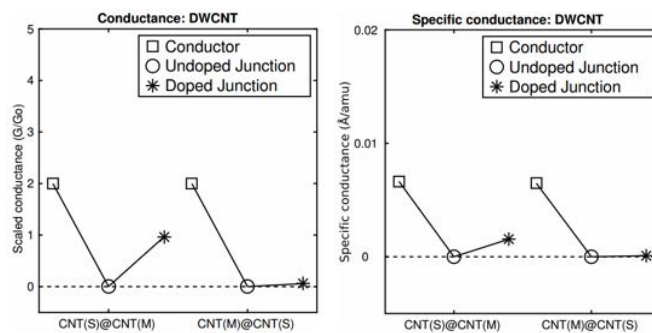


Fig. 14. Conductance and specific conductance: incommensurate CNT model

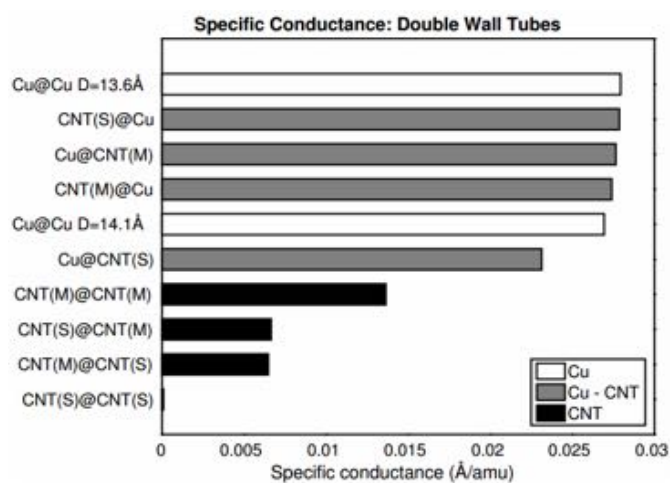


Fig. 15. Specific conductance of the double wall models

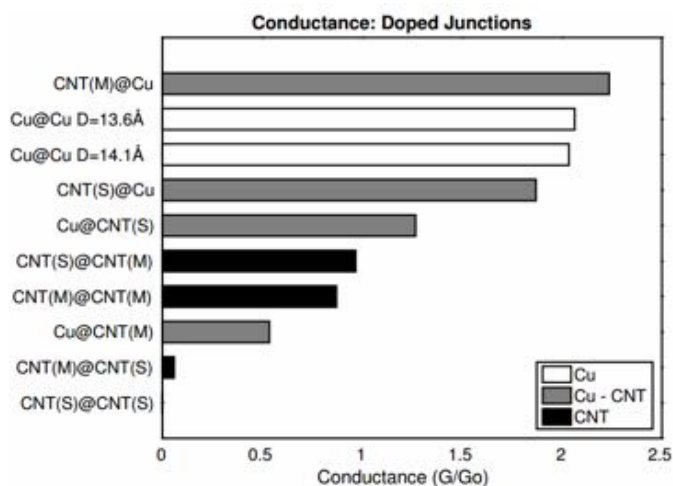


Fig. 16. Conductance of the doped junctions

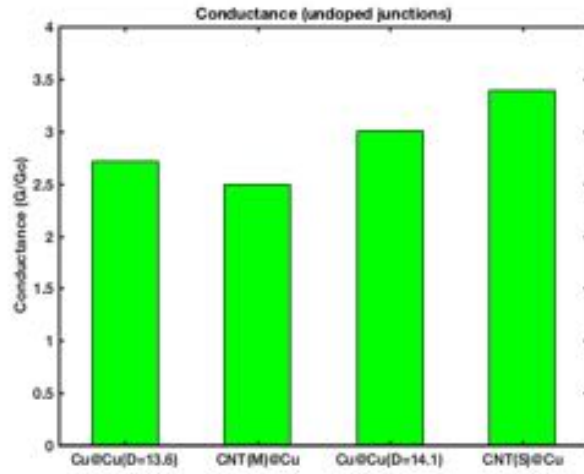


Fig. 17. Conductance of the undoped junctions

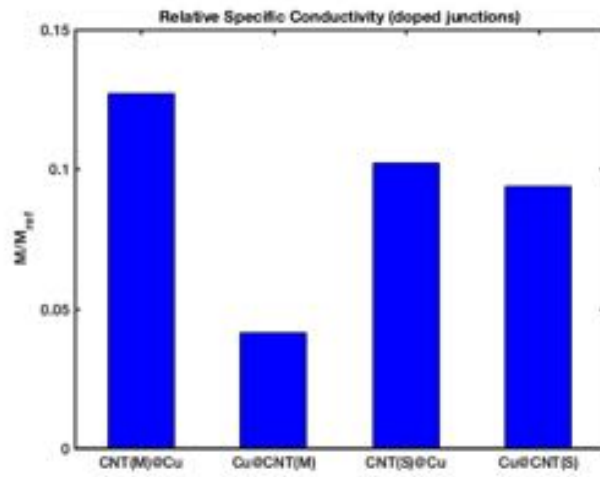


Fig. 18 Relative specific conductivity, doped Cu-CNT

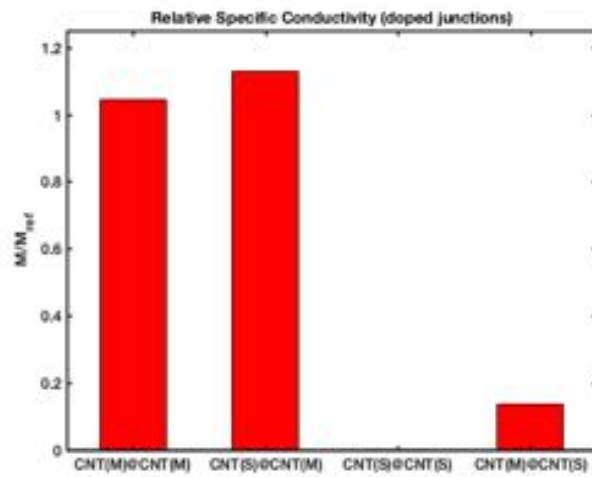


Fig. 19 Relative specific conductivity, doped CNT

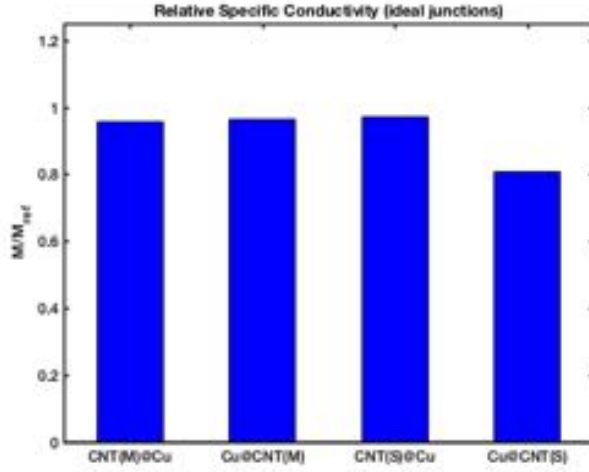


Fig. 20 Relative specific conductivity, ideal Cu-CNT

Table 5. Nanowire model parameters for the double wall conductors

	$\frac{1}{R_c} \frac{1}{G_0}$	$\frac{1}{R_j} \frac{1}{G_0}$	$\hat{m}_c \left(\frac{amu}{\text{\AA}} \right)$	$L_j \text{ (\AA)}$
Cu@Cu D=13.6 \AA	21.64	2.06	774.6	2.46
CNT(M)@Cu	16.82	2.24	614.0	2.46
Cu@CNT(M)	12.54	0.54	453.4	2.46
Cu@Cu D=14.1 \AA	21.68	2.03	804.9	2.84
CNT(S)@Cu	17.78	1.87	638.1	2.84
Cu@CNT(S)	10.90	1.27	471.2	2.84
CNT(M)@CNT(M)	3.99	0.87	292.8	2.46
CNT(S)@CNT(S)	0.03	0.00	304.3	2.46
CNT(S)@CNT(M)	1.99	0.97	300.6	2.46
CNT(M)@CNT(S)	1.99	0.12	308.4	2.46

The performance of the doped nanowire models studied in this paper are compared in Figures 18 and 19, which plot relative specific conductivity versus nanowire type. Figure 18 shows the results for the four copper-CNT composites; in the case of these materials, the nanowire models underpredict experimentally measured performance by an approximate order of magnitude. Figure 19 shows the nanowire modeling results for the four different CNT conductor configurations. Assuming that the CNT conductors incorporate a uniform mix of metallic and semiconducting nanotubes, the estimated experimental performance is the average of the four bars indicated in Figure 19, namely a specific conductivity 58 percent of that for copper. This shows good agreement with published data (Table 2) on performance of doped CNT fibers, although the dopants (acid and iodine, [10]) differed from the transmission metal doping modeled in this paper. The first bar of Figure 19 suggests that composite wiring fabricated using only metallic nanotubes may realize a greatly improved performance, estimated at 104 percent of the specific conductivity of pure copper. This computational result is consistent with

the recommendations of the last cited experimental reference, which highlighted the potential advantages of CNT conductor fabrication using a pure armchair feedstock.

In an effort to determine the source of the error in the predicted performance of the copper-CNT composites, the calculations used to generate Figure 18 were repeated, assuming that the modeled system incorporated “ideal” junctions: zero dopant mass ($m_d = 0$) and zero junction resistance ($R_j = 0$). The results obtained by introducing this assumption, plotted in Figure 20, are in broad agreement with the experimental data (Table 2). Assuming that the copper-CNT conductors incorporate a uniform mix of metallic and semiconducting nanotubes, the estimated experimental performance is now the average of the four bars indicated in Figure 20, namely a specific conductivity 93 percent of that for copper. It appears that the modeled Cu-CNT junctions are not representative of the physical system, and that the actual junctions present in the tested Cu-CNT composites have a resistance which is negligible. The first two bars of Figure 20 suggest that composite wiring fabricated using only metallic nanotubes may realize a slightly improved performance, estimated at 96 percent of the specific conductivity of pure copper.

The reasons for the current paper’s apparent overestimation of junction resistance effects in copper-CNT composites are a subject for future research, however the authors suggest that at least two factors are important: (1) actual junction overlap in copper-CNT composites may be much larger than the 2-3 angstrom overlap modeled in the current paper, and (2) junction conductance at non-zero voltage bias may be much higher than that predicted by the zero-bias calculations presented in the current paper. Although long junction overlaps and non-zero voltage bias will increase the already high computational cost of the models considered in this paper, understanding junction performance in copper-CNT composites is a subject clearly of central interest in future research.

6 CONCLUSIONS

This section presents general conclusions on the copper-CNT systems and CNT conductor systems analyzed in this paper.

With regards to the copper-CNT composite systems:

- a mass specific conductivity approximately 93 percent of that of pure copper is predicted by representing the composite structure as a collection of double wall tubes, composed of a uniform mix of copper-metallic and copper-semiconducting CNT’s, connected by ideal junctions
- composite fabrication using pure metallic CNT’s, as opposed to a metallic-semiconducting mix of CNT’s, will only slightly improve conductor performance

With regards to the CNT-CNT conductor systems:

- a mass specific conductivity approximately 58 percent of that of pure copper is predicted by representing the structure as a uniform mix of metallic and semiconducting double wall CNT’s, connected by doped junctions
- composite fabrication using pure metallic CNT’s, as opposed to a metallic-semiconducting mix of CNT’s, can improve conductor performance to 104 percent of that of pure copper

Although the modeling work presented in this paper incorporated significant assumptions, validity of the models is supported by:

- matching exact solutions for the conductance of double wall metallic CNT’s, double wall semiconducting CNT’s, and double wall metallic-semiconducting CNT’s (in two configurations),
- matching handbook data for room temperature copper (in two configurations) using a nanowire model incorporating both computed ballistic conductance properties for nanotubes and published data on the mean free path of pure copper, and
- broad agreement with experimental data on the macroscale performance of Cu-CNT composite conductors and CNT conductors.

The nanowire models presented in this paper assumed minimal conductor overlap, zero voltage bias, and only chromium as a dopant. Additional computational research focused on larger overlaps, nonzero voltage bias, and other dopants [39,40] is needed. As is common practice, the DFT modeling work presented in this paper assumed zero temperature conditions. Since the macroscale experimental data used in the validations is necessarily collected at finite temperatures, future investigation of temperature effects is also needed. Although finite temperature DFT methods have been developed [52], their added cost and complexity make them unattractive for use initial modeling efforts on complex systems. An important motivation for the application of finite temperature DFT methods is the study of thermal stability for nanocomposite dopants.

ACKNOWLEDGMENTS

This work was supported by the Office of Naval Research (Grant N00014-15-1-2693). Computer time support was provided by the Texas Advanced Computing Center at the University of Texas at Austin.

REFERENCES

- [1] J. M. Wernik and S. a. Meguid, 2010, "Recent Developments in Multifunctional Nanocomposites Using Carbon Nanotubes," *Appl. Mech. Rev.*, **63** (5), p. 50801.
- [2] M. F. L. De Volder, S. H. Tawfick, R. H. Baughman, and A. J. Hart, 2013, "Carbon nanotubes: present and future commercial applications.," *Science*, **339** (6119), pp. 535–539.
- [3] X. Wang, N. Behabtu, C. C. Young, D. E. Tsentlovich, M. Pasquali, and J. Kono, 2014, "High-ampacity power cables of tightly-packed and aligned carbon nanotubes," *Adv. Funct. Mater.*, **24** (21), pp. 3241–3249.
- [4] C. Subramaniam *et al.*, 2013, "One hundred fold increase in current carrying capacity in a carbon nanotube-copper composite.," *Nat. Commun.*, **4**, p. 2202.
- [5] Y. Zhao, J. Wei, R. Vajtai, P. M. Ajayan, and E. V Barrera, 2011, "Iodine doped carbon nanotube cables exceeding specific electrical conductivity of metals.," *Sci. Rep.*, **1** (c), p. 83
- [6] W. S. B. Meguid, S. A. Meguid, Z. H. Zhu, and M. J. 2011, "Modeling electrical conductivities of nanocomposites with aligned carbon nanotubes," *Nanotechnology*, **22** (48), p. 485704
- [7] X. J. Du, Z. Chen, J. Zhang, C. S. Yao, C. Chen, and X. L. Fan, 2012, "Structural and electronic properties of conducting Cu nanowire encapsulated in semiconducting zigzag carbon nanotubes: A first-principles study," *Phys. Status Solidi Basic Res.*, **249** (5), pp. 1033–1038.
- [8] C. Yang, 2013, "First Principle Studies of Cu-Carbon Nanotube Hybrid Structures with Emphasis on the Electronic Structures and the Transport Properties," Ph.D. Thesis, University of Central Florida.
- [9] M. Ghorbani-Asl, P. D. Bristowe, and K. Koziol, 2015, "A computational study of the quantum transport properties of a Cu-CNT composite," *Phys. Chem. Chem. Phys.*, **17** (28), pp. 18273–18277.
- [10] N. Behabtu *et al.*, 2013, "Strong, light, multifunctional fibers of carbon nanotubes with ultrahigh conductivity," *Science*, **339** (6116), pp. 182–186.
- [11] J. N. Wang, X. G. Luo, T. Wu, and Y. Chen, 2014, "High-strength carbon nanotube fibre-like ribbon with high ductility and high electrical conductivity," *Nat. Commun.*, **5** (2005), p. 3848.
- [12] A. Lopez-Bezanilla, 2013, "Electronic Transport Properties of Chemically Modified Double-Walled Carbon Nanotubes," *J. Phys. Chem. C*, **117**, pp. 15266–15271.
- [13] C. Yang and Q. Chen, 2017, "Electronic structure and transport properties of carbon nanotube adsorbed with a copper chain," *Int. J. of Smart and Nano Materials*, Vol. 4, No. 3, pp.143-149.
- [14] X. Du, Z. Chen, J. Zhang, C.-S. Yao, C. Chen, and X.-L. Fan, 2012, "Structural and electronic properties of conducting Cu nanowire encapsulated in semiconducting zigzag carbon nanotubes: A first-principles study," *Phys. Status Solidi B*, Vol. 249, No. 5, pp. 1033-1038.
- [15] Q. Yan, J. Wu, G. Zhou, W. Duan, and B.-L. Gu, 2005, "Ab initio study of transport properties of multiwalled carbon nanotubes," *Phys. Rev. B*, **72** (15), p. 155425.
- [16] R. Moradian, S. Azadi, and H. Refii-tabar, 2007, "When double-wall carbon nanotubes can become metallic or semiconducting," *J. Phys.: Condens. Matter* **19**, 176209.
- [17] M. Soto, T.A. Boyer, S. Biradar, L. Ge, R. Vajtai, A. Elías-Zúñiga, P.M. Ajayan and E.V. Barrera, 2015, "Effect of interwall interaction on the electronic structure of double-walled carbon nanotubes," *Nanotechnology*, Vol. 26, 165201.
- [18] E. Y. Li and N. Marzari, 2011, "Improving the electrical conductivity of carbon nanotube networks: A first-principles study," *ACS Nano*, **5** (12), pp. 9726–9736.
- [19] C. Buia, A. Buldum, and J. P. Lu, 2003, "Quantum Interference Effects in Electronic Transport through Nanotube Contacts," *Phys. Rev. B*, **67** (January), pp. 113409–113412.
- [20] F. Xu, A. Sadrzadeh, Z. Xu, and B. I. Yakobson, 2013, "Can carbon nanotube fibers achieve the ultimate conductivity? - Coupled-mode analysis for electron transport through the carbon nanotube contact," *J. Appl. Phys.*, **114** (6).
- [21] A. Buldum and J. P. Lu, 2001, "Contact resistance between carbon nanotubes," *Phys. Rev. B Condens. Matter*, **63** (16), p. 161403(1-4).
- [22] P. L. M. S. Fuhrer, J. Nygård, L. Shih, M. Forero, Young-Gui Yoon, M. S. C. Mazzoni, Hyoung Joon Choi, Jisoon Ihm, Steven G. Louie, A. Zettl, McEuen, 2000, "Crossed Nanotube Junctions," *Science*, **288** (5465), pp. 494–497.

- [23] J. M. Soler *et al.*, 2002, “The SIESTA method for ab initio order- N materials simulation,” *J. Phys. Condens. Matter*, **14** (11), p. 2745.
- [24] J. P. Perdew, K. Burke, and M. Ernzerhof, 1996, “Generalized Gradient Approximation Made Simple,” *Phys. Rev. Lett.*, **77** (18), pp. 3865–3868.
- [25] J. D. Pack and H. J. Monkhorst, 1976, “Special points for Brillouin-zone integrations,” *Phys. Rev. B*, **13** (4), pp. 5188–5192.
- [26] S. Datta, 2000, “Nanoscale device modeling: the Green’s function method,” *Superlattices Microstruct.*, **28** (4), pp. 253–278.
- [27] Y. Imry and R. Landauer, 1999, “Conductance viewed as transmission,” *Rev. Mod. Phys.*, **71** (2), pp. S306–S312.
- [28] Y. B. Band and Y. Avishai, 2012, *Quantum Mechanics with Applications to Nanotechnology and Information Science*, 1st ed., Elsevier.
- [29] J. Kong *et al.*, 2001, “Quantum interference and ballistic transmission in nanotube electron waveguides,” *Phys. Rev. Lett.*, **87** (10), p. 106801.
- [30] K. Stokbro, J. Taylor, M. Brandbyge, and P. Ordejón, 2003, “TranSIESTA: A Spice for Molecular Electronics,” in *Annals of the New York Academy of Sciences*, **1006**, pp. 212–226.
- [31] X. Lu and Z. Chen, 2005, “Curved Pi-conjugation, aromaticity, and the related chemistry of small fullerenes (<C60) and single-walled carbon nanotubes,” *Chem. Rev.*, **105** (10), pp. 3643–3696.
- [32] X. Blase, L. X. Benedict, E. L. Shirley, and S. G. Louie, 1994, “Hybridization effects and metallicity in small radius carbon nanotubes,” *Phys. Rev. Lett.*, **72** (12), pp. 1878–1881.
- [33] Y. Baskin and L. Meyer, 1955, “Lattice constants of graphite at low temperatures,” *Phys. Rev.*, **100** (2), p. 544.
- [34] K. E. Moore, D. D. Tune, and B. S. Flavel, 2015, “Double-walled carbon nanotube processing,” *Adv. Mater.*, **27** (20), pp. 3105–3137.
- [35] K. Liu *et al.*, 2014, “Van der Waals-coupled electronic states in incommensurate double-walled carbon nanotubes,” *Nat. Phys.*, **10** (10), pp. 737–742.
- [36] Y. Hanaoka, K. Hinode, K. Takeda, and D. Kodama, 2002, “Increase in Electrical Resistivity of Copper and Aluminum Fine Lines,” *Mater. Trans.*, **43** (7), pp. 1621–1623.
- [37] J. Y. Park *et al.*, 2004, “Electron-phonon scattering in metallic single-walled carbon nanotubes,” *Nano Lett.*, **4** (3), pp. 517–520.
- [38] D. Mann, A. Javey, J. Kong, Q. Wang, and H. Dai, 2003, “Ballistic Transport in Metallic Nanotubes with Reliable Pd Ohmic Contacts,” *Nano Lett.*, **3** (11), pp. 1541–1544.
- [39] D. Janas, A. P. Herman, S. Boncel, and K. K. K. Koziol, 2014, “Iodine monochloride as a powerful enhancer of electrical conductivity of carbon nanotube wires,” *Carbon N. Y.*, **73** (February 2014), pp. 225–233.
- [40] D. Janas, K. Z. Milowska, P. Bristowe, and K. Koziol, 2017, “Improving the electrical properties of carbon nanotubes with interhalogen compounds,” *Nanoscale*, **44** (27), pp. 3212–3221.
- [41] Chuong V. Nguyen, Nguyen N. Hieu, and Duong T. Nguyen, “Dispersion-Corrected Density Functional Theory Investigations of Structural and Electronic Properties of Bulk MoS₂: Effect of Uniaxial Strain,” *Nanoscale Research Letters* (2015) 10:433.
- [42] Yuki Matsuda, Jamil Tahir-Kheli, and William A. Goddard, III, “Definitive Band Gaps for Single-Wall Carbon Nanotubes,” *J. Phys. Chem. Lett.* 2010, **1**, 2946–2950.
- [43] Yan Li, Slava V. Rotkin, and Umberto Ravaioli, “Electronic Response and Bandstructure Modulation of Carbon Nanotubes in a Transverse Electrical Field,” *Nano Letters*, 2003, Vol. 3, No. 2, pp. 183–187.
- [44] Li, Yanchuan, Ab initio Study of Carbon Nanotube Based Conductors, Master of Science Thesis, Department of Mechanical Engineering, University of Texas at Austin, May 2017.
- [45] Andrew Pollack, Sufian Alnemrat, Thomas W. Chamberlain, Andrei N. Khlobystov, Joseph P. Hooper, and Sebastian Osswald, “Electronic Property Modification of Single-Walled Carbon Nanotubes by Encapsulation of Sulfur-Terminated Graphene Nanoribbons,” *Small*, 2014, **10**, No. 24, pp. 5077–5086.
- [46] V. Zólyomi and J. Kürti, “First-principles calculations for the electronic band structures of small diameter single-wall carbon nanotubes,” *Physical Review B*, **70**, 085403 (2004).
- [47] Min Ouyang, Jin-Lin Huang, Chin Li Cheung, Charles M. Lieber, “Energy Gaps in “Metallic” Single-Walled Carbon Nanotubes,” *Science*, Vol. 292, 27 April 2001, pp. 702–705.
- [48] Min Ouyang, Jin-Lin Huang, and Charles M. Lieber, “Scanning Tunneling Microscopy Studies of the One-Dimensional Electronic Properties of Single-Walled Carbon Nanotubes,” *Annu. Rev. Phys. Chem.* 2002. **53**:201–20.
- [49] Grimme, Stefan, “Density functional theory with London dispersion corrections,” *WIREs Computational Molecular Science*, Volume 1, March/April 2011, pp.211–228.
- [50] G.B. Abadir, K. Walus, D.L. Pulfrey, “Basis-set choice for DFT/NEGF simulations of carbon nanotubes,” *J Comput Electron* (2009) **8**: 1–9.
- [51] Wei Song, Ming Ni, Jing Lu, Zhengxiang Gao, Shigeru Nagase, Dapeng Yu, Hengqiang Ye, Xinwei Zhang, “Electronic structures of semiconducting double-walled carbon nanotubes: Important effect of interlayer interaction,” *Chemical Physics Letters* 414 (2005) 429–433.

- [52] Álvaro Ruiz-Serrano and Chris-Kriton Skylaris “A variational method for density functional theory calculations on metallic systems with thousands of atoms,” *Journal of Chemical Physics*, 2013, Vol. 139, 054107.
- [53] Berger, C., Ponchral, P., and De Heer, W., “Ballistic conduction in multiwalled carbon nanotubes,” *Journal of Nanoscience and Nanotechnology*, Vol. 3, No. 1 and 2, pp. 171-177.
- [54] Xin Lu and Zhongfang Chen, “Curved Pi-Conjugation, Aromaticity, and the Related Chemistry of Small Fullerenes (<C60) and Single-Walled Carbon Nanotubes,” *Chemical Reviews*, 2005, Vol. 105, No. 10.
- [55] Rundong Wan, Jin-hui Peng, Xiaocong Zhang, Chongyan Leng, “Band gaps and radii of metallic zigzag single wall carbon nanotubes,” *Physica B* 417 (2013) 1-3.

Nonholonomic Formulation of Ab Initio Molecular Dynamics

Eric P. Fahrenthold

Department of Mechanical Engineering, University of Texas
Austin, TX, 78712, epfahren@mail.utexas.edu

January 15, 2019

ABSTRACT

A new nonholonomic Hamiltonian formulation of ab initio molecular dynamics extends current Ehrenfest, Car-Parrinello, and Born-Oppenheimer formulations, offering potential improvements to modeling methods employed in computational materials design.

1 INTRODUCTION

A wide variety of continuum, mesoscale, molecular dynamics, and quantum mechanics methods have been applied to computational materials design problems. The most fundamental methods model both the nuclei and the electronic structure using quantum mechanics. Somewhat less general approaches, normally labeled ‘ab initio molecular dynamics,’ model the nuclei as a classical subsystem linked to a quantum description of the electrons.

Within the latter class of methods, the established modeling approaches are generally categorized as either Born-Oppenheimer, Car-Parrinello, or Ehrenfest formulations [1]. The three approaches are distinguished by a further gradation in modeling assumptions. Born-Oppenheimer molecular dynamics approximates transient variations in the electronic structure by solving a time-independent wave equation for each nuclear configuration. Car-Parrinello molecular dynamics models the nuclear and electronic degrees of freedom as a fully transient coupled system, but achieves this objective by introducing a fictitious inertia for the electronic structure. Ehrenfest molecular dynamics solves a time dependent quantum wave equation for the electronic structure, but assumes that the nuclear forces due to the time varying electronic structure are conservative: they are obtained by taking the derivative of an electronic Hamiltonian with respect to the nuclear coordinates. The widespread use of these methods, as compared to fully quantum models, in science and engineering applications

motivates interest in the further development of ab initio molecular dynamics formulations.

This technical note describes a new formulation of ab initio molecular dynamics. Distinct from the aforementioned approaches, it offers the following combination of modeling features: (1) the nuclear and electronic degrees of freedom are modeled as a fully transient coupled classical-quantum system, (2) no fictitious inertia is introduced, and (3) the nuclear forces due to the time varying electronic structure are derived from a rate constrained Hamiltonian analysis of the modeled system, and include both conservative and nonconservative forces. The generalization described here is enabled by: (1) introducing a nonholonomic model formulation approach [2], and (2) recognizing the existence and importance of the degenerate Hamilton's equations [3,4,5] associated with the absence of electronic momentum states. The development which follows builds upon the last cited research, conducted by the author and co-workers, formulating, implementing, and validating models for a variety of physical systems (at different scales and in various reference frames) using a nonholonomic Hamiltonian modeling methodology.

2 MODEL FORMULATION

The quantum-classical system considered here is a set of n nuclei and a set of n_e electrons in an isokinetic ensemble. The system Hamiltonian (H) is the sum of the nuclear kinetic energy (T_n), the nuclear potential energy (V_n), and the quantum mechanics expression for the total electronic energy (E_e)

$$H = T_n + V_n + E_e \quad (1)$$

The nuclear kinetic co-energy and nuclear momenta are

$$T_n^* = \frac{1}{2} \sum_{i=1}^n M^{(i)} \dot{\mathbf{q}}^{(i)2}, \quad \mathbf{p}^{(i)} = \frac{\partial T_n^*}{\partial \dot{\mathbf{q}}^{(i)}} \quad (2)$$

where $M^{(i)}$ is a nuclear mass and $\mathbf{q}^{(i)}$ is a nuclear center of mass position vector. The nuclear potential energy $V_n(\mathbf{q})$ includes electrostatic repulsion of the nuclei and the effects of any external potential. The quantum mechanics expression for the electronic energy includes electron repulsion, electron-nuclear attraction, and electron kinetic energy. It is computed from the electronic wave function Ψ and the electronic Hamiltonian operator H_e using the expectation value expression (expressed in Dirac bracket notation)

$$E_e = \frac{\langle \Psi | H_e | \Psi \rangle}{\langle \Psi | \Psi \rangle}, \quad H_e = -\frac{\hbar^2}{m_e} \sum_{j=1}^{n_e} \nabla_j^2 + V_e \quad (3)$$

where \hbar is the reduced Planck constant, m_e is an electron mass, and V_e is an electronic potential energy. If the wave function is interpolated using a set of n_s

basis functions (ϕ_j) which depend in general on the nuclear positions and the space coordinates (\mathbf{x}), then

$$\Psi = \sum_{j=1}^{n_s} c^{(j)} \phi_j(\mathbf{q}, \mathbf{x}) \quad (4)$$

where the parameters $c^{(j)}(t)$ are the time dependent weighting coefficients of the basis set. The electronic energy now takes the functional form $E_e(\mathbf{q}, \mathbf{c})$, where \mathbf{q} and \mathbf{c} are system level vectors of nuclear and electronic generalized coordinates. Evolution equations for the time dependent basis coefficients are obtained by discretization of the Schrodinger equation

$$i\hbar \frac{\partial \Psi}{\partial t} = H_e \Psi \quad (5)$$

Introducing the wave function interpolation, multiplying the Schrodinger equation by the complex conjugate basis function ϕ_k^* (the superscript denotes the complex conjugate), and integrating over the modeled volume provides the discrete evolution equations

$$\mathbf{A}\dot{\mathbf{c}} + \mathbf{B}\dot{\mathbf{q}} = \mathbf{H}\mathbf{c} \quad (6)$$

where the matrix coefficients are

$$A_{kj} = i\hbar \int \phi_k^* \phi_j d\tau, \quad H_{kj} = \int \phi_k^* H_e \phi_j d\tau \quad (7)$$

with $d\tau$ a differential volume, and

$$B_{kj} = i\hbar \sum_{l=1}^{n_s} c^{(l)} \int \phi_k^* \frac{\partial \phi_l}{\partial q^{(j)}} d\tau \quad (8)$$

If the basis functions are orthogonal (no such assumption is made here), the matrix \mathbf{A} is diagonal. The dynamics of the classical nuclear and quantum electronic subsystems may now be coupled using a nonholonomic modeling approach.

The canonical Hamilton's equations [2] for the mixed classical-quantum system are

$$\dot{\mathbf{p}} = -\frac{\partial H}{\partial \mathbf{q}} + \mathbf{f}^q, \quad \dot{\mathbf{q}} = \mathbf{M}^{-1}\mathbf{p} \quad (9)$$

where \mathbf{p} denotes a system level vector of nuclear momenta (the inertia matrix \mathbf{M} is diagonal) and

$$\mathbf{0} = -\frac{\partial H}{\partial \mathbf{c}} + \mathbf{f}^c \quad (10)$$

which are the momentum balance equations associated with the electronic coordinates. The vectors \mathbf{f}^q and \mathbf{f}^c are generalized nonconservative forces, to be determined by the net power flow to the system and the nonholonomic constraints.

The momentum balance equations associated with the electronic coordinates take a degenerate form [3,4,5], since the electronic momenta [and their time derivatives, hence the left hand side of equation (10)] are identically zero. Although the later equations have been overlooked in previous ab initio molecular dynamics work, they are in fact of central importance, since they allow the Lagrange multipliers associated with the nonholonomic constraints (the discrete Schrodinger equations) to be determined in closed form.

In the isokinetic ensemble case, the power flow to the ensemble (P^{ext}) takes a thermal form. Assuming a simple functional form which depends on an overall heat transfer coefficient R , the ensemble temperature θ , and a source temperature θ_e ,

$$P^{ext} = \theta \dot{S} = R(\theta_e - \theta) = \mathbf{f}^T \dot{\mathbf{q}} \quad (11)$$

where \dot{S} is the entropy flow to the ensemble and \mathbf{f} is a vector of thermal forces. If the ensemble temperature is defined by (k_B is Boltzman's constant)

$$\theta = \sum_{i=1}^n \frac{1}{3nk_B} M_i \dot{\mathbf{q}}^{(i)2} = \frac{1}{3nk_B} \mathbf{p}^T \dot{\mathbf{q}} \quad (12)$$

then equations (11) and (12) determine the net entropy flow and the nonconservative thermal forces to be

$$\dot{S} = R \left(\frac{\theta_e}{\theta} - 1 \right), \quad \mathbf{f} = \frac{R}{3nk_B} \left(\frac{\theta_e}{\theta} - 1 \right) \mathbf{p} \quad (13)$$

Finally, taking the inner product of equation (6) with a vector of Lagrange multipliers λ , the coefficients of the generalized velocities in the resulting expression combine with equations (13) to determine [2] the generalized nonconservative forces in the canonical Hamilton's equations as

$$\mathbf{f}^c = \mathbf{A}^T \lambda, \quad \mathbf{f}^q = \mathbf{B}^T \lambda + \mathbf{f} \quad (14)$$

Equations (10) and (14) now determine, in closed form, the unknown vector of Lagrange multipliers. The final Hamilton's equations for the isokinetic ensemble are

$$\dot{\mathbf{p}} = -\frac{\partial H}{\partial \mathbf{q}} + \mathbf{B}^T \mathbf{A}^{-T} \frac{\partial H}{\partial \mathbf{c}} + \frac{R}{3nk_B} \left(1 - \frac{\theta_e}{\theta} \right) \mathbf{p} \quad (15)$$

$$\dot{\mathbf{q}} = \mathbf{M}^{-1} \mathbf{p} \quad (16)$$

$$\mathbf{A} \dot{\mathbf{c}} = -\mathbf{B} \mathbf{M}^{-1} \mathbf{p} + \mathbf{H} \mathbf{c} \quad (17)$$

The preceding development is the first to exploit nonholonomic Hamiltonian methods to formulate a general ab initio molecular dynamics model of a mixed classical-quantum system.

3 CONCLUSION

Applications of nonholonomic methods in molecular dynamics have to date been rather limited, and focused on thermostats [6,7]. Despite this fact, nonholonomic methods may have other important applications in computational chemistry, for example in the development of time adaptive basis functions [8,9]. Previous work in other science and engineering fields, including both rigid body [2] and deformable body [3,4,5] dynamics, has demonstrated the practical importance of nonholonomic Hamiltonian methods in those fields. To evaluate the general utility of nonholonomic methods in ab initio molecular dynamics, numerical implementation and validation research (extending beyond the model formulation work presented here) will be required.

ACKNOWLEDGEMENTS

This work was supported by the Office of Naval Research (Grant Number N00014-15-1-2693).

References

- [1] D. Marx and J. Hutter. Ab Initio Molecular Dynamics. Cambridge University Press, New York, 2009.
- [2] J.H. Ginsberg. Advanced Engineering Dynamics. Harper and Row, New York, 1988.
- [3] R.J. Hernandez and E.P. Fahrenthold, “Hybrid particle-element method for an unstructured hexahedral mesh,” International Journal for Numerical Methods in Engineering, Vol. 94, 2013, pp. 1191-1215.
- [4] M.E. Shimek and E.P. Fahrenthold, “Impact Dynamics Simulation for Multilayer Fabrics of Various Weaves,” AIAA Journal, Vol. 53, No. 7, July 2015, pp. 1793-1811.
- [5] C.R. Hean and E.P. Fahrenthold, “Discrete Lagrange equations for reacting thermofluid dynamics in arbitrary Lagrangian-Eulerian frames,” Computer Methods in Applied Mechanics and Engineering, Vol. 313, 2017, pp. 303-320.
- [6] R. Kutteh and R. B. Jones, “Rigid body molecular dynamics with nonholonomic constraints: Molecular thermostat algorithms,” Physical Review E, Vol. 61, No. 3, 2000, pp. 3186-3198.
- [7] A.G. Rojo and A.M. Bloch, “Nonholonomic double-bracket equations and the Gauss thermostat,” Physical Review E, Vol. 80, 2009, 025601.
- [8] P.W. Atkins and R. Friedman. Molecular Quantum Mechanics. Oxford University Press, New York, 2011.

- [9] E.P. Fahrenthold, “Nonholonomic Ab Initio Molecular Dynamics for Computational Materials Design,” proceedings of the TechConnect Conference, Washington DC, May 22-25, 2016.

Molecular Doping of Carbon Nanotube Wiring - Part I: Conductors

Khai Yi Chin

Department of Mechanical Engineering
University of Texas
Austin, Texas 78705
Email: khaiyichin@utexas.edu

Eric Fahrenthold

Department of Mechanical Engineering
University of Texas
Austin, Texas 78705
Email: epfahren@austin.utexas.edu

ABSTRACT

Carbon nanotubes (CNTs) show attractive electronic properties that have been studied extensively, including interest for cabling and wiring applications. Specifically, CNTs may provide an advantage over conventional materials, such as copper, due to their lightness and flexibility, which are properties demanded in naval and aircraft applications. Using molecular doping with the potassium tetrabromaurate molecule (KAuBr_4), doped nanowires with enhanced electrical properties may be obtained. This paper presents the first comprehensive modeling effort on KAuBr_4 doping of CNTs, including doping of SWNT junctions.

The potassium tetrabromaurate molecule (KAuBr_4), potassium atom (K), tetrabromaurate fragment (AuBr_4), potassium ion (K^+), and tetrabromaurate ion (AuBr_4^-) were tested as dopants on the SWNT based conductors. While the ions have do not affect the conductors, the charge neutral dopants were able to enhance the conductance of the doped SWNT conductors. Subsequently, a nanowire model based on the computational results show dramatic improvement over experimental data and copper in terms of specific conductivity. Overall, results presented in this paper show the promise of doped SWNTs as potential candidates for the replacement of conventional copper conductors.

1 Introduction

Carbon nanotubes (CNTs) have attracted much attention since physicist Sumio Iijima identified hollow cylindrical carbon structures in 1991 [1]. Since then, research on the material has escalated in order to study its unique properties. In particular, the electronic properties of CNTs show great promise, and provide an attractive prospect for applications like power transmission and consumer electronics. Specifically, conventional materials used in electrical applications, such as copper, are heavy and have poor mechanical properties; CNT-based wires may be able to resolve those complications with superior mechanical and electrical properties [2]. Recent research showed the advantage of doped CNT cables over conventional copper cables in terms of specific conductivity [3]; another paper showed a flexible and conductive CNT-based electrode [4]. This work on doped CNTs can contribute to the fabrication of highly conductive nanotubes in many of these applications.

In order to replace conventional conductive materials, the enhancement of electrical conductivity in CNTs is a highly researched topic. One way of enhancing the electrical conductivity is through the chemical doping of the CNTs. Some experimental studies of doped CNTs include I_2 , ICl , IBr [5], KAuBr_4 [6, 7], K , Br [8], and AuCl_3 doped [9] CNTs.

This paper explores the effect of potassium tetrabromaurate (KAuBr_4) on single-walled nanotube (SWNT) conductors, motivated by recent experimental efforts [6, 7] where CNT wires doped in a KAuBr_4 aqueous solution show improved conductivity over undoped CNT wires. (In this paper, the KAuBr_4 investigated has a gold oxidation number of +3, represented by the Roman numeral III [10].) Notably, the doped CNT wires showed increased conductivity, but decreased specific conductivity (specific conductivity is defined in a continuum as σ/ρ , where σ is the conductivity, and ρ is the mass density, of

the continuum). No computational work on KAuBr_4 as a CNT dopant was found at the time of this writing. Furthermore, the possibility of the KAuBr_4 molecule disassociating is considered, since the exact chemical makeup of the doped CNT is unknown. In this work, both the K atom and AuBr_4 fragment were included as potential dopants in the analysis.

K doping has been shown to improve the SWNT conductivity as well as its high-temperature stability (the change in conductivity was low across a wide range of temperatures) [8]. In that cited work however, the K doping process was limited to a small sample size; the procedure involved transferring the reacted sample into a cryostat, which limits the yield. This poses an obstacle for the fabrication of conductive wires, since a high volume of these wires is required. Alternative K doping methods have been found, however: K doped multi-walled nanotubes were produced through a reaction with a phenanthrene/K solution [11], which allows doping of larger volumes of CNTs. Moreover, the electronic structure of K doped SWNTs were investigated computationally [12]. In that work, the K atoms were positioned in the center of semiconducting SWNT conductors without structural relaxation. The researchers observed an upwards shift of the Fermi energy in the band structure, which is an indication of the n-doping of nanotubes by the K atoms. A different doping configuration for the K atoms is shown in this paper, for both the SWNT conductor and junction models.

The AuBr_4 fragment was not studied as a dopant for CNTs, but results on a similar dopant (AuCl_3) exist. Kim et al. found a decrease of sheet resistance in AuCl_3 doped CNT films with increasing dopant concentration, undergoing a decrease as much as 90% with an AuCl_3 concentration of 60 mM [9]. A further study using Raman and x-ray photoelectron spectroscopy showed that the element chlorine, rather than the gold, in the AuCl_3 molecule is responsible for the p-doping of the CNT, thus reducing the sheet resistance [13]. More recently, a computational study determined that it was neither the Cl nor the AuCl_3 (and Au_2Cl_6) that induced the p-doping, but the AuCl_4 [14]. Building upon that result, AuCl_4 doped conductors have been studied computationally and found to improve the conductance of the SWNT [15], but there were no computational studies on AuBr_4 doped SWNTs at the time of writing. In this work, that gap in knowledge will be bridged through the investigation of AuBr_4 doped SWNT conductors.

Apart from the neutral K atom and AuBr_4 fragment, their charged counterparts were modeled as well, namely, the K^+ and AuBr_4^- ion. The modeling of the charged dopants was motivated by the uncertainty in the doping configuration presented in [6, 7]: the doping solution used to produce the KAuBr_4 doped CNT in the two works was a KAuBr_4 aqueous solution, which raised the possibility of K^+ and AuBr_4^- as doping agents in the solutions. Hence the effect of charged dopants on SWNT conductors was investigated in this research.

In this research, two types of SWNTs were used to study the doping effects: the armchair SWNT of chirality (5,5) is the representative metallic SWNT, while the zigzag SWNT of chirality (8,0) is the representative semiconducting SWNT, both initialized as a rolled graphene sheet. The transport calculations for the conductors were done to replicate the conductance of an isolated SWNT. Once the doped SWNT conductors were analyzed, a nanowire model, based on a previous work [16], was then used to compare the computational results with the experimental work on KAuBr_4 CNT [7], and with copper as well.

The paper is organized as follows: Section 2 discusses the methodology used in investigating the models, Section 3 presents results on SWNT conductors. Section 4 compares this paper's results using a nanowire model, while conclusions are drawn in Section 5.

2 Methodology

Structural relaxation for all presented models was performed using the SIESTA 4.0 computational package, a self-consistent density functional theory (DFT) software that uses a basis set based on linear combinations of atomic orbitals (LCAO) [17]. In all cases, the atomic orbitals were double- ζ polarized. Exchange-correlation functionals were obtained using the Generalized Gradient Approximation (GGA) method, parametrized by Perdew, Burke, and Ernzerhof (PBE) [18], matched with an orbital energy shift $\Delta E_{PAO} = 150$ meV [19]. The k -grid mesh for structural relaxation was $1 \times 1 \times 1$, while the k -grid mesh for transport calculations was $1 \times 1 \times 4$. The relatively coarse mesh [15, 20] was selected due to the size of the computational models; a finer mesh ($1 \times 1 \times 4$ for structural relaxation) was tested; it was found that the difference in results was negligible ($< 2\%$), while the computation time was much longer (four times as long). The mesh cutoff energy was 300 Ry for both the structural relaxation and transport calculations [20]. Dispersion correction was not incorporated in the calculations of this paper, since there have been DFT studies that showed accurate SWNT band gap values without dispersion correction [21]. However, dispersion corrected models are of interest in future studies.

A computational unit cell under periodic boundary conditions was used for the relaxation and transport calculations. All models were relaxed until the maximum atomic force in the system was less than 0.04 eV \AA^{-1} . Transport calculations were performed with the TransSIESTA module included in the SIESTA 4.0 package, which computes the charge density matrix using Green's functions [22]. The conductance G is expressed in the form of the multichannel Landauer conductance

formula [23, 24]:

$$G = G_0 \int \left(-\frac{\partial f(E)}{\partial E} \right) T(E) dE, \quad T(E) = \text{Tr}[t^\dagger(E)t(E)], \quad (1)$$

where Tr is the trace operator, $t(E)$ is the transmission matrix, † is the conjugate transpose operator, $\text{Tr}[t^\dagger(E)t(E)]$ is the transmission amplitude at energy E , $f(E)$ is the Fermi-Dirac distribution, and the conductance quantum is

$$G_0 = \frac{2e^2}{h} = 7.748 \times 10^{-5} \text{ S}, \quad (2)$$

where e is the elementary charge, and h is Planck's constant. All results presented in this work were computed at zero temperature conditions, and thus Eqn. (1) becomes [23]

$$G = T(E_F)G_0. \quad (3)$$

In order to perform the transport calculations, each model was split into three regions: two end electrodes (one on each end) and the central scattering region. The end electrodes used in all calculations are extensions of the central scattering region, i.e., they are of the same species and configuration, instead of a different element (e.g. gold electrodes with a SWNT central scattering region). This is because of the intention is to simulate macro-scale CNT conductors, which can be approximated as infinitely long. Furthermore, the inclusion of buffer atoms is required when using bulk electrodes of a different species, which will further enlarge the model size and prolong the computation time. The electrodes range from 2 to 3 unit cells in length, depending on the model and dopant size, and are semi-infinite: they extend to infinity on ends that are not connected to the scattering region, via periodic images.

3 Conductor Models

In order to observe the effects of different dopants on the conductance, SWNT conductor models were tested. Motivated by the experimental efforts of KAuBr₄ doped CNTs [6, 7], a KAuBr₄ dopant was chosen in an attempt to shed light on the mechanism behind the improvement of the electrical conductivity of the nanotubes. As the exact dopant standoff and dopant type were unknown, the possibility of the K atoms and AuBr₄ fragments disassociating from their KAuBr₄ form in the doping solution was considered. Besides, the doping solution, which is a KAuBr₄ aqueous solution, also raised the possibility of K⁺ and AuBr₄⁻ ions as doping agents in the solution. Hence, the conductance of the undoped, KAuBr₄ doped, K doped, AuBr₄ doped, K⁺ doped, and AuBr₄⁻ doped SWNT conductors is presented in this section.

Prior to transport calculations, structural relaxation was performed on all the models. The SWNT conductors were relaxed in an isolated environment, i.e., the undoped/doped conductors were relaxed in a large computational unit cell to prevent interactions between the periodic images. The SWNT conductors modeled are 20 Å away from the walls in the x - and y -directions, while the z -walls were positioned such that the periodic images of the computational unit cell simulate a continuous and infinitely long SWNT conductor. Once relaxed, transport calculations were carried out on the SWNT conductor models in the same computational unit cell. Transport calculations for the ion doped conductors were done by initializing the models as electron-deficient or -surplus, respectively, for the K⁺ and the AuBr₄⁻ cases.

As mentioned in Section 1, there is a great interest in the specific conductivity of the doped models, in addition to the conductance. In the conductor models, the transport calculations were performed with two isolated nanotubes; as such, the volume of the conductor models was not considered. Therefore, the results of conductance and specific conductance (instead of specific conductivity) of the modeled SWNT conductors are computed. The specific conductance of the conductors is defined by:

$$\hat{G}_c = \frac{G_c}{\hat{m}_c}, \quad \hat{m}_c = \frac{m_c}{L_c} \quad (4)$$

where G_c is the conductance of a SWNT conductor with mass per unit length of \hat{m}_c , L_c is the unit cell length of the conductor, and m_c is the unit cell mass of the conductor. The atomic masses of the different elements considered are listed in Table 1, obtained from [25].

The SWNT conductors were modeled with two different dopant concentrations; the concentration values depend on the dopant species. Note that in this work, dopant concentration is referred to as the number of atoms/fragments/molecules of

dopants per SWNT unit cell; Table 2 tabulates the dopant mass fractions for the different dopants, and the dopant concentrations.

The dopants were initialized at a distance of 1-1.1 Å from the nanotube surface, which was sufficient to induce inter-atomic interactions; in all the cases, the dopants relaxed to a distance further away from the initial position, shown in Table 2 as dopant standoff ($l_{dopant-SWNT}^*$).

3.1 Undoped Conductors

The SWNTs were initialized as a rolled graphene sheet with a carbon-carbon bond length of 1.42 Å, leading to diameters of 6.26 Å and 6.78 Å respectively for the (8,0) SWNT and the (5,5) SWNT, which match literature values [26]. In terms of band structures, the models are consistent with past work [21, 26]: the (8,0) SWNT has a band gap of 1.25 eV and the (5,5) SWNT has a zero band gap.

For the undoped cases, the (8,0) SWNT conductor has a conductance of zero at the Fermi energy E_F , while the (5,5) SWNT conductor has a conductance of $2G_0$ at E_F . These results match literature values [27, 28]. The mass per unit length for the undoped (8,0) SWNT is 90.160 amu Å⁻¹; similarly 97.601 amu Å⁻¹ for the (5,5) SWNT.

3.2 Potassium Tetrabromaurate Doped Conductors

The first doped SWNT conductor model studied was the KAuBr₄ doped conductor. The KAuBr₄ molecule spans the length of two unit cells in the (8,0) SWNT, and three unit cells in the (5,5) SWNT, shown in Figs. 1 and 2. Hence, the KAuBr₄ dopant concentrations tested were 0.50 and 1.00 molecules per unit cell for the (8,0) SWNT. Correspondingly, the dopant concentrations were 0.33 and 0.67 molecules per unit cell for the (5,5) SWNT. The dopant standoff, the doped mass per unit length, and the dopant mass fraction are listed in Table 2.

The KAuBr₄ molecule had mixed effects on the conductance of the SWNT conductor, as shown in Fig. 3. The (8,0) conductor was unaffected by the KAuBr₄ dopant: its conductance remained at zero. The (5,5) conductor showed an increase in conductance with KAuBr₄ doping: the conductance increased from $2G_0$ to $3G_0$ at 0.33 molecules per unit cell, and to $4G_0$ at 0.67 molecules per unit cell. Despite this effect, the specific conductance was not improved, due to the high mass of the KAuBr₄ molecule (the specific conductance of the (8,0) conductor was zero since the $G = 0$), as shown in Fig. 3. The dopant mass fraction for the KAuBr₄ was very large, going as high as 60% and 61% for the (8,0) and (5,5) conductors respectively. The equilibrium geometry of the dopant molecule differed between the KAuBr₄ doped (8,0) SWNT and the KAuBr₄ doped (5,5) SWNT, as shown in Figs. 1 and 2 respectively. In the (8,0) SWNT case, the K atoms in the KAuBr₄ molecule aligned into a single plane, whereas in the (5,5) SWNT case the K atoms moved away from the plane of the AuBr₄.

The KAuBr₄ molecule has been shown to improve the conductivity of CNTs [6, 7], consistent with the present work, noting that bulk SWNTs include both metallic and semiconducting nanotubes [29].

3.3 Potassium Doped Conductors

The second dopant considered was the K atom, disassociated from its KAuBr₄ form. The K atom spans the length of one unit cell in both the (8,0) and (5,5) SWNT conductors, as shown in Figs. 4 and 5. Hence, the dopant concentrations were 0.50 and 1.00 atoms per unit cell for both the (8,0) and (5,5) SWNT. The dopant standoff, the doped mass per unit length, as well as the dopant mass fraction are listed in Table 2.

The K doping had a positive effect on both the (8,0) and (5,5) SWNT conductors, as shown in Fig. 6. The (8,0) conductor saw an increase in conductance: the conductance increased from 0 to $1.6G_0$ at 0.50 atoms per unit cell, and to $2.5G_0$ at 1.00 atoms per unit cell. The (5,5) conductor also saw an increase in conductance: the conductance increased from $2G_0$ to $3G_0$ at 0.50 atoms per unit cell, and to $3.8G_0$ at 1.00 atoms per unit cell. The specific conductance of the (8,0) conductor was increased, going over the benchmark value of an undoped (5,5) SWNT at 1.00 atoms per unit cell, while the specific conductance of the (5,5) conductor exceeded the same benchmark at 0.50 and 1.00 atoms per unit cell, as shown on the right of Fig. 6. Since the K atom is relatively light, the dopant mass fraction was low for both semiconducting and metallic SWNT conductors, going only as high as 9% for the (8,0) conductor and 14% for the (5,5) conductor. Band structure analysis showed that there was an upwards shift in the Fermi energy, a sign of the n-doping of the SWNT conductor by the K atom. This led to an increase in electronic states available near the doped Fermi energy, and consequently an improvement in the conductance.

The positive effect of the K atom in the doped SWNT conductors is consistent with computational and experimental literature [8, 12].

3.4 Tetrabromaurate Doped Conductors

The third dopant investigated was the AuBr₄ fragment, the other disassociated part of the KAuBr₄ molecule. The AuBr₄ fragment spans the length of two unit cells in the (8,0) SWNT conductor, and three unit cells in the (5,5) SWNT conductor, as shown in Figs. 7 and 8. Hence, the AuBr₄ fragment concentrations tested were 0.50 and 1.00 fragments per unit cell

for the (8,0) SWNT conductor. The dopant concentrations were 0.33 and 0.67 fragments per unit cell for the (5,5) SWNT conductor. The dopant standoff, the doped mass per unit length, and the dopant mass fraction are listed in Table 2.

The AuBr_4 fragment had a positive effect on both the (8,0) and the (5,5) conductors, as shown in Fig. 9. The (8,0) conductor saw an increase in conductance: the conductance increased from 0 to $1.3G_0$ at 0.50 fragments per unit cell, and to $1.9G_0$ at 1.00 fragments per unit cell. The (5,5) conductor also saw an increase: the conductance increased from $2G_0$ to $3G_0$ at 0.33 fragments per unit cell, and to $0.67G_0$ at 0.67 fragments per unit cell. However, the specific conductance of both the (8,0) and (5,5) conductors were lower than the benchmark value for the undoped (5,5) SWNT, shown on the right of Fig. 9. Since the AuBr_4 fragment is heavy, the dopant mass fraction was high for both the semiconducting and metallic SWNT conductors, going as high as 57% for the (8,0) conductor and 59% for the (5,5) conductor. Band structure analysis showed that there was a downwards shift in the Fermi energy, a sign of p-doping of the SWNT conductor by the AuBr_4 fragment. This led to an increase in electronic states available near the doped Fermi energy, and consequently an improvement in the conductance.

The AuBr_4 fragment's effect is qualitatively consistent with the closest experimental work on AuCl_3 doping of CNT films [9]. In that work the authors observed a decrease in sheet resistance of the doped film over its undoped counterpart. It is also consistent with a related computational work on AuCl_4 , which exhibited improvement to its conductance of SWNT [15]. (Related work on AuBr_4 doped CNTs, computational or experimental, was not found.)

3.5 Potassium Ion Doped Conductors

Next, the ion dopants were studied, starting with the K^+ ion. The K^+ ion spans the length of one unit cell in both the (8,0) and (5,5) SWNTs, as shown in Figs. 10 and 11. Hence, the dopant concentrations were 0.50 and 1.00 ions per unit cell for both the (8,0) and (5,5) SWNT conductors. The dopant standoff, the doped mass per unit length, and the dopant mass fraction are listed in Table 2.

The K^+ ion had no effect on the conductance for both the (8,0) or the (5,5) SWNT conductors: the conductance of the (8,0) conductor remained at zero, while the conductance of the (5,5) conductor remained at $2G_0$. Consequently, the specific conductance decreased for the (5,5) conductor (the specific conductance of the (8,0) conductor stayed at zero), shown in Fig. 12. The dopant mass fraction introduced by the K^+ ion is identical to the K atom, since the mass of one electron is negligible; the maximum dopant mass fraction for the (8,0) conductor was 9%, and for the (5,5) conductor it was 14%.

There were no previous works on K^+ that was found; the closest computational result [12] focused on K as a charge neutral atom, which is different from the presented case of K^+ doped SWNT conductor (electron-deficient model).

3.6 Tetrabromoaurate Ion Doped Conductors

The final dopant, AuBr_4^- ion was studied. The AuBr_4^- ion spans the length of two unit cells in the (8,0) SWNT, and three unit cells in the (5,5) SWNT, as shown in Figs. 13 and 14. Hence, the AuBr_4^- dopant concentrations tested were 0.50 and 1.00 ions per unit cell for the (8,0) SWNT. Correspondingly, the dopant concentrations were 0.33 and 0.67 ions per unit cell for the (5,5) SWNT. The dopant standoff, the doped mass per unit length, and the dopant mass fraction are listed in Table 2.

The AuBr_4^- ion had no effect on the conductance, for both the (8,0) or the (5,5) SWNT conductor: the conductance of the (8,0) conductor remained at zero, while the conductance of the (5,5) conductor remained at $2G_0$. Consequently, the specific conductance decreased for the (5,5) conductor (the specific conductance of the (8,0) conductor stayed at zero), shown in Fig. 15. The dopant mass fraction introduced by the AuBr_4^- was high, which is the same as the AuBr_4 fragment: the maximum dopant mass fraction for the (8,0) conductor was 57%, and for the (5,5) conductor it was 59%. There were no previous works found for the AuBr_4^- ion as well.

The closest computational result is based on the AuCl_4 molecule [15], which is different from the presented case of AuBr_4^- doped SWNT conductor (electron-surplus model).

4 Nanowire Model

In order to connect the presented results in Section 3 with experimental efforts, a nanowire model was defined based on a previous work [16]. The conductors concerned were the KAuBr_4 , K, and AuBr_4 doped SWNT conductors; the ion doped models were left out due to their lack of influence on the conductance for the SWNT conductors. For the same reason, the (8,0) KAuBr_4 doped SWNT conductor (of both concentrations) were left out of consideration for the nanowire model.

The experimental reference of interest is the KAuBr_4 doped CNT in [7]. It is worth noting that due to the uncertainty of the doped CNT's chemical composition provided in the experimental reference, the nanowire model is not meant as a direct comparison; rather, the results show the possibility of the work presented in this paper as dopants for CNTs in the aforementioned experimental work.

The nanowire model is evaluated through its specific conductivity, defined by the metric M :

$$\frac{1}{M} = \frac{\rho}{\sigma} = \hat{m}_c \frac{R_c}{L_{MFP}} = \frac{1}{L_{MFP} \hat{G}_c} \quad (5)$$

where ρ is the mass density and σ is the conductivity of a continuum material, \hat{m}_c is the mass per unit length of the doped SWNT conductor, R_c is the conductor resistance (and its inverse G_c is the conductance; \hat{G}_c is the specific conductance defined in Eqn. (4)), and L_{MFP} is the electronic mean free path, set to 500 nm [30].

To properly gauge the performance of the nanowire, the specific conductivity of copper was used as a reference metric M_{ref} , obtained via the specific conductivity definition for continuum materials. Using only the mass density ρ and the conductivity σ , the specific conductivity of copper was found to be $M_{ref} = 6671.30 \text{ Sm kg}^{-1}$ [31]. The relative specific conductance, which is the ratio M/M_{ref} , was then compared among all doped SWNT conductors, including the experimental reference in [7].

Figures 16 and 17 show the performance of the nanowires. In all the tested cases, the nanowires outperform both the copper and experimental reference (whereby $M/M_{ref} = 0.7$). For the KAuBr₄ doped (5,5) nanowire, the relative specific conductance is about 6 times better than copper, lower than the benchmark set by the undoped (5,5) SWNT nanowire at $M/M_{ref} = 7.1$. As for the K doped nanowire, at 1.00 atoms per unit cell, both the (8,0) and the (5,5) nanowire exceeded the undoped nanowire benchmark, with the K doped (8,0) nanowire at $M/M_{ref} = 8.8$ and the (5,5) nanowire at $M/M_{ref} = 11.8$. However, for the AuBr₄ doped nanowire, the specific conductivity was lower than the undoped nanowire benchmark, with $M/M_{ref} \approx 3$ for the (8,0) nanowire and $M/M_{ref} \approx 6$ for the (5,5) nanowire.

Such a superiority in the performance of nanowire models was expected, since the model considers an ideal circumstance for the nanowire in the macro-scale, that the nanowires are continuously and infinitely long. Thus, to better capture the behavior of macro-scale wires, it is of interest to examine models that are not limited to just intratube electronic transmission, but also intertube electronic transmission: SWNT junctions. Furthermore, the exact doping configuration of the KAuBr₄ CNT in [7] is unknown, which could be a reason behind the discrepancy in nanowire performance. In the future, an investigation into nanowire models that include doped SWNT junctions will allow a better representation of the KAuBr₄ doped CNT.

5 Conclusions

The principal findings of this research on KAuBr₄, K, AuBr₄, K⁺ and AuBr₄⁻ doped models are presented in this section. From the SWNT conductor models, it was found that the K atom and the AuBr₄ fragment were the most effective in increasing the conductance of both the semiconducting (8,0) and the metallic (5,5) conductor. The KAuBr₄ molecule was only partially useful; the KAuBr₄ doped (5,5) conductor saw an increase in conductance, but not the KAuBr₄ doped (8,0) conductor. The ion dopants had no effect on the SWNT conductors.

Using the three effective dopants, a nanowire model was used to compare the doped conductor results to the experimental work on KAuBr₄ doped CNT [7]. Results were positive in indicating the improvement of the computational models over conventional copper, although more work on studying SWNT junctions would improve the nanowire model prediction significantly.

In general, the results in this work show the potential of SWNT wires doped with KAuBr₄, K, and AuBr₄ for conductive wires (especially K in mass specific applications) and can assist future experimental efforts in the investigation of doped SWNT conductive wires. In the near future, we integrate the results shown here with SWNT junction models into a nanowire model to describe the performance of the doped SWNTs, as compared to an experimental reference [7] and to copper. The work will provide a practical connection between the computational results and experimental works, which highlights the potential of the KAuBr₄ doped CNTs.

Acknowledgements

This work was supported by the Office of Naval Research grant (Grant No. N00014-15-1-2693). Computer time support provided by the Texas Advanced Computing Center at the University of Texas at Austin and the Department of Defence High Performance Computing Modernization Program.

References

- [1] Iijima, S., 1991, "Helical Microtubules of Graphitic Carbon," *Nature*, **354**, pp. 56-58.
- [2] Puchades, I., Lawlor, C. C., Schauerma, C. M., Bucossi, A. R., Rossi, J. E., Cox, N. D., and Landi, B. J., 2015, "Mechanism of Chemical Doping in Electronic-Type-Separated Single Wall Carbon Nanotubes Towards High Electrical Conductivity," *Journal of Materials Chemistry C*, **3**(39), p. 10256.

- [3] Zhao, Y., Wei, J., Vajtai, R., Ajayan, P. M., and Barrera, E. V., 2011, "Iodine Doped Carbon Nanotube Cables Exceeding Specific Electrical Conductivity of Metals," *Scientific Reports*, **1**, p. 83.
- [4] Lee, P., Ham, J., Lee, J., Hong, S., Han, S., Suh, Y. D., Lee, S. E., Yeo, J., Lee, S. S., Lee, D., and Ko, S. H., 2014, "Highly Stretchable or Transparent Conductor Fabrication by a Hierarchical Multiscale Hybrid Nanocomposite," *Advanced Functional Materials*, **24**(36), pp. 5671-5678.
- [5] Janas, D., Milowska, K. Z., Bristowe, P. D., and Koziol, K. K. K., 2017, "Improving the Electrical Properties of Carbon Nanotubes with Interhalogen Compounds," *Nanoscale*, **9**(9), pp. 3212-3221.
- [6] Alvarenga, J., Jarosz, P. R., Schauerman, C. M., Moses, B. T., Landi, B. J., Cress, C. D., and Raffaele, R. P., 2010, "High Conductivity Carbon Nanotube Wires from Radial Densification and Ionic Doping," *Applied Physics Letters*, **97**(18), p. 182106.
- [7] Cress, C. D., Ganter, M. J., Schauerman, C. M., Soule, K., Rossi, J. E., Lawlor, C. C., Puchades, I., Ubnoske, S. M., Bucossi, A. R., and Landi, B. J., 2017, "Carbon Nanotube Wires with Continuous Current Rating Exceeding 20 Amperes," *Journal of Applied Physics*, **122**(2), p. 025101.
- [8] Lee, R. S., Kim, H. J., Fischer, J. E., Thess, A., and Smalley, R. E., 1997, "Conductivity Enhancement in Single-Walled Carbon Nanotube Bundles Doped with K and Br," *Nature*, **388**(6639), pp. 255-257.
- [9] Kim, K. K., Bae, J. J., Park, H. K., Kim, S. M., Geng, H., Park, K. A., Shin, H., Yoon, S., Benayad, A., Choi, J., and Lee, Y. H., 2008, "Fermi Level Engineering of Single-Walled Carbon Nanotubes by AuCl₃ Doping," *Journal of the American Chemical Society* **130**(38), pp. 12757-12761.
- [10] Salzer, A., 1999, "Nomenclature of Organometallic Compounds of the Transition Elements (IUPAC Recommendations 1999)," *Pure and Applied Chemistry*, **71**(8), pp. 1557-1585.
- [11] Li, X., Liu, J., Kong, F., Liu, X., Xu, J., and Chen, H., 2012, "Potassium-Doped Graphene for Simultaneous Determination of Nitrite and Sulfite in Polluted Water," *Electrochemistry Communications*, **20**, pp. 109-112.
- [12] Miyake, T., and Saito, S., 2002, "Electronic Structure of Potassium-Doped Carbon Nanotubes," *Physical Review B*, **65**(16), p. 165419.
- [13] Kim, S. M., Kim, K. K., Jo, Y. W., Park, M. H., Chae, S. J., Duong, D. L., Yang, C. W., Kong, J., and Lee, Y. H., 2011, "Role of Anions in the AuCl₃-Doping of Carbon Nanotubes," *ACS Nano*, **5**(2), pp. 1236-1242.
- [14] Murat, A., Rungger, I., Jin, C., Sanvito, S., and Schwingenhlögl, U., 2014, "Origin of the p-Type Character of AuCl₃ Functionalized Carbon Nanotubes," *Journal of Physical Chemistry C*, **118**(6), pp. 3319-3323.
- [15] Ketolainen, T., Havu, V., and Puska, M. J., 2017, "Conductivity of AuCl₄-Functionalized Carbon Nanotube Networks," *The Journal of Physical Chemistry C*, **121**(8), pp. 4627-4634.
- [16] Li, Y., and Fahrenthold, E., 2018, "Ab Initio Study of Iodine-Doped Carbon Nanotube Conductors," *Journal of Engineering Materials and Technology*, **140**(2), p. 021008.
- [17] Soler, J. M., Artacho, E., Gale, J. D., García, A., Junquera, J., Ordejón, P., and Sánchez-Portal, D., 2002, "The SIESTA Method for Ab Initio Order-N Materials Simulation," *Journal of Physics: Condensed Matter*, **14**(11), pp. 2745-2780.
- [18] Perdew, J. P., Burke, K., and Ernzerhof, M., 1996, "Generalized Gradient Approximation Made Simple," *Physical Review Letters*, **77**(18), pp. 3865-3868.
- [19] Artacho, E., Sánchez-Portal, D., J., Ordejón, P., García, A., and Soler, J. M., 1999, "Linear-Scaling Ab-Initio Calculations for Large and Complex Systems," *Physica Status Solidi (B)*, **215**(1), pp. 809-817.
- [20] Bonardi, P., Achilli, S., Tantardini, G. F., and Martinazzo, R., 2015, "Electron Transport in Carbon Wires in Contact with Ag Electrodes: A Detailed First Principles Investigation," *Physical Chemistry Chemical Physics*, **17**(28), p. 18413.
- [21] Matsuda, Y., Tahir-Kheli, J., and Goddard, W. A., III., 2010, "Definitive Band Gaps for Single-Wall Carbon Nanotubes," *Journal of Physical Chemistry Letters*, **1**(19), pp. 2946-2950.
- [22] The Siesta Group, 2016, "USER'S GUIDE: SIESTA 4.0," Retrieved from <https://departments.icmab.es/leem/siesta/Documentation/Manuals/siesta-4.0.pdf>
- [23] Band, Y. B., and Avishai, Y., 2013, *Quantum Mechanics with Applications to Nanotechnology and Information Science*, Academic Press, Amsterdam, The Netherlands, Chap. 13, p. 757.
- [24] Brandbyge, M., Mozos, J., Ordejón, P., Taylor, J., and Stokbro, K., 2002, "Density-Functional Method for Nonequilibrium Electron Transport," *Physical Review B*, **65**(16), p. 165401.
- [25] Meija, J., Coplen, T., Berglund, M., Brand, W. A., De Bièvre, P., Gröning, M., Holden, N. E., Irrgeher, J., Loss, R. D., Walczyk, T., and Prohaska, T., 2016, "Atomic Weights of the Elements 2013 (IUPAC Technical Report)," *Pure and Applied Chemistry*, **88**(3), pp. 265-291.
- [26] Sun, G., K irti, J., Kertesz, M., and Baughman, R. H., 2003, "Variations of the Geometries and Band Gaps of Single-Walled Carbon Nanotubes and the Effect of Charge Injection," *Journal of Physical Chemistry*, **107**(29), pp. 6924-6931.
- [27] Rabiee Golgir, H., Faez, R., Pazoki, M., Karamitaheri, H., and Sarvari, R., 2011, "Investigation of Quantum Conductance in Semiconductor Single-Wall Carbon Nanotubes: Effect of Strain and Impurity," *Journal of Applied Physics*, **110**(6), p. 064320.
- [28] Thomsen, C., Reich, S., and Maultzsch, J., 2004, *Carbon Nanotubes: Basic Concepts and Physical Properties*, Wiley-VCH Verlag GmbH, Weinheim, Germany, Chap. 5, p. 86.

- [29] Cambré, S., Wenseleers, W., Goovaerts, E., and Resasco, D. E., 2010, "Determination of the Metallic/Semiconducting Ratio in Bulk Single-Wall Carbon Nanotube Samples by Cobalt Porphyrin Probe Electron Paramagnetic Resonance Spectroscopy," *ACS Nano*, **4**(11), pp. 6717-6724.
- [30] Mann, D., Javey, A., Kong, J., Wang, Q., and Dai, H., 2003, "Ballistic Transport in Metallic Nanotubes with Reliable Pd Ohmic Contacts," *Nano Letters*, **3**(11), pp. 1541-1544.
- [31] Matula, R. A., 1979, "Electrical Resistivity of Copper, Gold, Palladium, and Silver," *Journal of Physical and Chemical Reference Data*, **8**(4), p. 1147.

Table 1. Atomic masses of atoms used in models

Element	K	Au	Br	C
Mass (amu)	39.098	196.967	79.904	12.012

Table 2. Dopant standoff (from SWNT surface), mass per unit length, and dopant mass fraction for the doped conductors

Dopant	SWNT Chirality	Concentration (number per unit cell)	Dopant Standoff $l_{dopant-SWNT}^*$ (Å)	Mass per Unit Length \hat{m}_c (amu Å ⁻¹)	Dopant Mass Fraction (%)
KAuBr ₄	(8,0)	0.50	3.375 (Au)	155.3	0.420
		1.00	3.313 (Au)	220.5	0.591
	(5,5)	0.33	3.364 (Au)	172.9	0.435
		0.67	3.362 (Au)	248.1	0.607
K	(8,0)	0.50	2.352	94.7	0.048
		1.00	2.492	99.3	0.092
	(5,5)	0.50	2.618	105.6	0.075
		1.00	2.549	113.5	0.140
AuBr ₄	(8,0)	0.50	3.382 (Au)	150.8	0.402
		1.00	3.186 (Au)	211.3	0.573
	(5,5)	0.33	3.507 (Au)	167.6	0.418
		0.67	3.375 (Au)	237.5	0.589
K ⁺	(8,0)	0.50	2.503	94.8	0.048
		1.00	2.440	99.3	0.092
	(5,5)	0.50	2.546	105.5	0.075
		1.00	2.936	113.5	0.140
AuBr ₄ ⁻	(8,0)	0.50	3.163 (Au)	150.8	0.402
		1.00	3.296 (Au)	211.3	0.573
	(5,5)	0.33	3.377 (Au)	167.6	0.418
		0.67	3.506 (Au)	237.5	0.589

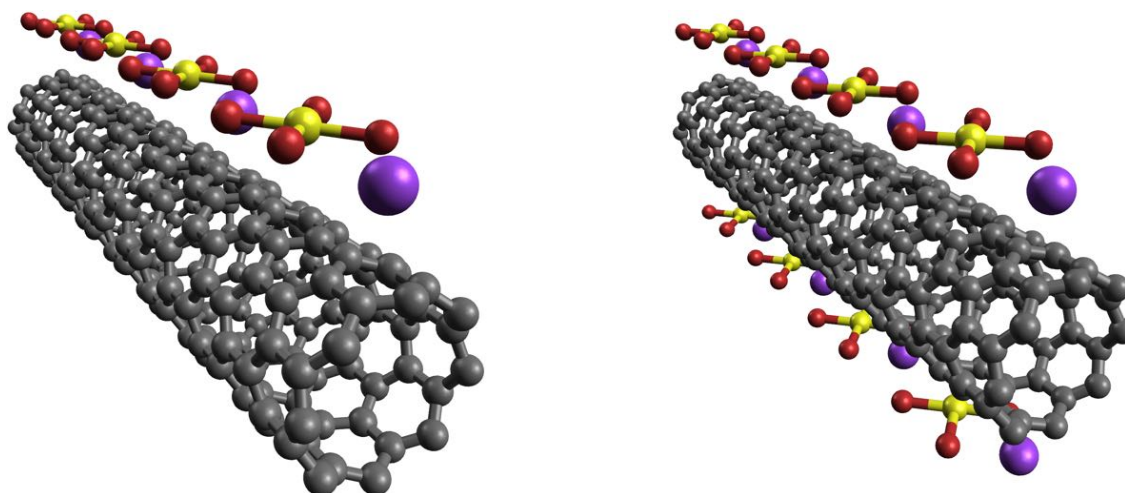


Fig. 1. KAuBr₄ doped SWNTs: (8,0) SWNT with 0.500 dopant molecules per unit cell (left), and 1.000 dopant molecules per unit cell (right)

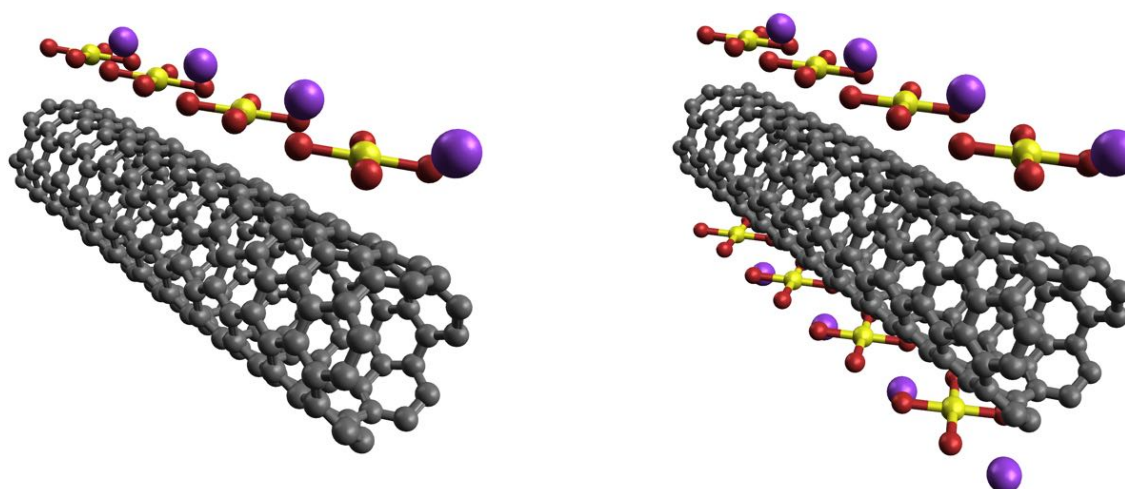


Fig. 2. KAuBr₄ doped SWNTs: (5,5) SWNT with 0.333 dopant molecules per unit cell (left), and 0.667 dopant molecules per unit cell (right)

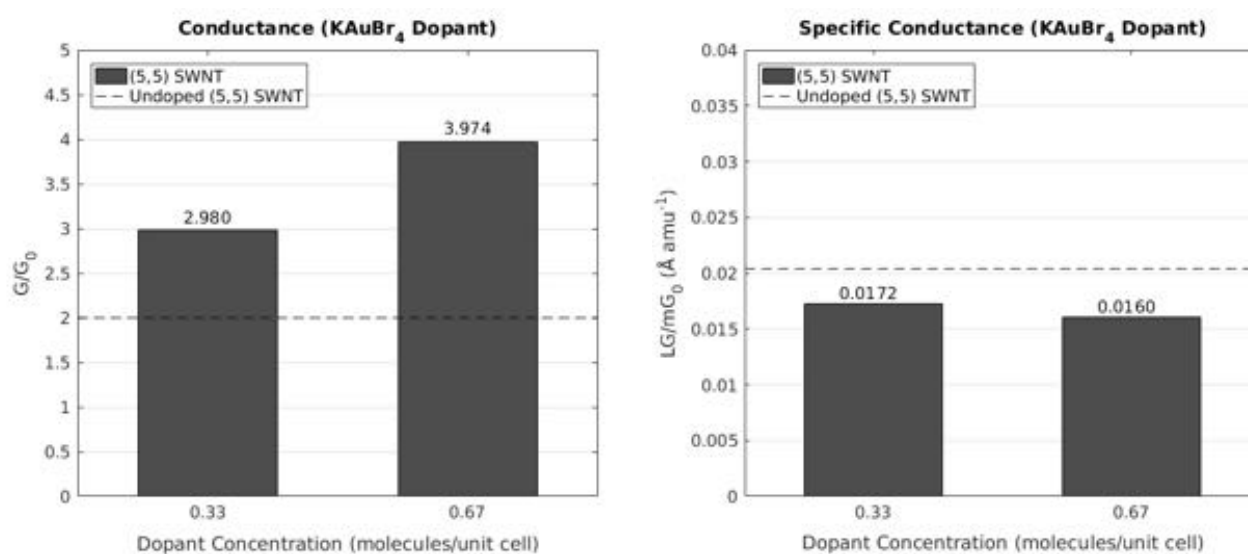


Fig. 3. Performance of the KAuBr₄ doped SWNTs (conductance, left, and specific conductance, right), with the dashed lines representing an undoped (5,5) SWNT (note that the (8,0) SWNT was not affected by KAuBr₄ doping)

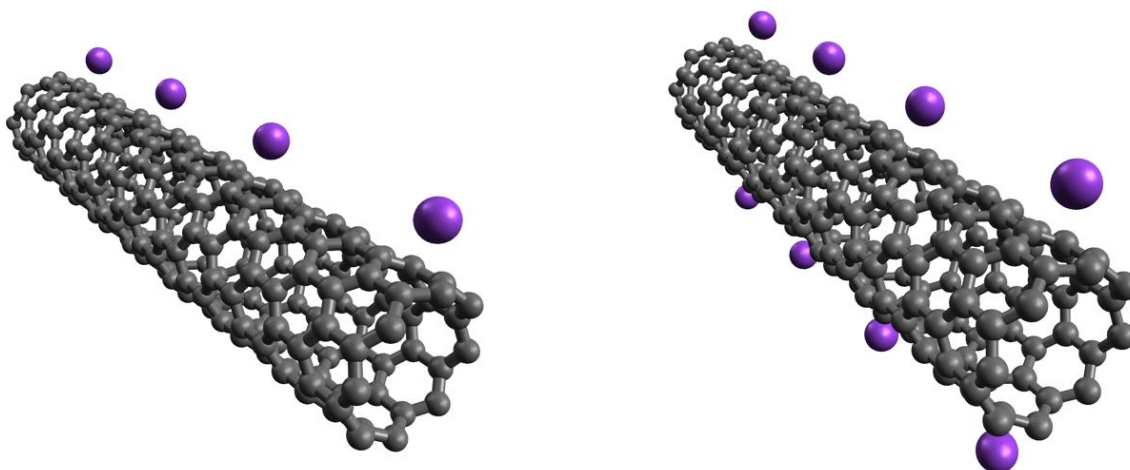


Fig. 4. K doped SWNTs: (8,0) SWNT with 0.500 dopant atoms per unit cell (left), and 1.000 dopant atoms per unit cell (right)

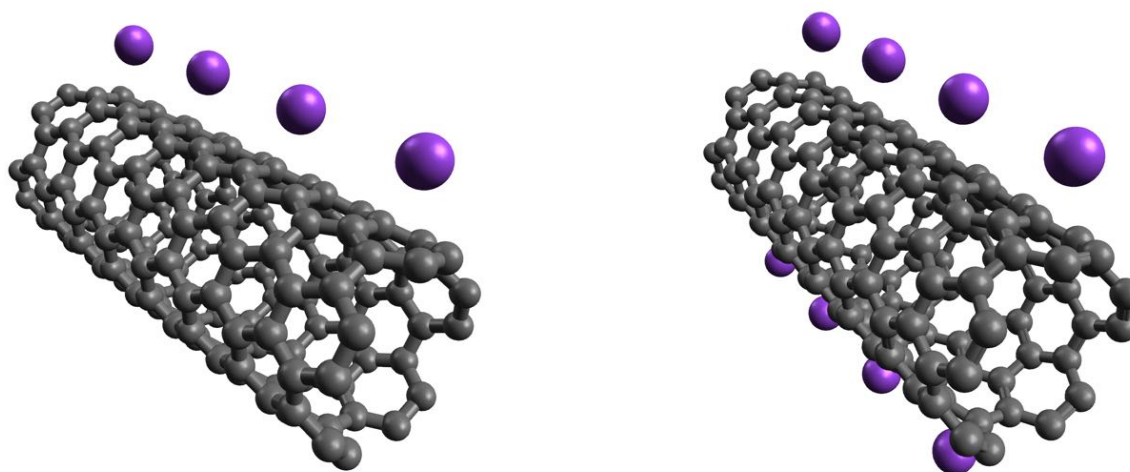


Fig. 5. K doped SWNTs: (5,5) SWNT with 0.500 dopant atoms per unit cell (left), and 1.000 dopant atoms per unit cell (right)

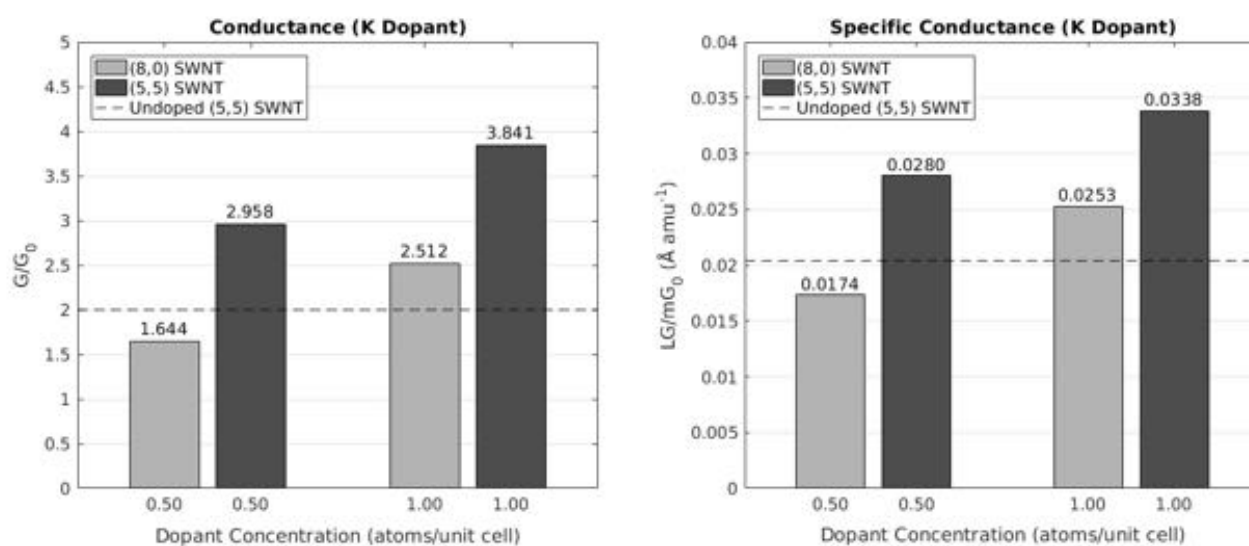


Fig. 6. Performance of the K doped SWNTs (conductance, left, and specific conductance, right), with the dashed lines representing an undoped (5,5) SWNT

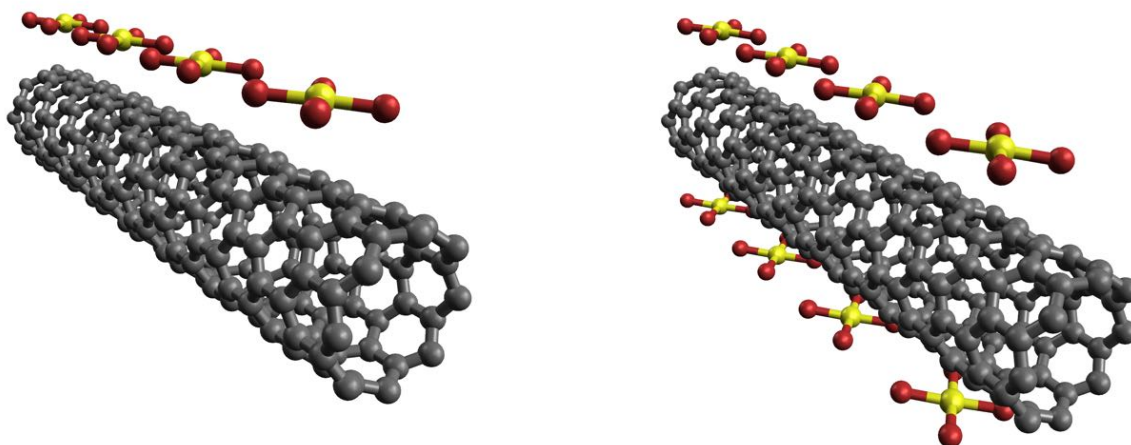


Fig. 7. AuBr_4 doped SWNTs: (8,0) SWNT with 0.500 dopant fragments per unit cell (left), and 1.000 dopant fragments per unit cell (right)

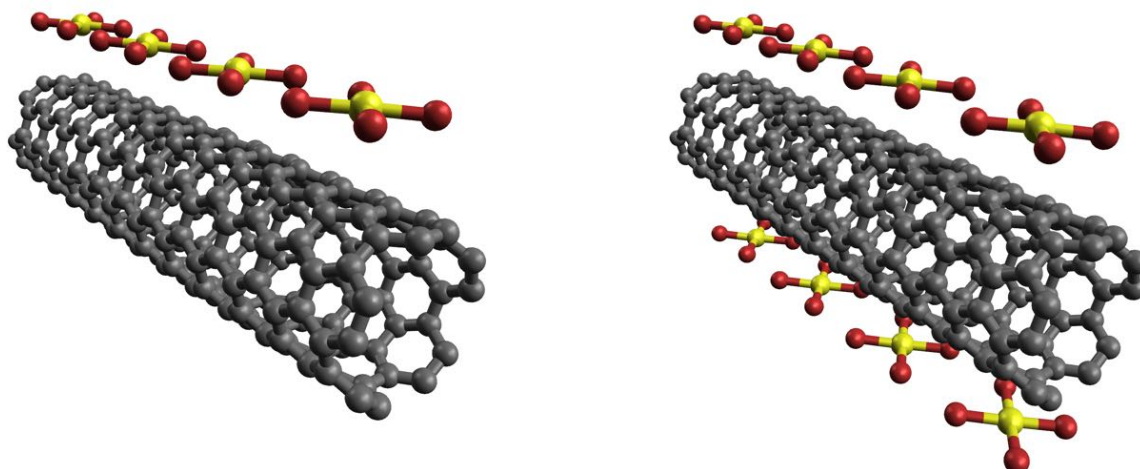


Fig. 8. AuBr_4 doped SWNTs: (5,5) SWNT with 0.333 dopant fragments per unit cell (left), and 0.667 dopant fragments per unit cell (right)

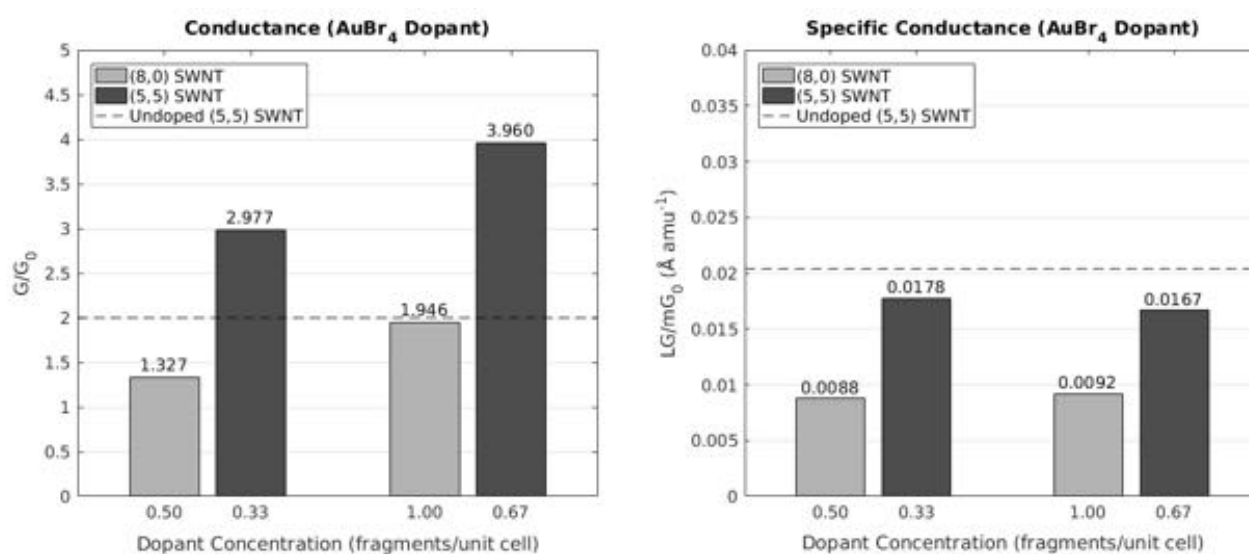


Fig. 9. Performance of the AuBr_4 doped SWNTs (conductance, left, and specific conductance, right), with the dashed lines representing an undoped (5,5) SWNT

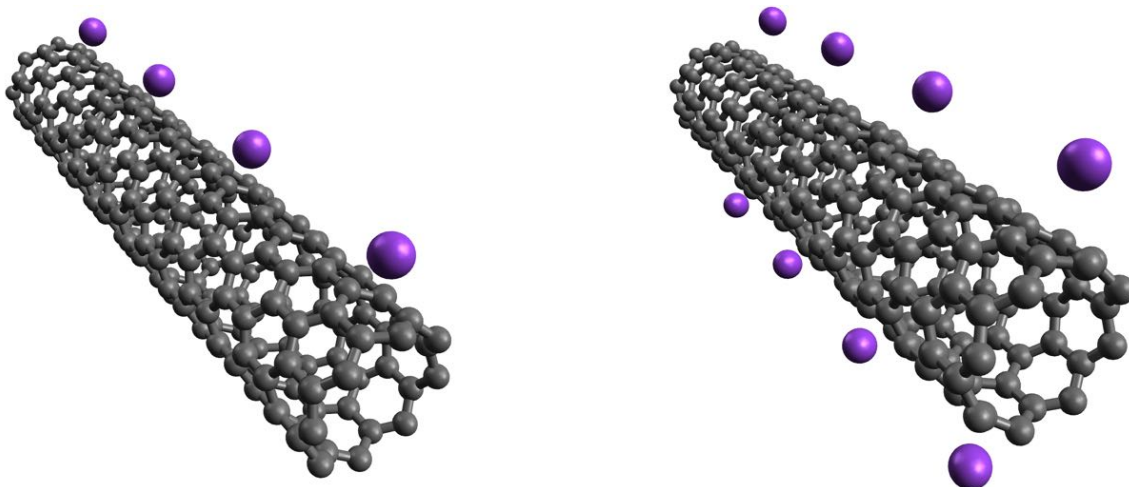


Fig. 10. K doped SWNTs: (8,0) SWNT with 0.500 dopant ions per unit cell (left), and 1.000 dopant ions per unit cell (right)

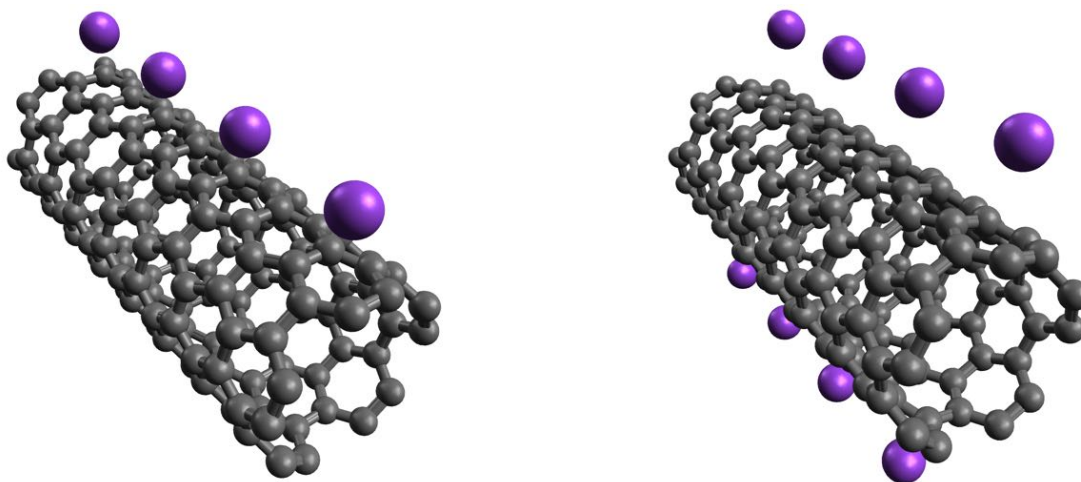


Fig. 11. K doped SWNTs: (5,5) SWNT with 0.500 dopant ions per unit cell (left), and 1.000 dopant ions per unit cell (right)

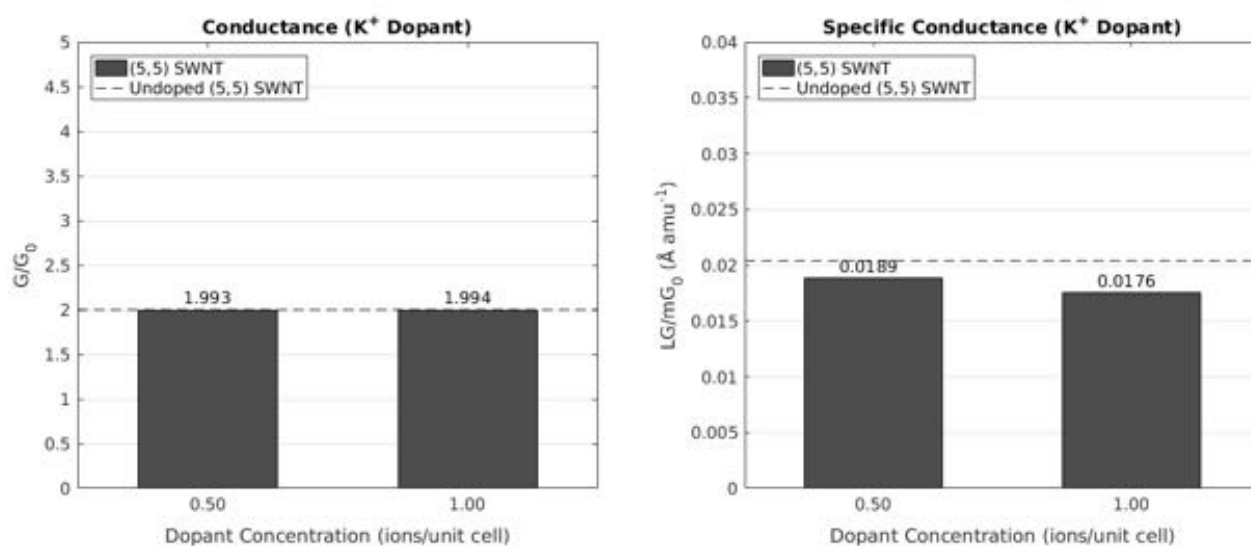


Fig. 12. Performance of the K^+ doped SWNTs (conductance, left, and specific conductance, right), with the dashed lines representing an undoped (5,5) SWNT

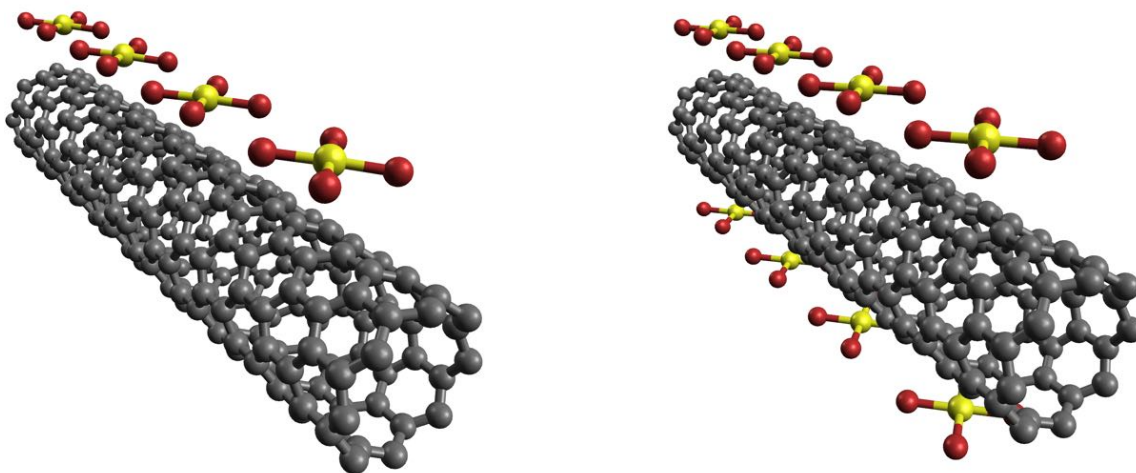


Fig. 13. AuBr_4^- doped SWNTs: (8,0) SWNT with 0.500 dopant ions per unit cell (left), and 1.000 dopant ions per unit cell (right)

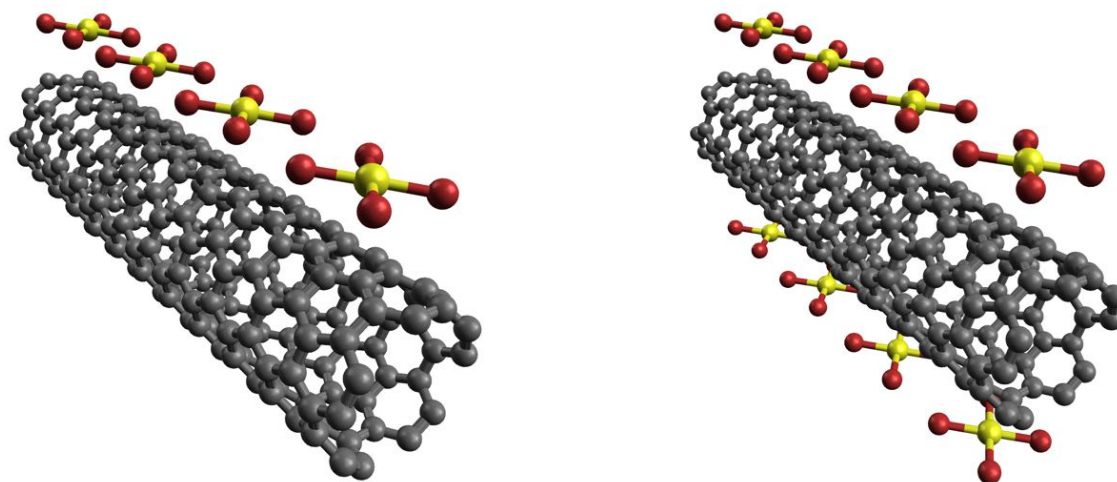


Fig. 14. AuBr_4^- doped SWNTs: (5,5) SWNT with 0.333 dopant ions per unit cell (left), and 0.667 dopant ions per unit cell (right)

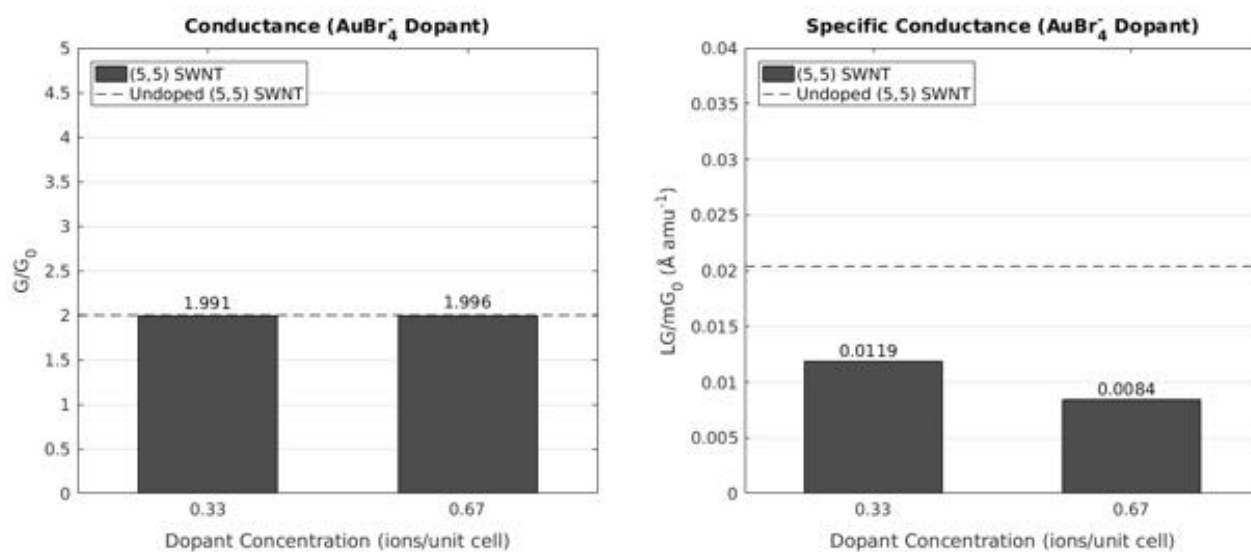


Fig. 15. Performance of the AuBr_4^- doped SWNTs (conductance, left, and specific conductance, right), with the dashed lines representing an undoped (5,5) SWNT

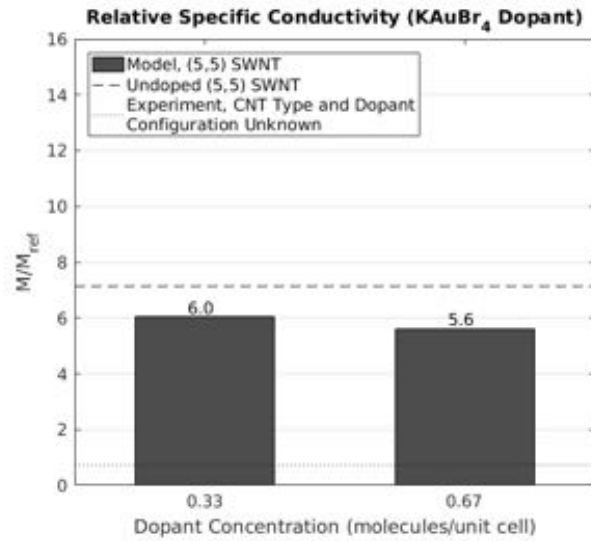


Fig. 16. The relative specific conductivity of the KAuBr₄ doped nanowire, as compared to the undoped nanowire and the experimental reference [7]

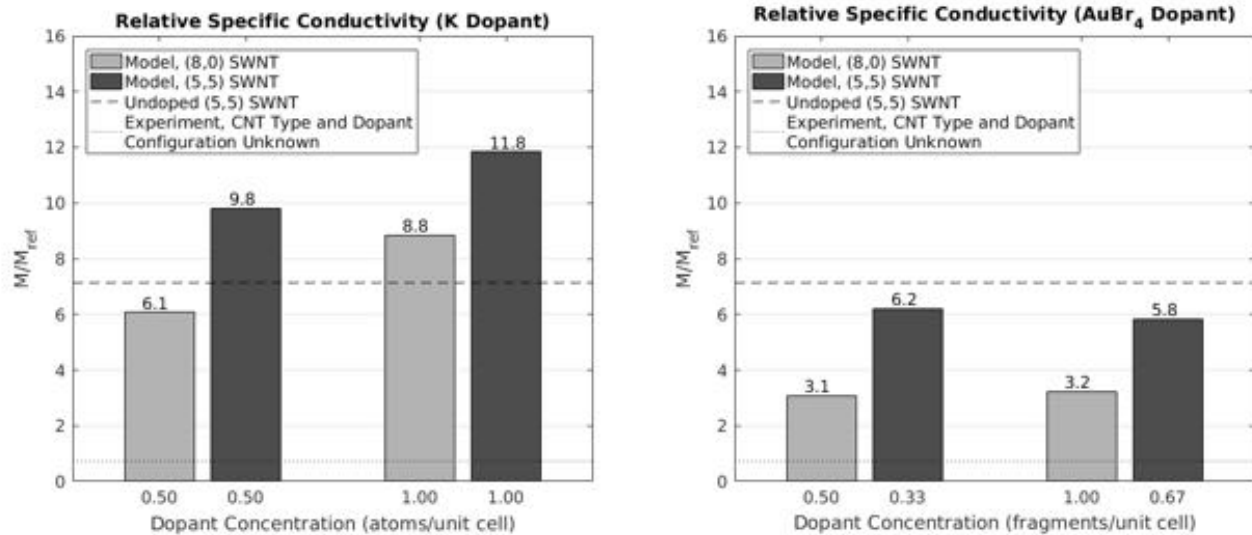


Fig. 17. The relative specific conductivity of the doped nanowires, for the K dopant (left) and the AuBr₄ dopant (right), as compared to the undoped nanowire and the experimental reference [7]

Molecular Doping of Carbon Nanotube Wiring - Part II: Junctions

Khai Yi Chin

Department of Mechanical Engineering
University of Texas
Austin, Texas 78705
Email: khaiyichin@utexas.edu

Eric Fahrenthold

Department of Mechanical Engineering
University of Texas
Austin, Texas 78705
Email: epfahren@austin.utexas.edu

ABSTRACT

Carbon nanotubes (CNTs) have been steadily gaining traction as a potential material for electrical wiring. As such, the characterization of the electrical properties of CNTs are vital to fulfill the objective of producing CNT-based wires. In this paper, single-walled nanotubes (SWNTs) are studied in undoped and doped junctions to understand the reaction of the SWNTs to several factors, including nanotube separation distance and packing, rotational misalignment, overlap distance, as well as chemical doping and doping configuration. Here, the dopants of interest are the K atom and AuBr₄ fragment. Additionally, a nanowire model is presented to provide a means to compare the computational results to experiment.

The undoped SWNT junctions were very sensitive to the change in nanotube separation distance (and packing) as well as overlap distance. Besides, rotational misalignments of 12° and 18° drastically reduced the junction conductance. As for the doped junctions, the conductance of K doped junctions was similar, regardless of doping configuration, while the conductance for the AuBr₄ doped junction was heavily reliant on the doping configuration. The AuBr₄ doping fragment showed a unique characteristic: it eliminated the dependence of the junction conductance on nanotube overlap. A nanowire model was developed and used as a metric for comparison with experimental studies of KAuBr₄ doped CNTs. The nanowire model provided a reasonable comparison of the computational results with previous experimental work. Overall, results presented in this paper show the promise of doped CNTs as potential candidates for the replacement of conventional copper conductors.

1 Introduction

Carbon nanotube (CNT) have been steadily gaining traction as a potential material for electrical wiring. Notably, CNTs offer advantage over conventional electrical conductors made of copper, since they are much lighter and flexible [1]; such benefits are attractive to industries that rely on electrical conductors for mass specific applications. In order to implement CNTs in wiring applications, past research efforts have focused on studying the factors affecting wiring conductance, including nanotube separation distance [2] and packing (radial densification of CNT-based wires) [3], overlap distance [4,5], chemical doping [3,6–13], as well as doping configuration [13]. These effects are all considered in this paper. In addition to those, the effect of rotational misalignment in junctions, which has not been investigated before, was studied.

The characterization of the junction conductance with respect to the nanotube separation distances was motivated by the efforts of Srivastava et al. [2], who found a dependence of conductance on separation distances of graphene nanoribbons (defined as contact distances in the aforementioned work). Here, in order to understand the effects of densification in experimental works [3, 14], the nanotube separation distance in undoped SWNT junctions was tested as a variable, which determines the packing arrangement. Besides, this paper presents effects of a change in packing arrangement of a K doped junction. In this work, the packing arrangement is dictated by the model's computational unit cell (finite volume of a wire),

which has the dimensions $x_{junc} \times y_{junc} \times z_{junc}$, and the packing density is defined as the number of SWNTs divided by the cross section of the wire: $2/x_{junc}y_{junc}$.

Additionally, this paper presents the effects of overlap distances on both the undoped and the doped SWNT junctions. Previous works detailed the behavior of junction conductance with respect to varying overlap distances: both González et al. [4] and Tripathy et al. [5] noted an oscillatory behavior in conductance as a function of overlap distances in graphene and SWNT junctions respectively. In this work, the overlap distance effects were studied at various nanotube separation distances for the undoped junctions described previously, presenting new results on the combined effects of both nanotube separation and overlap distances. Furthermore, overlap distance effects on the junction conductance documented here for the K and AuBr₄ doped junctions are novel; no junction works for the two mentioned dopants were found.

While much of the past research focused on orientation and configuration in junctions, such as separation distances (in graphene nanoribbon-graphene interlayer distance) [2] and overlap [5], none looked at the rotational misalignment between SWNTs in junctions. This work investigated the effects of said rotational misalignment on undoped SWNT junctions, since the role of interface alignment is well documented in graphene junctions [4, 15–17].

In terms of chemical doping, there have been many experimental efforts made to enhance the electronic properties of CNTs with various dopants. Janas et al. [6] looked into doping CNTs with interhalogen compounds (I₂, ICl, IBr) that improved conductance. Potassium tetrabromoaurate (KAuBr₄) doped CNTs were superior than the undoped CNTs in terms of conductivity [3, 7]. Meanwhile, single-walled nanotubes (SWNT) doped with potassium (K) and bromine (Br) saw a decrease in resistivity [8], and Kim et al. [9] observed a decrease in SWNT sheet resistance through AuCl₃ doping. Motivated by the experimental efforts in [3, 7], computational results on the KAuBr₄ dopant on SWNT conductors were presented in a previous work [18]. In that work, computational models of SWNT conductors doped with K, AuBr₄, K⁺, and AuBr₄⁻ were investigated in addition to the KAuBr₄ dopant, since the doping solution used in the experiment was an aqueous KAuBr₄ solution [3, 7], which introduced possibilities of having dopants from the disassociated parts of the KAuBr₄ molecule. From those results, the K and AuBr₄ dopants were picked as candidates for doping the SWNT junction models in this paper. Notably, the K atom and the AuBr₄ fragments are reasonable disassociation states for the KAuBr₄ molecule. In addition, both the K and AuBr₄ dopants are symmetric: the K atom being a sole atom, and the AuBr₄ fragment being square planar. This eliminated dopant orientation as a degree of freedom that the KAuBr₄ would otherwise introduce. K⁺ and AuBr₄⁻ were considered as well, but due to their lack of effect on the SWNT conductors [18], only their charge neutral counterparts are discussed here.

In relation to past computational works, Li and Marzari [10] looked at (5,5) nanotube junctions and showed the potential of transition metals as a ‘linker’ atom in the junction interface, to improve the electrical conductance of the junctions. Their junction models only considered transition metals as dopants, and only had about a one half unit cell of junction overlap. Saito [11] studied the computational model of K doped CNTs as a candidate for superconductors, and observed an upwards shift in the Fermi energy, a sign of n-doping. In this paper, the K atoms were used to dope junctions, not conductors as shown in Saito’s work (which means that electronic transport from one end to another is more likely to be due to intertube travel as compared to arrays of continuous SWNT conductors). Furthermore, junctions presented in this work considered multiple overlap distances and not continuous, as shown in Fig. 1 (left). Meanwhile, the closest computational study to AuBr₄ doped junctions were AuCl₄ doped junctions [12], but the models presented in that work had the junction tube axes orthogonal to each other, which differed from the junction models presented in this paper. In that work, they utilized (10,0) semiconducting SWNT junctions, and showed an increase of conductance from zero to an ideal metallic SWNT conductance. In this paper, the AuBr₄ doped junctions presented are of metallic SWNTs.

Moreover, inspired by the detailed look at dopant distribution using iodine doped SWNTs [13], two doping configurations were tested in this research: the external doping and interstitial doping configuration. The external doping configuration was adopted from a previous work on doped SWNT conductors [18], whereby the dopants are positioned above the SWNT conductors, whereas the interstitial doping configuration was motivated by the iodine doped junctions from a previous work [13]. There has not been any junction models in the literature concerning the K atom and AuBr₄ fragment, thus this paper will contribute to the scientific body in the knowledge of doped SWNT junctions, and consequently, doped nanowires.

In this research, the (5,5) SWNT was chosen as the SWNT candidate for the junction models because, as compared to the (8,0) SWNT, the metallic SWNT better allowed observation of the doping effects. If the dopant was detrimental to the junction conductance, there would be a decrease in conductance (from $2G_0$), and if the dopant was beneficial, there would be an increase in conductance; in the case of the (8,0) SWNT, only the positive effects can be seen. Computational studies of metallic junctions are scarce, especially for the K atom and AuBr₄ fragment. The closest reference found investigated junctions comprising of two semiconducting SWNTs [12]. This work on the metallic SWNT junctions in this paper will fill in a void pertaining to the conductance of doped metallic junctions, complementing the past research efforts on semiconducting SWNT junctions.

In this paper, Section 2 describes the methodology in modeling the SWNT junctions. Section 3 presents the results on the SWNT junction models, and Section 4 defines a nanowire model to compare the computational model results. Finally, the conclusions are drawn in Section 5.

2 Methodology

The investigation of the SWNT models was done using the Spanish Initiative for Electronic Simulations with Thousands of Atoms (SIESTA) version 4.0 program. It is a density functional theory (DFT) based computational method that uses a linear combination of atomic orbitals (LCAO) as its basis set [19]; the atomic orbitals used in this paper were double ζ polarized. The PBE exchange correlation functionals [20] and pseudopotentials used were obtained through the Generalized Gradient Approximation (GGA). The orbital energy shift was set to $\Delta E_{PAO} = 150$ meV, and the models were relaxed to an atomic force threshold of at most 0.04 eV \AA^{-1} .

A k -grid mesh of $1 \times 1 \times 1$ was used for relaxation, and a k -grid mesh of $1 \times 1 \times 4$ was used for the transport calculations, both with a mesh cutoff energy at 300 Ry [21]. Computational unit cells with periodic boundary conditions were used for both the structural relaxation and transport calculations. The computation began with a structural relaxation of the two aligned SWNT conductors in an isolated environment (with SWNTs to the computational unit cell walls in the x - and y -direction 20 \AA apart [18]), to obtain an equilibrium configuration for the model. Then, alternate ends of the two conductors were discarded to form a junction. The model was then moved to a computational unit cell with dimensions $x_{junc} \times y_{junc} \times z_{junc}$ for transport calculations (which has the packing density $2/x_{junc}y_{junc}$), shown in Figs. 2 and 3, explained further in the next section. The packing density (and thus the computational unit cell size) is dependent on the nanotube separation distance, dopant standoff, dopant separation distance and SWNT diameter.

The transport calculations were performed on the models using the TranSIESTA module within the SIESTA program. TranSIESTA operates by computing the charge density matrix with Green's functions [22], which gives the Landauer-Büttiker formula for conductance [23]. Since the transport calculations were performed at zero temperature, the conductance formula becomes [24]:

$$G = T(E)G_0, \quad G_0 = \frac{2e^2}{h} = 7.748 \times 10^{-5} \text{ S} \quad (1)$$

where $T(E)$ is the transmission amplitude at energy E , G_0 is the conductance quantum, e is the elementary charge, and h is Planck's constant.

The junction models consist of three parts: two end electrodes (one at each end) and the scattering region. The two end electrodes were acquired via an alternate-end-removal process from the two SWNT conductors described earlier, depending on the overlap distance desired; the remaining (and alternate) ends were then used as electrodes. The electrodes are three to four unit cells long (depending on dopant species, as elaborated further in the following section), identical to the scattering region (of the same chemical species and dopants), and semi-infinite; the side of an electrode not attached to the scattering region extends infinitely via its periodic images.

3 Junction Models

This section presents the results of the research on the SWNT junction models, as a reaction to SWNT configurations and doping effects, in the interest of improving the design of CNT-based wiring. Since any practical nanowire consists of a large number of noncontinuous CNTs, it is only rational to consider the intertube movement of electrons (in addition to the intratube conductance studied in [18]), in order to better understand the conductivity of a macro-scale wire. To do this, SWNT junctions were simulated. The (5,5) SWNT conductor was used in all junction models due to the convenience of observing conductance effects by the dopants.

For a CNT-based macro-scale wire to be fabricated, it needs to contain a huge bundle of nanotubes packed together. Since prior work by Srivastava et al. [2] found an influence on junction conductance by the separation distance between a graphene nanoribbon and its graphene electrodes, the transport calculations performed in this work addressed that by investigating junction models with different nanotube separation distances and packing arrangements, dictated by the size of the computational unit cell used. Beside the nanotube separation distances and packing effects, the influence of overlap distances and rotational configuration on the conductance of the (5,5) SWNT junctions were studied; the effect of overlap distances has been well documented in both graphene [4] and SWNT junctions (labeled as contacts in their work) [25], while there were no studies on the effects of rotational configuration of SWNTs found.

In this research, the K atom and AuBr₄ were chosen as candidates to dope the SWNT junctions. As mentioned in the Introduction, the choice of the two dopants was a logical progression from the results obtained in a previous work, where the K doped and AuBr₄ doped SWNT conductors displayed great improvements to the conductance [18]. The KAuBr₄ molecule showed excellent results too, but due to the asymmetry of the KAuBr₄ molecule, only the K atom and AuBr₄ fragment were considered here. The KAuBr₄ molecule is considered as a future effort in modeling doped SWNT junctions. Other than dopant types, two doping configurations were also tested: the external doping and the interstitial doping configurations. The difference in doping configurations attempts to explore the effects of dopant distribution on junction conductance, as studied in [13].

3.1 Geometry of Undoped SWNT Junctions

The geometries of the different undoped junctions studied are described here, including the packing arrangement tested to investigate the effects of varying nanotube separation distances; the rotationally misaligned geometry is also explained in this subsection.

Firstly, two aligned and isolated SWNT conductors were relaxed, from which the equilibrium nanotube separation distance between the two conductors was obtained, defined as $l_{SWNT-SWNT}^*$. The ends of the undoped conductors were then removed in the model, as follows: alternate ends of the two relaxed conductors were removed (equal lengths) depending on the overlap distances desired.

For the transport calculations of the undoped junctions, the intention was to have the SWNT conductors in the model and in the periodic images be separated by the nanotube separation distance, $l_{SWNT-SWNT}^*$. Therefore, the SWNT junction was packed into a computational unit cell of dimensions $x_{junc} \times y_{junc} \times z_{junc}$, defined as:

$$x_{junc} = l_{SWNT-SWNT}^* + d_{SWNT} \quad (2)$$

$$y_{junc} = 2l_{SWNT-SWNT}^* + 2d_{SWNT} \quad (3)$$

where d_{SWNT} is the diameter of the SWNT conductor, with z_{junc} as the length of the model. The model of two aligned, undoped (5,5) SWNTs, each 15 unit cells long, was relaxed to a nanotube separation distance of $l_{SWNT-SWNT}^* = 3.36 \text{ \AA}$. Figure 1 shows the undoped (5,5) SWNT junction with a five unit cell overlap. Figure 2 shows the computational unit cell used for the undoped junction model in the transport calculations, and Table 1 lists the dimensions.

Apart from allowing the two aligned SWNTs to relax freely in the y-direction, which resulted in a nanotube separation distance of $l_{SWNT-SWNT}^* = 3.36 \text{ \AA}$, the effect which different packing arrangements have on the conductance of the junction was determined. This was done to simulate conditions in a recent work, whereby the researchers radially densified rolled CNT sheets before doping them in KAuBr₄ solution [3]. To do this, the nanotube separation distance was initialized to $l_{SWNT-SWNT} = 1.50, 2.00, 2.50, 3.00, 3.50$, and 4.00 \AA for structural relaxation (the asterisk has been removed to indicate that the distances are no longer for isolated nanotubes, but for packed nanotubes). The packing arrangements were still obtained using the rules shown in Eqns. (2) and (3), except that now $l_{SWNT-SWNT}^*$ is replaced by $l_{SWNT-SWNT}$. Table 1 shows all dimensions for the computational unit cells used for the model junctions at seven different nanotube separation distances.

Furthermore, the examination of SWNT configuration was extended to study the effects of rotational misalignment. While there have been previous efforts to study the effects on junction conductance of overlap distances and tube axis alignment [5], there has not been any computational research on the rotational misalignment of nanotubes in junctions. Thus the effects of rotational misalignment between the SWNT conductors in the junctions was investigated here. Figure 4 shows three rotational configurations of the two conductors in the junction model: (a) is the model used for all junction calculations: the carbon atoms of the two SWNT conductor surfaces facing each other align perfectly. The upper conductor may be rotated along its tube axis, as shown in (b) for a rotation of 12° , and (c) for a rotation of 18° . The unrolled view of the misaligned models is shown in Fig. 5. The choice of 12° and 18° rotations was driven by the honeycomb lattice of the SWNTs: a 12° rotation moves a carbon atom (in the upper conductor) to the lowest point of the conductor (in the y-direction), and an 18° rotation moves it slightly more, such that the same carbon atom now defines a joint lowest point on the conductor. The lower conductor was stationary for all cases.

3.2 Results of Undoped SWNT Junctions

The results of the undoped junctions are presented here, in the following order: effects of nanotube separation distance, and effects of rotational misalignment, all with varying overlap distances.

The isolated junction was relaxed to a nanotube separation distance of $l_{SWNT-SWNT}^* = 3.36 \text{ \AA}$, while different nanotube separation distances ($l_{SWNT-SWNT} = 1.50, 2.00, 2.50, 3.00, 3.50$, and 4.00 \AA) have also been tested. Due to the highly constrained conditions which the packing arrangement imposed on the model, the relaxed structure for the two SWNTs at the nanotube separation distance of $l_{SWNT-SWNT} = 1.50 \text{ \AA}$ and 2.00 \AA did not maintain a uniform circular cross section, leading to an unrealistically high total energy value. As for the nanotube separation distance of $l_{SWNT-SWNT} = 2.50, 3.00, 3.50$, and 4.00 \AA , the energy values of the junctions were close to the energy value of the junction at $l_{SWNT-SWNT}^* = 3.36 \text{ \AA}$, the difference being $< 0.03\%$. For all overlap distances, the energy values of all six junctions ($l_{SWNT-SWNT} = 1.50 - 4.00 \text{ \AA}$) were higher than the energy value of the junction that was structurally relaxed as isolated nanotubes ($l_{SWNT-SWNT}^* = 3.36 \text{ \AA}$).

In Fig. 1 (right) the conductance for the different nanotube separation distances is shown, where the highest conductance value for the three, five, and seven unit cell overlaps occurred at $l_{SWNT-SWNT} = 3.00 \text{ \AA}$. For the one unit cell overlap the highest conductance occurred at 2.50 \AA . Comparing to the junction with a separation distance of $l_{SWNT-SWNT}^* = 3.36 \text{ \AA}$ (and a looser packing arrangement) shown on the dotted line in the same figure, it can be seen that at a closer packing the junction conductance rose sharply. Around the nanotube separation distance of $2.50 - 3.00 \text{ \AA}$ (close to the optimal nanotube separation distance of 3.36 \AA), the conductance had a strong dependence on the overlap distances. Moreover, Fig. 1 (right)

shows that at constant separation distances, the variation of the conductance with overlap was not monotonic, which is not surprising; previous computational efforts have shown oscillatory conductance variations for both graphene [4], and SWNT junctions [25], as a function of overlap distance.

In terms of rotational misalignment introduced effects, both the 12° and 18° rotations reduced the conductance drastically, as compared to the junction with no misalignment, as shown on the left in Fig. 6. In fact, the 12° rotation created a gap in the transmission plot similar to that of an undoped semiconducting SWNT conductor, as shown on the right in Fig. 6, leading to zero conductance at the Fermi energy. The 18° rotation models had a finite conductance, albeit much lower than the rotationally aligned junction.

3.3 Geometry of Doped SWNT Junctions

The geometries used to perform the computation of the doped junction models are presented here, specifically on the approach of packing the doped SWNT junctions. Two dopants were tested for the doped junction models: the K atom and the AuBr₄ fragment. Additionally, for each dopant type, two doping configurations were explored: the external doping configuration and the interstitial doping configuration. The motivation for studying the external doping configuration was the positive results shown in the previous work on SWNT conductors [18], whereas study of the interstitial doping configuration was inspired by the work on polyiodide doped CNT junctions [13]

Similar to the process used for the undoped junctions, the equilibrium nanotube separation distance ($l_{SWNT-SWNT}^*$) was obtained after structural relaxation. In addition, the dopant standoff ($l_{dopant-SWNT}^*$) and dopant separation distance ($l_{dopant-dopant}^*$) were obtained, respectively, for the externally doped and interstitially doped junctions. Next, alternate end segments were removed (at equal lengths, along with the electrode dopants) depending on the overlap distance desired, for transport calculations.

For the transport calculations, like the undoped junction, the SWNT conductors in the doped junction model and in the periodic images were separated by the nanotube separation distance, $l_{SWNT-SWNT}^*$. However, this only applied to the periodic images in directions whereby there were no dopants between the SWNTs. Specifically, for the externally doped models, the SWNTs were separated by the nanotube separation distance only in the x -direction (since there were only dopants between the periodic images in the y -direction); for the interstitially doped models, the SWNTs were separated by the nanotube separation distance only in the y -direction (since there were only dopants between the periodic images in the x -direction). As for the directions that had dopants between the SWNTs in periodic images, it was assumed that the distance between dopants (in periodic images) in the external doping configuration case to be twice the dopant standoff ($2l_{dopant-SWNT}^*$), while the distance between dopants (in periodic images) in the interstitial doping configuration case is the dopant separation distance ($l_{dopant-dopant}^*$). The equations that embody the assumptions for the packing arrangement (in a computational unit cell of dimensions $x_{junc} \times y_{junc} \times z_{junc}$) were

$$x_{junc} = \begin{cases} l_{SWNT-SWNT}^* + d_{SWNT}, & \text{for the external doping configuration} \\ 2l_{dopant-dopant}^*, & \text{for the interstitial doping configuration} \end{cases} \quad (4)$$

$$y_{junc} = \begin{cases} 4l_{dopant-SWNT}^* + l_{SWNT-SWNT}^* + 2d_{SWNT}, & \text{for the external doping configuration} \\ 2l_{SWNT-SWNT}^* + 2d_{SWNT}, & \text{for the interstitial doping configuration} \end{cases} \quad (6)$$

$$z_{junc} = \begin{cases} l_{SWNT-SWNT}^* + d_{SWNT}, & \text{for the external doping configuration} \\ 2l_{SWNT-SWNT}^* + 2d_{SWNT}, & \text{for the interstitial doping configuration} \end{cases} \quad (7)$$

where d_{SWNT} is the diameter of the SWNT conductor, with z_{junc} as the length of the model. Figures 2 (right) and 3 show the computational unit cells for the different doping configurations.

The first of the two doped junctions examined was the K doped junction. The two doping configurations for the K doped junctions are shown in Fig. 7. Due to the size of the K atom, which spans the length of one unit cell in the (5,5) SWNT, the K doped junctions were doped at one atom per two unit cells. This led to the total number of unit cells for each K doped SWNT conductor in the junctions to be a multiple of two: the SWNT conductors were 16 unit cells long before removal of the ends. For the external K doping configuration, the nanotube separation distance ($l_{SWNT-SWNT}^*$) was 3.46 Å, and the dopant standoff ($l_{dopant-SWNT}^*$) was 2.62 Å. For the interstitial K doping configuration, the nanotube separation distance ($l_{SWNT-SWNT}^*$) was 3.41 Å, and the dopant separation distance ($l_{dopant-dopant}^*$) was 6.42 Å. The dimensions for the computational unit cells used are listed in Table 2.

The second of the two doped junctions examined was the AuBr₄ doped junction. The two doping configurations for the AuBr₄ doped junctions are shown in Fig. 8. Due to the size of the AuBr₄ fragment, which spans the length of three unit cells, in the (5,5) SWNT, the AuBr₄ doped SWNT were doped at one fragment per three unit cells. This led to the total number of unit cells of each AuBr₄ doped SWNT conductor in the junction to be a multiple of three: the SWNT conductors were 15 unit cells long before the removal of the ends. For the external AuBr₄ doping configuration, the nanotube separation distance ($l_{SWNT-SWNT}^*$) was 3.39 Å, and the dopant standoff ($l_{dopant-SWNT}^*$) was 3.36 Å. For the interstitial AuBr₄ doping

configuration, the nanotube separation distance ($l_{SWNT-SWNT}^*$) was 3.79 Å, and the dopant separation distance ($l_{dopant-dopant}^*$) was 11.43 Å. The dimensions for the computational unit cells used are listed in Table 2.

3.4 Results of Doped SWNT Junctions

The results of the K and AuBr₄ doped junctions, with the external doping and interstitial doping configurations both at various overlap distances, are presented here, along with a further investigation of packing effects on the interstitially doped K junction. Note that, while the results in Fig. 9 compares the doped junction conductance with the undoped one (that relaxed in an isolated setting, resulting in $l_{SWNT-SWNT}^* = 3.36$ Å), the packing densities are different, due to the complexity of packing doped junction models.

For the K doped junctions, both doping configurations improved the conductance, as shown in Fig. 9. The highest conductance value for the K doped junction was $1.02G_0$. It was obtained with the interstitial doping configuration at an overlap distance of seven unit cells, with the nanotube packing rule (in the x_{junc} direction) derived from the rule for interstitially doped models (shown on the right of Fig. 2). The external doping configuration performed similarly to the interstitial doping configuration, which resulted in a conductance range of $G = 0.32G_0 - 0.95G_0$.

The effect of packing arrangement was further investigated, done by increasing the packing density of the interstitially doped K junction. This was done by using Eqn. (2) in place of Eqn. (5) to reduce the computational unit cell size, shown on the third entry in Table 2; the corresponding packing density is shown in Table 3 as $9.368 \times 10^{-3} \text{ Å}^{-2}$. On the right of Fig. 9 the effect of the packing arrangement on the conductance can be seen. The conductance of the interstitially doped K junction decreased when the nanotube packing (in x_{junc}) was reduced from 12.84 Å (Eqn. (5), packing density of $7.639 \times 10^{-3} \text{ Å}^{-2}$) to 10.47 Å (Eqn. (2), packing density of $9.368 \times 10^{-3} \text{ Å}^{-2}$). Such behavior is consistent to the undoped junctions, as the nanotube separation distance decreased from 3.0 Å (equivalent to an increase in packing density). This suggested that the packing density of the interstitially doped K junction is a bit higher than the optimal density, but further tests are needed to support that statement.

Next, in regard to the AuBr₄ doped junctions: depending on the type of dopant configuration, the AuBr₄ fragment had a mixed effect on the (5,5) junction, as shown in Fig. 9. The external doping configuration had an adverse effect on the junction conductance, which was reduced to $\leq 0.41G_0$ across the different overlap distances. The interstitial doping configuration however, had a large positive effect on the junction conductance. At an overlap distance of five unit cells, the conductance exceeded the benchmark value for an undoped (5,5) SWNT at $2.04G_0$. The conductance for the interstitially doped AuBr₄ junction was also independent of the junction overlap; for all overlap distances the conductance stayed in the range of $1.8G_0$.

3.5 Discussion

The effects of nanotube separation distance and rotational misalignment were seen in the undoped SWNT junction models, while the effects of dopant type, doping configuration, and packing arrangement were observed in the doped SWNT junction models. The junction overlap distance was also another influence on both the undoped and doped junction model.

- Nanotube separation distance, $l_{SWNT-SWNT}$: The junction conductance rose at $l_{SWNT-SWNT} = 2.00$ Å before dropping at $l_{SWNT-SWNT} = 3.00$ Å; it was highest between $l_{SWNT-SWNT} = 2.50$ to 3.00 Å, much higher than the junction conductance at $l_{SWNT-SWNT}^* = 3.36$ Å. The relative maximum of the junction conductance in the range of $l_{SWNT-SWNT} = 2.50$ to 3.00 Å suggests that a tighter packing arrangement is beneficial, since $l_{SWNT-SWNT}^* = 3.36$ Å (at which the system was more energetically favorable than at any of the other $l_{SWNT-SWNT}$). Thus, it appears that the radial densification as performed by experimental researchers in [3] had a positive effect on the undoped junction conductance.
- Rotational misalignment: The rotational misalignment of the junctions drastically reduced the conductance, and was likely due to the reduction in the π bond overlap as the misalignment increases. At a 12° rotation misalignment, the junction even had a gap in its transmission plot, similar to that of an undoped SWNT. In carbon nanotubes, the p_z orbitals of the carbon atoms interact with each other to form π orbitals, which are the main contributors to the conduction of the SWNT [26]. Tripathy et al. suggested that the dependence of conductance on the crossing angle between nanotubes in junctions is due to the overlap of the π orbitals [5], which is also a possible explanation for the observation shown here. Here, it is speculated that when both SWNTs are rotationally aligned (at 0° , shown in (a) of Fig. 4), the π orbitals on the junction interface overlap; in addition to the intratube π orbital interaction, this improves the junction conductance. As the rotational misalignment increases, the overlap region shrinks, and in turn reduces the junction conductance.
- K and AuBr₄ doping, for both doping configurations: The K atom had a positive effect on the junction, in both the external and interstitial doping configuration. Both doping configurations have conductance that are quite similar across different overlap distances. As for the AuBr₄ doped junctions, only the interstitial doping configuration improved the junction conductance, while the external doping configuration reduced the conductance, as compared to the undoped junction. According to Saito, the most effective type of dopant in inducing charge transfer in CNTs would be a highly electropositive element, like alkali metals [27]. This could explain why the conductance for the K doped junctions were less dependent on the dopant configuration, as compared to the AuBr₄ doped junctions. For the AuBr₄ doped junction,

the proximity of the dopant to the CNT interface seems to be important; the positioning of the AuBr₄ fragments closer to the interface seems to raise the junction conductance.

- **Packing arrangement:** In the case of the (packed) undoped SWNT junctions, there was an optimum packing arrangement ($l_{SWNT-SWNT} = 2.50 - 3.00 \text{ \AA}$) resulting in high junction conductance. In the interstitially doped K junction case however, the conductance decreased when the packing density increased. More data points on the packing of K doped junctions will be needed in order to obtain a verdict on the ideal packing size. With only a small dataset, it seems that the optimum in packing density (for a relative maximum in junction conductance) was not observed here; the reduction in packing of the interstitial K doped junction from $x_{junc} = 12.84 \text{ \AA}$ to $x_{junc} = 10.47 \text{ \AA}$ was detrimental to conductance.
- **Junction overlap distance:** A nonmonotonic behavior of both the undoped and doped junction conductance was observed, as the overlap distance was increased. Such behavior is common in graphene and SWNT junctions [4,25], although in the mentioned works a higher number of overlaps was tested. While longer SWNT junctions (i.e. longer overlap distances) can capture the behavior over larger ranges in this work, computational costs were a concern for models of such size, especially in utilizing a DFT-based software like SIESTA.

4 Nanowire Model

In this section, a method to describe the macro-scale performance of CNTs is presented: a nanowire model was defined to compute specific conductivity, expressed as a performance metric M . A combination of doped SWNT conductor and junction models was used to compute the metric, with the conductor results from a previous work [18] and the junction results from Section 3. The performance of the nanowires was then evaluated through a comparison of specific conductivity to the specific conductivity of copper.

The metric M for the nanowire was based on another previous work [13] that describes the specific conductivity. In the case of the CNT-based nanowire, the specific conductivity is affected by the ballistic conductance G within the electronic mean free path in CNTs, L_{MFP} , in a unit of mass. Associating the specific conductivity of continuum material to a non-continuum one, the metric was defined as:

$$\frac{1}{M} = \frac{\rho}{\sigma} = \hat{m}_{eff} \frac{R_{eff}}{L_{MFP}}, \quad R_{eff} = \frac{1}{\min(G_c, G_j)}, \quad (8)$$

where ρ and σ are the mass density and conductivity of a continuum material respectively, \hat{m}_{eff} is the effective mass per unit length of the nanowire, R_{eff} is the effective resistance of the nanowire, and G_c (or G_j) is the conductance of the conductor (or junction). The ‘min’ function ensured that the nanowire model can only allow electronic transmission at the lower conductance (between the conductor and junction), since that would be the limiting factor for electronic transport. The effective mass per unit length is defined as

$$\hat{m}_{eff} = (1 - \alpha)\hat{m}_c + \alpha\hat{m}_j, \quad \hat{m}_c = \frac{m_c}{L_c}, \quad \hat{m}_j = \frac{m_j}{L_j}, \quad \text{and } \alpha = \frac{L_j}{L_{MFP}}, \quad (9)$$

where m_c (or m_j) is the mass of a conductor (or junction) with the length L_c (or L_j). Here, α is defined as the fractional overlap of the nanowire.

The junction results from the previous section is shown in Table 3, which includes the fractional overlap, mass per unit length, packing density, and conductance values for the doped junctions. The highest and lowest conductance results for the junction models (with regard to the fractional overlap, mass per unit length, and packing density) were considered for the nanowire model. The conductor results, obtained from [18], is shown in Table 4.

The nanowire performance metric M in its functional form is expressed as:

$$M = f(m_c, m_j, L_c, L_j, G_c, G_j) \quad (10)$$

where the values for the variables were obtained from the models presented in a previous work [18] and from Section 3. Since two different doping concentrations were studied for the conductor models, and two doping configurations were studied for the junction models, four combinations of conductor and junction models were analyzed to create the nanowire model. The properties of the models are shown in Table 5, representing high performance configurations for the different types of disassociated dopants (highest conductance values) for strictly metallic SWNT conductors and junctions.

The results of the nanowire model were compared to a continuum conductor made of copper, designated as the reference metric, M_{ref} . Since the reference metric was obtained from a continuum model, the specific conductivity formula (shown as

the inverse in Eqn. (8)) only requires the conductivity (σ) and the mass density (ρ), which yields $M_{ref} = 6671.30 \text{ Sm kg}^{-1}$ [28]. A mean free path of $L_{MFP} = 500 \text{ nm}$ was chosen for the nanowire model, based off a study on metallic SWNTs [29].

Figure 10 shows a comparison of specific conductivity predicted by the nanowire model versus copper. The metrics for different combinations had different ranges. Notably, the K doped nanowire showed a wider variation (shown on the left) than the AuBr_4 doped nanowire (shown on the right). In fact, the AuBr_4 doped nanowire was extremely sensitive to the junction doping configuration. Quantitatively, the relative specific conductivity for the K doped nanowire (as compared to copper) ranged from 0.524 to 3.357, while the relative specific conductivity for the AuBr_4 doped nanowire ranged from 0.154 to 4.164. The experimental relative specific conductivity for the KAuBr_4 doped CNT in [3], shown in black dashed lines in Fig. 10, was 0.73 (73% of the specific conductivity of copper) at $4842.86 \text{ Sm}^2 \text{ kg}^{-1}$, and is within the computed ranges for the K doped and AuBr_4 doped nanowires.

It is noted that the nanowire model presented in this work is expected to outperform the experimental data obtained from [3]. In that work, the KAuBr_4 doped CNT consisted of nanotubes that were SWNTs and MWNTs, and possibly included a mixture of both metallic and semiconducting nanotubes. Hence, the observed difference of the experimental specific conductivity, as compared to the nanowire models, is reasonable. Furthermore, the experimental doping configuration is undetermined for the KAuBr_4 doped CNT; the dopant could either adsorb to the CNTs in its disassociated form (as K atoms and AuBr_4 fragments) or as a complete KAuBr_4 molecule, or both. These factors could all contribute to the discrepancy between the nanowire performance and the experimental data in Fig. 10. Moreover, the fractional overlap α may vary from junction to junction. Hence the nanowire model is a ‘high performance model’ and it estimates a higher specific conductivity than the experimental reference indicates.

5 Conclusions

Finally, the research efforts are concluded in this section by a presentation of the principal findings on the SWNT junctions and nanowires. First off, the (5,5) SWNT junctions showed reactions to varying nanotube separation distances, rotational misalignment, K and AuBr_4 doping at both the external and interstitial doping configurations, different packing arrangements, as well as separate overlap distances:

- The nanotube separation distance of $l_{SWNT-SWNT}^* = 3.36 \text{ \AA}$ was obtained from relaxing two isolated and undoped SWNT conductors, but with a slight decrease of nanotube separation distance (to $l_{SWNT-SWNT} = 2.50$ to 3.00 \AA) the junction conductance increased sharply; further decrease in the separation distance reduced the conductance. This suggested an optimum in packing arrangement (with the different $l_{SWNT-SWNT}$) that will lead to an increased conductance, which also points to the benefit of radial densification as performed in [3].
- The rotational misalignment was tested at a misalignment of 12° and 18° , which notably deteriorated the junction conductance. The decrease in conductance due to rotational misalignment between the SWNT conductors in the junction can be described as the reduction in π orbital overlap between the conductors; similar behavior was found in a misalignment of SWNT tube axes [5].
- K had a positive effect on the SWNT junction conductance, and was not quite as sensitive to different doping configurations. On the other hand, the interstitially doped AuBr_4 junction was significantly better than the externally doped AuBr_4 junction in increasing junction conductance. As pointed out by Saito, alkali metals are the leading candidates in altering nanotube electronic states [27], and this supports the argument that the K atom affects the SWNT junctions’ electronic state more than the AuBr_4 fragments: the K atom as an alkali metal is extremely reactive, and has a higher tendency to alter the electronic state of the SWNT junctions as compared to the AuBr_4 fragment, which was heavily dependent on doping configuration for high conductance.
- The packing arrangement affected the junction conductance. As seen in the undoped SWNT junction, the conductance can be increased with an increase in packing density from the isolated relaxation case (that gave a nanotube separation distance of $l_{SWNT-SWNT}^*$); with an optimal packing density (at a nanotube separation distance between $2.50 - 3.00 \text{ \AA}$), the conductance is at its relative maximum. This suggests that the situation might be similar with the doped junctions. However, due to the size of the dataset in this work, the optimum was not observed for the interstitially doped K junction with an increase in packing density.
- The junction overlap distance had a nonmonotonic effect on both the undoped and doped junction conductance, which was expected from previous work [4, 25]. Testing longer overlaps could be useful in characterizing the junction conductance’s dependence on overlap distances, but that would increase the size of the junction models, which was a challenge for computation.

Next, a nanowire model was provided to compare the findings with the experiments of [3], as well as to bulk copper. The experimental specific conductivity of the KAuBr_4 doped CNT fell within the range of the nanowire model values. As expected, the high performance configuration nanowire models had a specific conductivity higher than the experimental value, since many factors such as the doping configuration and the mixture of nanotubes could lower the experimental value. Note that it is possible to experimentally produce doped CNTs with specific conductivity much higher than that of copper:

Zhao et al. showed that with iodine doping, the specific conductivity of nanotube cables surpassed copper's by a factor of three [30] (although the nanotubes in question were double walled, which are metallic even if both the inner and outer nanotubes are semiconducting [31]).

Overall, using the nanowire model, the doped SWNT junctions results showed the potential of disassociated KAuBr_4 molecules, namely the K atom and AuBr_4 fragment, in improving the specific conductivity of CNTs. As part of future work, KAuBr_4 doped junctions are considered for the nanowire model, as well as exploring doped semiconducting SWNT junctions. With that, a better understanding of doped CNTs can be achieved, in order to support the experimental efforts in the enhancement of CNT based conductive wires.

Acknowledgements

This work was supported by the Office of Naval Research grant (Grant No. N00014-15-1- 2693). Computer time support provided by the Texas Advanced Computing Center at the University of Texas at Austin and the Department of Defence High Performance Computing Modernization Program.

References

- [1] Puchades, I., Lawlor, C. C., Schauerman, C. M., Bucossi, A. R., Rossi, J. E., Cox, N. D., and Landi, B. J., 2015, "Mechanism of Chemical Doping in Electronic-Type-Separated Single Wall Carbon Nanotubes Towards High Electrical Conductivity," *Journal of Materials Chemistry C*, **3**(39), p. 10256.
- [2] Srivastava, S., Kino, H., and Joachim, C., 2016, "Contact Conductance of a Graphene Nanoribbon with its Graphene Nano-Electrodes," *Nanoscale*, **8**(17), pp. 9265-9271.
- [3] Cress, C. D., Ganter, M. J., Schauerman, C. M., Soule, K., Rossi, J. E., Lawlor, C. C., Puchades, I., Ubnoske, S. M., Bucossi, A. R., and Landi, B. J., 2017, "Carbon Nanotube Wires with Continuous Current Rating Exceeding 20 Amperes," *Journal of Applied Physics*, **122**(2), p. 025101.
- [4] González, J. W., Santos, H., Pacheco, M., Chico, L., and Brey, L., 2010, "Electronic Transport through Bilayer Graphene Flakes," *Physical Review B*, **81**(19), p. 195406.
- [5] Tripathy, S., and Bhattacharyya, T. K., 2016, "Role of Inter-Tube Coupling and Quantum Interference on Electrical Transport in Carbon Nanotube Junctions," *Physica E*, **83**, pp. 314-321.
- [6] Janas, D., Milowska, K. Z., Bristowe, P. D., and Koziol, K. K. K., 2017, "Improving the Electrical Properties of Carbon Nanotubes with Interhalogen Compounds," *Nanoscale*, **9**(9), pp. 3212-3221.
- [7] Alvarenga, J., Jarosz, P. R., Schauerman, C. M., Moses, B. T., Landi, B. J., Cress, C. D., and Raffaele, R. P., 2010, "High Conductivity Carbon Nanotube Wires from Radial Densification and Ionic Doping," *Applied Physics Letters*, **97**(18), p. 182106.
- [8] Lee, R. S., Kim, H. J., Fischer, J. E., Thess, A., and Smalley, R. E., 1997, "Conductivity Enhancement in Single-Walled Carbon Nanotube Bundles Doped with K and Br," *Nature*, **388**(6639), pp. 255-257.
- [9] Kim, K. K., Bae, J. J., Park, H. K., Kim, S. M., Geng, H., Park, K. A., Shin, H., Yoon, S., Benayad, A., Choi, J., and Lee, Y. H., 2008, "Fermi Level Engineering of Single-Walled Carbon Nanotubes by AuCl_3 Doping," *Journal of the American Chemical Society* **130**(38), pp. 12757-12761.
- [10] Li, E., and Marzari, N., 2011, "Improving the Electrical Conductivity of Carbon Nanotube Networks: A First-Principles Study," *ACS Nano*, **5**(12), pp. 9726-9736.
- [11] Saito, S., 1999, "Electronic Properties of Potassium-Doped Carbon Nanotube Lattice, Amorphous and Nanostructured Carbon, Sullivan, J.P., Robertson, J., Zhou, O., Allen, T. B., and Coll, B. F., 1st ed., Vol. **593** *MRS Symposium Proceedings*, Materials Research Society, Pennsylvania, USA, pp. 161-166.
- [12] Ketolainen, T., Havu, V., and Puska, M. J., 2017, "Conductivity of AuCl_4 -Functionalized Carbon Nanotube Networks," *The Journal of Physical Chemistry C*, **121**(8), pp. 4627-4634.
- [13] Li, Y., and Fahrenthold, E., 2018, "Ab Initio Study of Iodine-Doped Carbon Nanotube Conductors," *Journal of Engineering Materials and Technology*, **140**(2), p. 021008.
- [14] Koziol, K., Vilatela, J., Moisala, A., Motta, M., Cuniff, P., Sennett, M., and Windle, A., 2007, "High-Performance Carbon Nanotube Fiber," *Science*, **318**(5858), pp. 1892-1895.
- [15] Li, T. S., Huang, Y. C., Lin, M. F., and Chang, S. C., 2010, "Conductance of Bilayer Graphene Nanoribbons with Different Widths," *Philosophical Magazine*, **90**(23), pp. 3177-3187.
- [16] Wang, J., Lin, Z., and Chan, K. S., 2014, "The Effect of Interlayer Coupling on Electron Transport in Graphene Nanoribbons: A Potential Method for Nanoposition Sensing," *Journal of Physics: Condensed Matter*, **26**(13), p. 135301.
- [17] Benameur, M. M., Gargiulo, F., Manzeli, S., Autès, G., Tosun, M., Yazyev, O. V., and Kis, A., 2015, "Electromechanical Oscillations in Bilayer Graphene," *Nature Communications*, **6**, p. 8582.

- [18] Chin, K. Y., 2018, “Molecular Doping of Carbon Nanotube Conductors,” MS Thesis, The University of Texas, Austin, TX, May.
- [19] Soler, J. M., Artacho, E., Gale, J. D., García, A., Junquera, J., Ordejón, P., and Sánchez-Portal, D., 2002, “The SIESTA Method for Ab Initio Order-N Materials Simulation,” *Journal of Physics: Condensed Matter*, **14**(11), pp. 2745-2780.
- [20] Perdew, J. P., Burke, K., and Ernzerhof, M., 1996, “Generalized Gradient Approximation Made Simple,” *Physical Review Letters*, **77**(18), pp. 3865-3868.
- [21] Bonardi, P., Achilli, S., Tantardini, G. F., and Martinazzo, R., 2015, “Electron Transport in Carbon Wires in Contact with Ag Electrodes: A Detailed First Principles Investigation,” *Physical Chemistry Chemical Physics*, **17**(28), p. 18413.
- [22] The Siesta Group, 2016, “USER’S GUIDE: SIESTA 4.0,” Retrieved from <https://departments.icmab.es/leem/siesta/Documentation/Manuals/siesta-4.0.pdf>
- [23] Brandbyge, M., Mozos, J., Ordejón, P., Taylor, J., and Stokbro, K., 2002, “Density-Functional Method for Nonequilibrium Electron Transport,” *Physical Review B*, **65**(16), p. 165401.
- [24] Band, Y. B., and Avishai, Y., 2013, *Quantum Mechanics with Applications to Nanotechnology and Information Science*, Academic Press, Amsterdam, The Netherlands, Chap. 13, p. 757.
- [25] Buia, C., Buldum, A., and Lu, J. P., 2003, “Quantum Interference Effects in Electronic Transport through Nanotube Contacts,” *Physical Review B*, **67**(11), p. 113409.
- [26] Bell, R. A., 2015, *Conduction in Carbon Nanotube Networks*, Springer, Cham, Switzerland, Chap. 2, p. 14.
- [27] Saito, S., 1999, “Design of Fullerene-Based Solids and Fullerides, Fullerenes, Kadish, K. M., and Ruoff, R. S., 1st ed., Vol. 4 *Recent Advances in the Chemistry and Physics of Fullerenes and Related Materials*, The Electrochemical Society, New Jersey, USA, pp. 1055-1062.
- [28] Matula, R. A., 1979, “Electrical Resistivity of Copper, Gold, Palladium, and Silver,” *Journal of Physical and Chemical Reference Data*, **8**(4), p. 1147.
- [29] Mann, D., Javey, A., Kong, J., Wang, Q., and Dai, H., 2003, “Ballistic Transport in Metallic Nanotubes with Reliable Pd Ohmic Contacts,” *Nano Letters*, **3**(11), pp. 1541-1544.
- [30] Zhao, Y., Wei, J., Vajtai, R., Ajayan, P. M., and Barrera, E. V., 2011, “Iodine Doped Carbon Nanotube Cables Exceeding Specific Electrical Conductivity of Metals,” *Scientific Reports*, **1**, p. 83.
- [31] Tison, Y., Giusca, C. E., Stolojan, V., Hayashi, Y., and Silva, S. R. P., 2007, “The Inner Shell Influence on the Electronic Structure of Double-Walled Carbon Nanotubes,” *Advanced Materials*, **20**(1), pp. 189-193.

Table 1. Computational unit cell dimensions of undoped junction models, and the equations used to generate the dimensions

Nanotube Separation Distance	x_{junc} (Å)	y_{junc} (Å)	z_{junc} (Å)	Comp. Unit Cell Equations
$l_{SWNT-SWNT} = 1.50$ Å	8.28	16.35	36.92	(2), (3)
$l_{SWNT-SWNT} = 2.00$ Å	8.78	17.35	36.92	
$l_{SWNT-SWNT} = 2.50$ Å	9.28	18.35	36.92	
$l_{SWNT-SWNT} = 3.00$ Å	9.78	19.35	36.92	
$l_{SWNT-SWNT}^* = 3.36$ Å	10.33	20.52	36.92	
$l_{SWNT-SWNT} = 3.50$ Å	10.28	20.35	36.92	
$l_{SWNT-SWNT} = 4.00$ Å	10.78	21.35	36.92	

Table 2. Computational unit cell dimensions of doped junction models, and the equations used to generate the dimensions

Dopant	Dopant Configuration	x_{junc} (Å)	y_{junc} (Å)	z_{junc} (Å)	Comp. Unit Cell Equations
K	External	10.38	27.65	39.38	(4), (6)
	Interstitial	12.84	20.39	39.38	(5), (7)
	Interstitial	10.47	20.39	39.38	(2), (7)
AuBr ₄	External	10.31	30.44	36.92	(4), (6)
	Interstitial	22.86	21.37	36.92	(5), (7)

Table 3. Fractional overlap, mass per unit length, packing density and conductance for the doped junctions

Dopant	Dopant Configuration	Fractional Overlap α ($\times 10^{-3}$)	Mass per Unit Length \hat{m}_j (amu Å ⁻¹)	Packing Density ($\times 10^{-3}$ Å ⁻²)	Conductance G_j/G_0
K	External	0.246	390.7	6.968	0.318
		1.230	253.4	6.968	0.824
		2.215	231.1	6.968	0.950
		3.199	227.4	6.968	0.908
	Interstitial	0.246	391.1	7.639	0.602
		1.230	260.0	7.639	0.760
		3.197	230.0	7.639	1.017
		0.246	391.1	9.368	0.170
		1.230	260.0	9.368	0.225
		3.197	230.0	9.368	0.783
AuBr ₄	External	0.246	681.5	6.373	0.074
		1.229	402.7	6.373	0.111
		2.213	324.9	6.373	0.183
		3.197	339.7	6.373	0.302
		4.182	355.0	6.373	0.415
	Interstitial	0.246	971.4	4.094	1.888
		1.230	402.4	4.094	1.841
		2.214	339.2	4.094	2.044
		3.199	364.1	4.094	1.637
		4.183	355.0	4.094	1.930

Table 4. Mass per unit length and conductance for the doped conductors, from [18]

Dopant	SWNT Chirality	Concentration (number per unit cell)	Mass per Unit Length \hat{m}_c (amu \AA^{-1})	Conductance G_c/G_0
K	(8,0)	0.50	94.7	1.644
		1.00	99.3	2.512
	(5,5)	0.50	105.6	2.958
		1.00	113.5	3.841
AuBr ₄	(8,0)	0.50	150.8	1.327
		1.00	211.3	1.946
	(5,5)	0.33	167.6	2.977
		0.67	237.5	3.960

Table 5. Combinations of conductors and junctions considered in the nanowire model calculation

Dopant	Conductor Dopant Concentration (dopant/u.c.)	Junction Doping Configuration
K	0.50	External
	0.50	Interstitial
	1.00	External
	1.00	Interstitial
AuBr ₄	0.33	External
	0.33	Interstitial
	0.67	External
	0.67	Interstitial

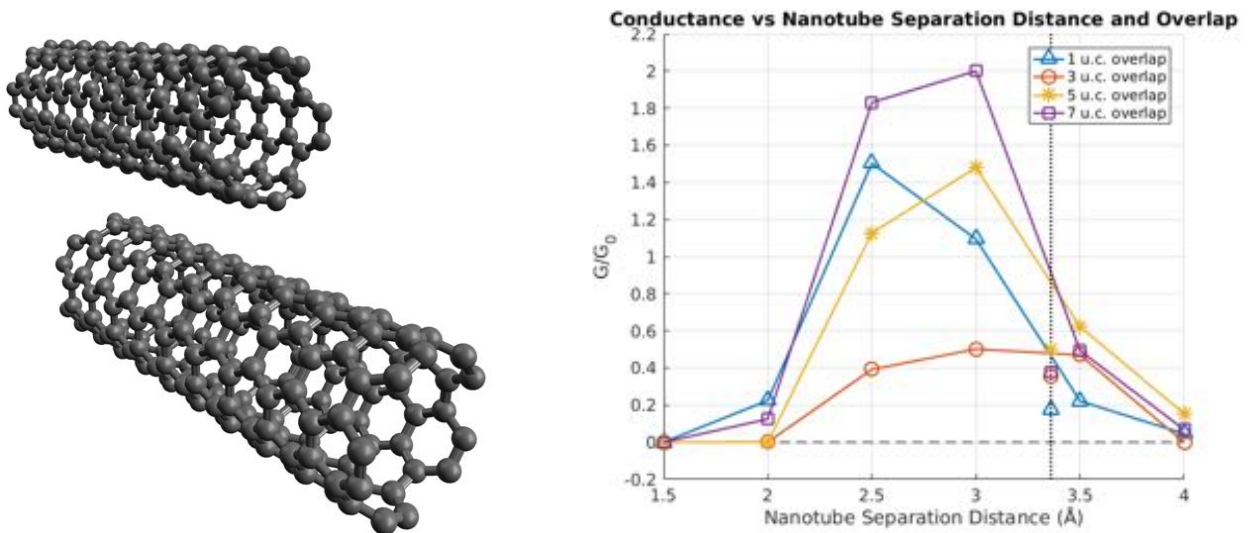


Fig. 1. On the left, an undoped junction with a five unit cell overlap; on the right, the conductance of the undoped (5,5) junctions as a function of varying overlap distance and nanotube separation distance for 0° rotation, with the vertical dotted line indicating the results for the isolated (equilibrium) relaxation model

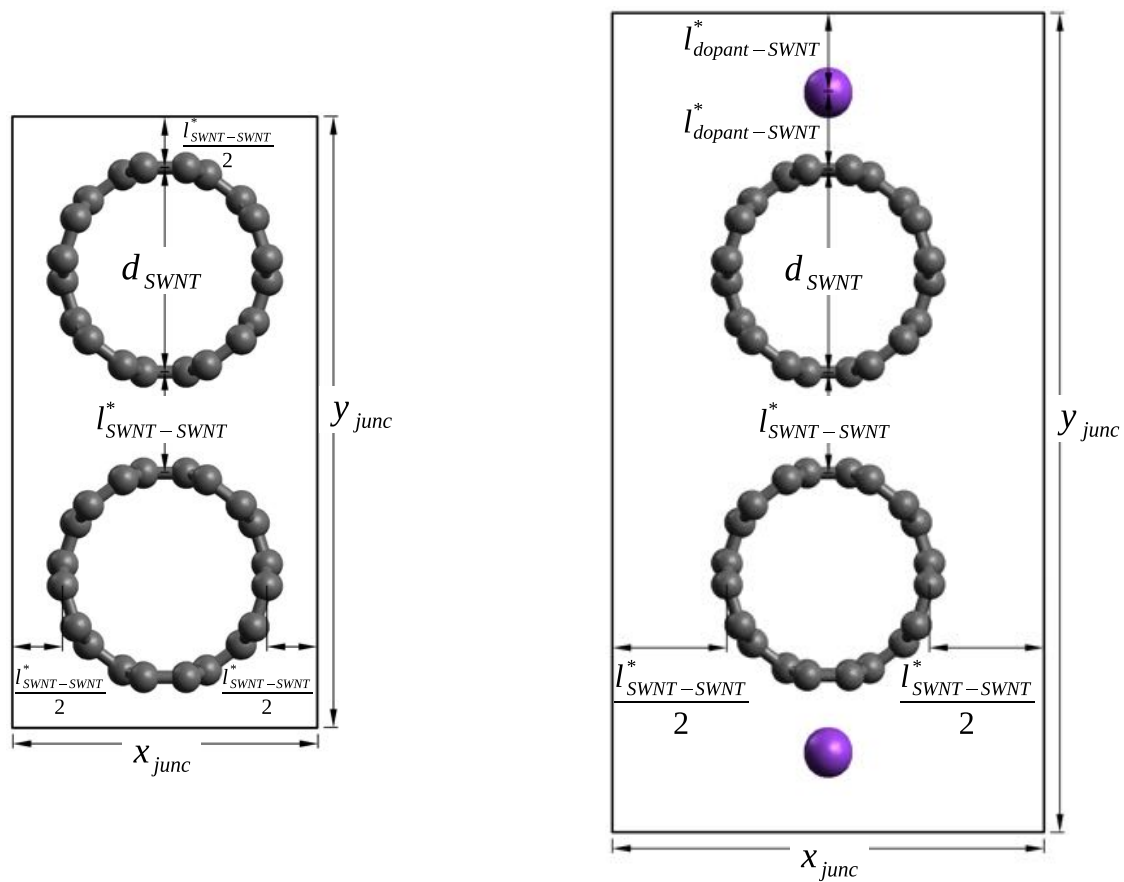


Fig. 2. Axial (projected) view of a computational unit cell for an undoped (left) and externally doped (right) junction (note that z_{junc} is the model length in the axial direction)

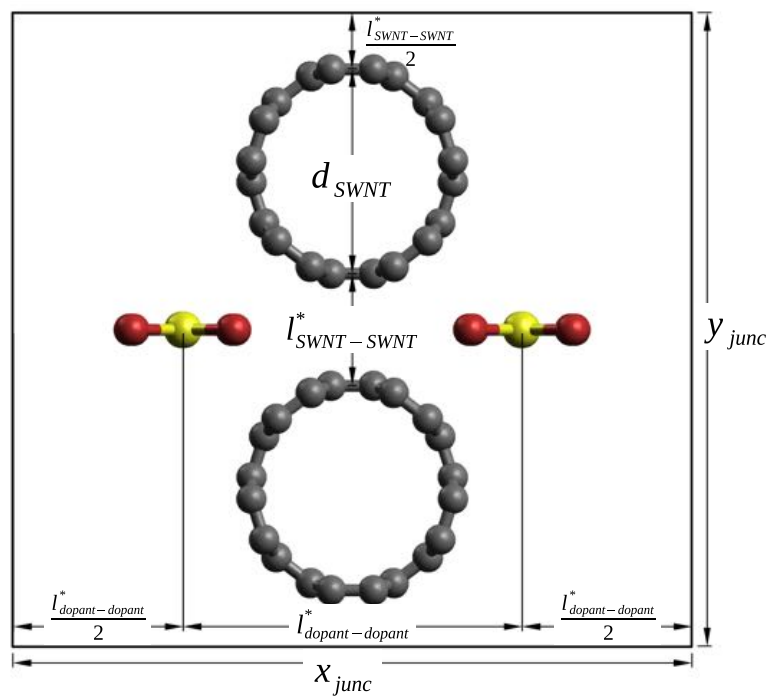


Fig. 3. Axial (projected) view of a computational unit cell for an interstitially doped junction (note that z_{junc} is the model length in the axial direction)

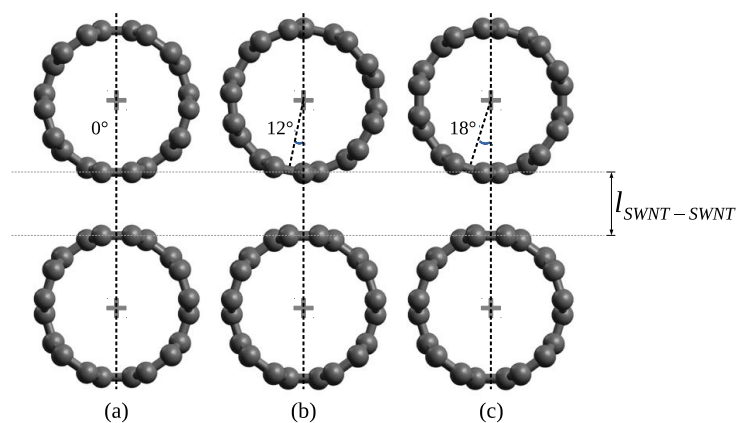


Fig. 4. Axial (projected) view of three SWNT junctions for three different rotational alignments (0° , 12° and 18°); the lower SWNT conductor is stationary in all cases

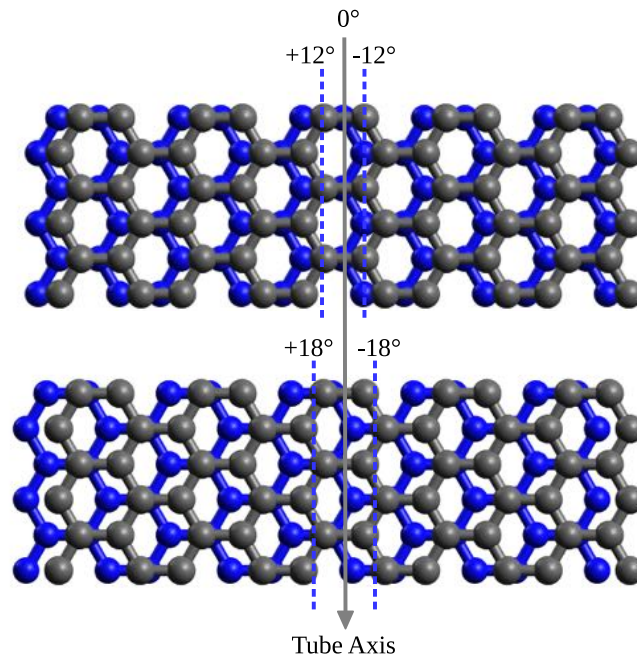


Fig. 5. Unrolled SWNTs for the rotationally misaligned junctions at 12° (top) and 18° (bottom); the grey (lighter) atoms represent the lower SWNT (in Fig. 4), and the blue (darker) atoms represent the upper SWNT (in Fig. 4)

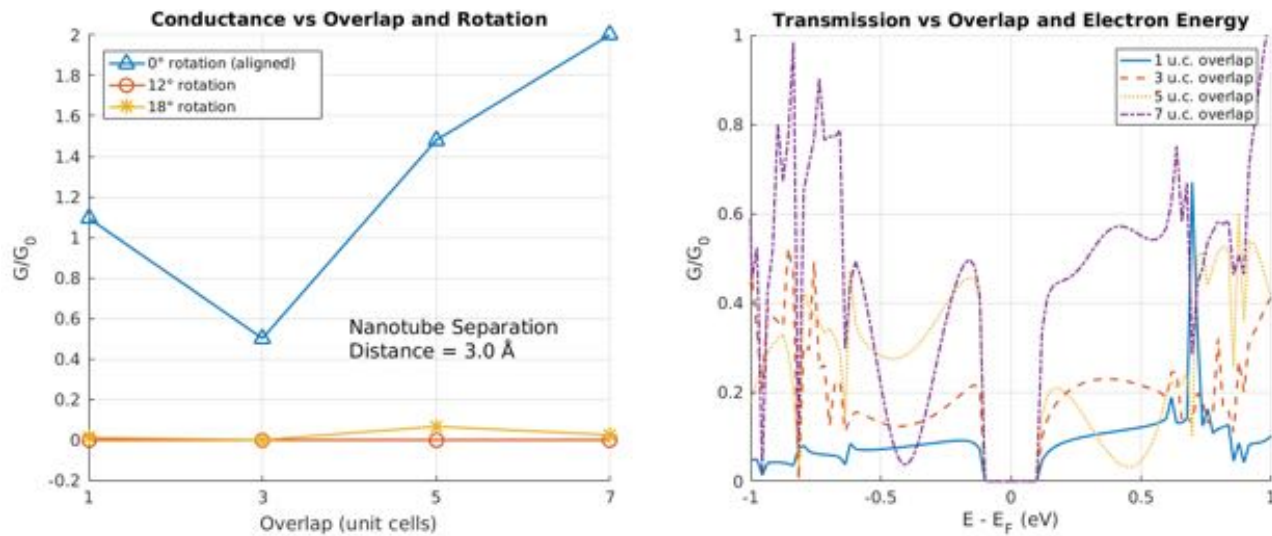


Fig. 6. On the left, conductance of the 12° and 18° rotationally misaligned junctions as a function of overlap, at a nanotube separation distance ($l_{SWNT-SWNT}$) of 3.0 Å; on the right, conductance of the 12° rotationally misaligned junction as a function of overlap and electron energy (in this work, the transmission data from the transport calculations was obtained through the sampling of 201 points between -2 eV to +2 eV)

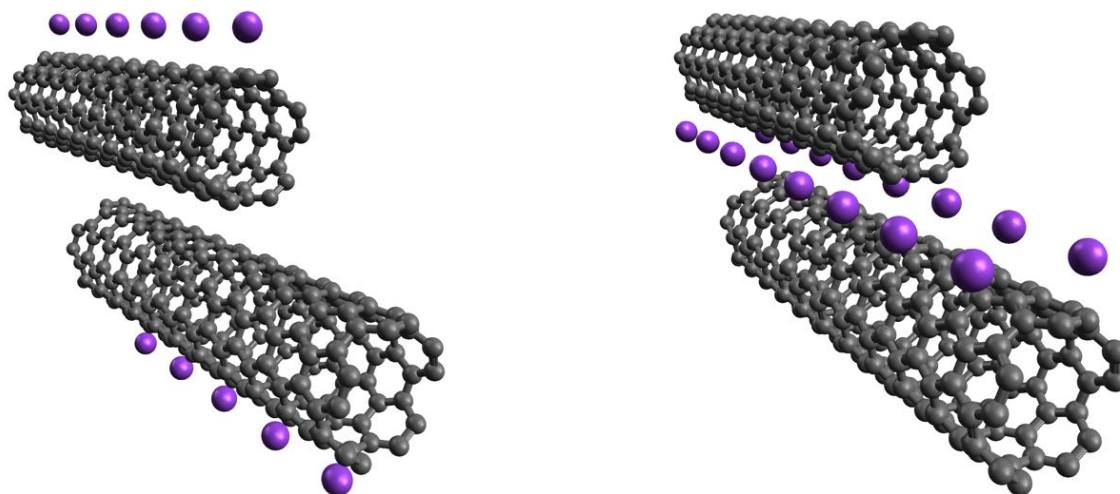


Fig. 7. K doped junctions: externally doped (left) and interstitially doped (right)

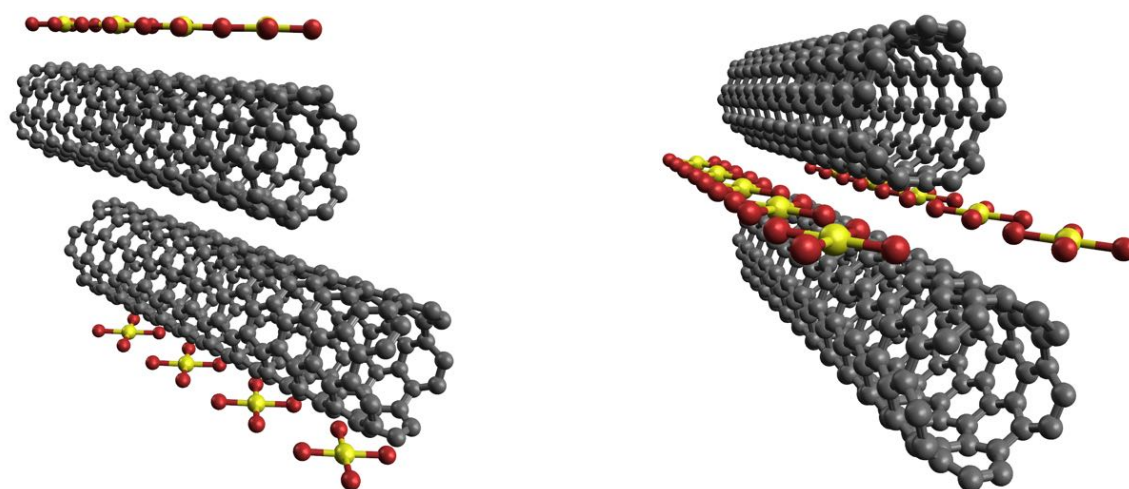


Fig. 8. AuBr_4 doped junctions: externally doped (left) and interstitially doped (right)

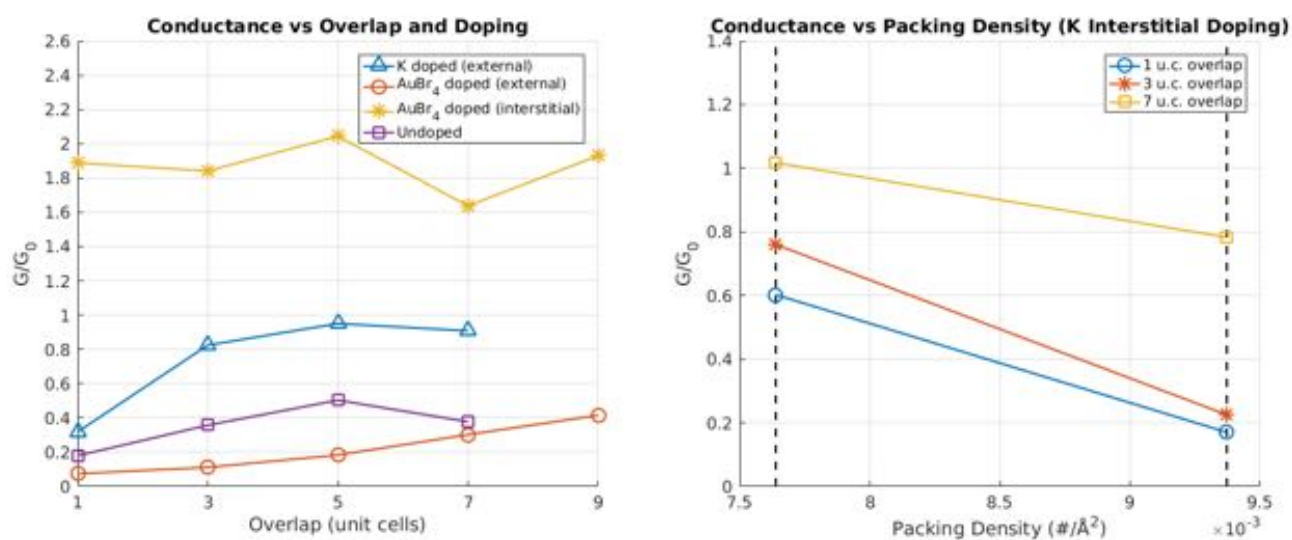


Fig. 9. On the left, effects of overlap and dopant configuration on conductance (note: due to the relaxation in an isolated setting, the different doped models—including the undoped case—have different packing densities); on the right, effects of overlap and nanotube packing on conductance

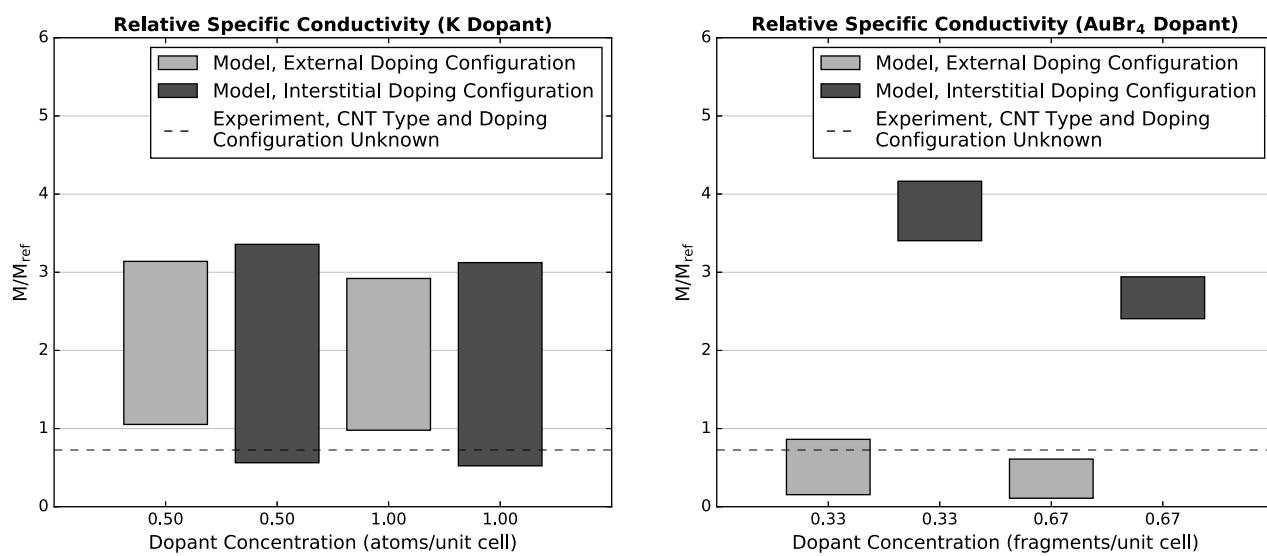


Fig. 10. The relative specific conductivity of the K doped nanowire (left) and $AuBr_4$ doped nanowire (right), with the dashed line indicating the specific conductivity of the $KAuBr_4$ -doped CNT (of which the doping origin is undetermined) in [3] as compared to M_{ref} ; the experimental reference is meant to show the plausibility of the presented nanowire model, not as a direct comparison